Cells as Living Materials: Force Spectroscopic Investigation of Mechanotransduction

Zellen als lebende Materialien:
Kraftspektroskopische Untersuchung der
Mechanotransduktion

Dissertation

zur Erlangung des akademischen Grades
Doktor der Ingenieurwissenschaften
(Dr.-Ing.)
der Technischen Fakultät
der Christian-Albrechts-Universität zu Kiel

vorgelegt von

Sandra Sindt-Lage

aus
Coburg

2022

Declaration of Authorship

I, Sandra Sindt-Lage, declare that the dissertation "Cells as Living Materials: Force Spectroscopic Investigation of Mechanotransduction" is in terms of content and form, apart from the advice given by my supervisor, my own work. I declare that I have identified all quotations of other authors and that I have listed all relevant sources to the best of my knowledge.

I declare that I did not partially or fully present this dissertation during any other examination procedure and that I did not submit it for any other publication.

I declare that I have used good scientific practise defined by the German Research Society (DFG) to produce and write this dissertation.

Kiel, 05/13/2022

Sandra Sindt-Lage

Reviewers:

Prof. Dr. Christine Selhuber-Unkel
Prof. Dr. Regine Willumeit-Römer

Date of oral examination: 06/10/2022

If one thing I know, I'll fall but I'll grow.
I'm walking down this road of mine, this road that I call home.

"Am I wrong" by Nico & Vinz

Lebe, sei glücklich und mache andere glücklich.

Mary Shelley

Abstract

Mechanotransduction describes a cellular mechanism of sensing and converting mechanical cues into biochemical signals to regulate cell processes, such as adhesion, migration, proliferation and/or apoptosis. Thus, becoming an ever-growing field of research with high potential for medical applications.

In the first part of my thesis, I present a novel strategy towards reliable microindentation measurements, which is essential for investigating mechanotransduction using soft substrates with defined material properties. I show a precise and reproducible determination of Young's moduli through an automatic analysis of indentation data. The algorithm presented detects Young's moduli in a region without dependence on indentation depth while minimizing the fitting error. This strategy is an essential step towards a comprehensive study of soft materials on a spatial scale similar to cell interactions. It has broad applicability ranging from fundamental research of mechanotransduction to developing innovative implants that match the *in vivo* situation more precisely.

In the second part of my thesis, I present novel approaches for multifaceted cellular manipulation. I show that layer thickness of a soft material fixed to a stiff underlying substrate can be crucial for cell adhesion. Since a stiffness mismatch between implant material and *in vivo* situation can lead to implant complications, such as scar formations that reduce signal transduction in brain tissue, these findings are pioneer for new implant designs and advanced application fields. In addition, I present two atomic force microscopy (AFM)-based manipulation systems that allow applying specific mechanical stimuli to single cells and a subsequent correlation to whole cell detachment and single bond strengths. The unique AFM-based shear system presented combines application of shear stimuli and cell detachment measurements, whereas the AFM-based modulation system combines oscillatory pushing and pulling with cell detachment measurements. Both shear and oscillatory forces are essential mechanical stimuli in our body. For instance, disturbed shear conditions interfere vascular functionality and increase the risk for atherosclerosis, whereas oscillatory forces are essential for bone formation or heart muscle contraction.

Thus, the strategies presented in this thesis are of significant medical interest allowing an overarching study of mechanotransduction and may pave the way towards smart stimulation devices that allow cell adhesion on demand.

Zusammenfassung

Mechanotransduktion beschreibt einen zellulären Mechanismus des Ertastens und Umwandelns mechanischer Reize in biochemische Signale, um Zellprozesse wie Migration, Adhäsion, Proliferation und/oder Apoptose zu steuern. Dadurch wurde Mechanotransduktion zu einem stetig wachsenden Forschungsgebiet mit erheblichem Potenzial für medizinische Anwendungen.

Im ersten Teil meiner Dissertation stelle ich eine neuartige Strategie zur zuverlässigen Mikroindentationsmessung vor. Dies ist für die Erforschung von Mechanotransduktion mittels weichen Substraten mit definierten Materialeigenschaften unerlässlich. Ich zeige eine präzise und reproduzierbare Bestimmung von Elastizitätsmoduln mittels einer automatischen Analyse von Indentationsdaten. Der dargestellte Algorithmus ermittelt Elastizitätsmoduln in einem Bereich ohne Abhängigkeit von der Eindringtiefe. Diese Strategie ist ein wesentlicher Schritt zu einer umfassenden Untersuchung weicher Materialien auf Zellebene mit einer Anwendbarkeit, die von der Grundlagenforschung der Mechanotransduktion bis zur Entwicklung innovativer Implantate reicht.

Im zweiten Teil meiner Dissertation stelle ich neue Ansätze zur vielfältigen Zellmanipulation vor. Ich zeige, dass die Schichtdicke eines weichen Materials, das an ein steifes Substrat befestigt ist, entscheidend für die Zelladhäsion sein kann. Ein Steifigkeitsunterschied zwischen Implantatmaterial und *in vivo*-Situation kann zu Implantatkomplikationen führen. Im Gehirn können zum Beispiel Narben entstehen, die die Signalübertragung beeinträchtigen. Deshalb können die Erkenntnisse meiner Dissertation wegweisend für die Entwicklung neuartiger Implantate sein. Darüber hinaus stelle ich zwei Rasterkraftmikroskopie-basierte Manipulationssysteme vor, die es ermöglichen, spezifische mechanische Stimuli auf einzelne Zellen auszuüben und anschließend mit der vollständigen Zellablösung sowie Einzelbindungskräften zu korrelieren. Das vorgestellte einzigartige Schersystem kann gezielte Scherstimuli auf einzelne Zellen ausüben, wohingegen das Modulationssystem oszillierendes Drücken und Ziehen mit Messungen der Zellablösung kombiniert. Sowohl Scherkräfte als auch oszillierende Kräfte sind wesentliche mechanische Reize in unserem Körper. Beispielsweise beeinträchtigen geschädigte Scherbedingungen die Gefäßfunktion und erhöhen das Risiko für Atherosklerose, während oszillierende Kräfte für die Knochenbildung oder Herzmuskelkontraktion unerlässlich sind.

Die in dieser Dissertation vorgestellten Strategien sind von erheblichem Interesse für die Medizin, da sie eine allumfassende Untersuchung der Mechanotransduktion ermöglichen und den Weg zu intelligenten Stimulationsgeräten ebnen können.

Contents

Chapter 1

Introduction

1.1 Biological Background

Cells are the smallest structural and functional unit of all living beings [1], [2]. Our survival is guaranteed through a variety of different tasks (e.g., structural support, molecular and electrical signaling, energy production) [2]. Some cell functions and tasks are universal [3], whereas distinct cell types emerged that specialized on certain functions [4]. For instance, neurons are responsible for electrical signal transduction, whereas cells of the immune system defend our body against foreign substances and endothelial cells give structural support [2], [3]. Although such cell functions can differ significantly, the basic structure of a cell is the same [1]. In mammalian cells, a selective double lipid membrane protects and separates the cell interior from the outside [1]. Membrane proteins allow an interaction with the outside [3], [5]. Membrane receptor proteins, for example, are responsible for inside-outside signaling, whereas transport proteins exchange molecules or ions with the outside and cell adhesion molecules (CAMs) control the communication with the surrounding. Furthermore, CAMs are highly relevant for the linkage of cells to other cells or their surrounding [5], [6]. Inside the cell, a cell nucleus contains all genetic information that is necessary for reproduction and construction of other cell components. These so-called reaction spaces synthesize proteins, provide energy or regulate pressure within a cell [1]. The cytoskeleton serves as support structure of a cell and is responsible for the transportation and distribution of substances and information [7]–[9]. It consists of actin, intermediate filaments and microtubules [1], [7], [9]. Microtubules are the highways of a cell and responsible for the transport within the cell [1], [10]. Actin filaments contract muscles, whereas intermediate filaments give structural support [1], [9].

Cells are surrounded by a composition of glycoproteins (e.g., collagen, fibronectin, laminin, elastin) and proteoglycans in form of a complex support structure that is called extracellular matrix (ECM) [1], [7]. Cells permanently interact with the ECM and an impaired interaction between cells and their ECM can affect many biological processes including cell adhesion, migration and differentiation [7], [8], [11].

1.1.1 Cell Adhesion

For survival, many cells need a physical connection to another cell or the ECM [8], [11], [12]. This so-called cell adhesion is essential for cell communication and regulatory processes such as growth, division, differentiation and apoptosis [7], [13], [14], thus proving an essential role for diseases and medical applications [7], [15]. In wound healing, for example, a fast but light adhesion is initially required to recruit leukocytes to the wound but reinforcement of cell adhesion over time is necessary to seal the wound [16]. In cancer, on the other hand, cell adhesion is often reduced and/or the expression of cell adhesion molecules impaired, which can both promote metastatic behavior [13], [17].

Cell adhesion is a dynamic process of formation and disassembly of connections between a cell and its surrounding [10], [18]. In contrast to chemical bonds, biological binding is based on molecular recognition and a lock-and-key principle [3], [19]. A pair of binding partners (receptor and ligand) resemble in shape (high structural affinity) to produce a tight bonding [3]. If necessary, this bond separates and the binding partners can be reused again [4], [20]. Ligands within the cell environment (e.g., fibronectin, collagen) bind to receptors (e.g., transmembrane CAMs such as integrins) at so-called cell junctions (see Figure 1.1) [2].

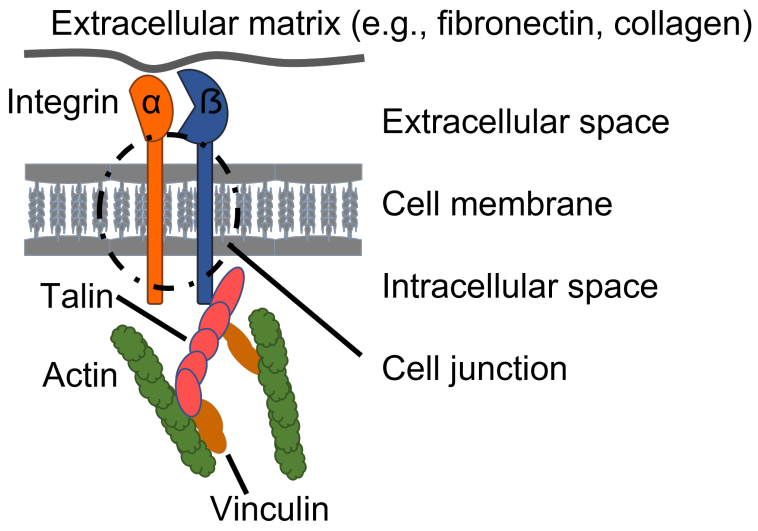

Figure 1.1: Visualization of receptor-ligand binding. Transmembrane cell adhesion molecules, such as integrins, bind to proteins of the extracellular matrix (e.g., fibronectin, collagen) at cell junctions. In the intracellular space, the connection of integrins to the actin cytoskeleton is realized through the binding of adhesion proteins (e.g., talin, vinculin) [2], [21]. Inspired by [22].

In addition to the anchoring junctions relevant for cell adhesion, there are communicating and occluding junctions [23]. Occluding junctions generate barriers with selective permeability [15], [22]. Communicating junctions guarantee chemical and electrical signal transduction [2]. In animal tissues, anchoring junctions can be found especially in regions of large mechanical stress (e.g., heart muscle, skin epithelium) [2] and generate cell-ECM or cell-cell connections depending on the type

of transmembrane protein family. Anchoring junctions formed by a cell-cell connection are called adherens junctions and link cells together through transmembrane proteins of the cadherin family [2], [24]. Focal adhesions, on the other hand, refer to anchoring junctions through cell-ECM connections formed by integrins [2], [15].

During initial adhesion, single receptor-ligand bonds [8] and unspecific interaction of ECM and the cell's glycocalix exist. Since these bonds are weaker than covalent bonds, a binding and breaking can simply occur due to thermal fluctuations [3], [20]. However, the initial binding of receptor and ligand leads to an intracellular signal cascade to recruit more integrins to the cell junction (i.e., binding site) [8], [20], [25]. After the recruitment of integrins to a cell junction, an adhesion cluster is formed, where external stresses can be distributed over multiple integrins and makes it more probable that broken bonds rebind before their receptors diffuse out of the adhesion complex [20], [26]. To establish stable focal adhesions, the intracellular part of the integrins attach to the actin cytoskeleton [8], [21] through adhesion proteins such as paxillin, talin, vinculin or zyxin (see Figure 1.1) [2], [3], [27]. Focal adhesions are highly regulated structures with lengths of 2-6 µm [28] that allow signal transduction between cell and ECM [10], [29], [30]. For instance, focal adhesions forward information about the state of the ECM to cells (e.g., stress distribution, deformations) and are involved in force-sensing mechanisms [20], [27], [31].

1.1.2 Mechanotransduction

A cell's environment can be diverse. The stiffness, topography or thickness can vary [11]. For instance, the stiffness of brain tissue is multiple magnitudes lower than bone tissue [32] or the epithelial tissue consists of densely packed cells of different structures (e.g., cuboidal, columnar, stratified) [33], [34], whereas blood mainly contains three types of floating cell types (erythrocytes, leukocytes, thrombocytes) [2]. Also, cells are subjected to a variety of forces [7], [35], [36]. For instance, the bloodstream causes shear forces to cells in blood vessels [12], [35], cells of the heart and lung experience contractile forces due to breathing [37], whereas blood pressure stretches the blood vessel wall [12]. At adhesion sites, cells can exert forces to actively interact with their environment [38]. For instance, these so-called traction forces facilitate cell migration [39], allow the sensing of environmental cues such as elastic or topographic properties [7], [38] or can open ion channels within the cell membrane [40]. Furthermore, the level of traction forces may scale with the cell type [11], [38]. For instance, it was shown that neuronal traction forces can be weaker than traction forces of fibroblast cells [41], whereas epithelial cells can in turn exert larger traction forces than fibroblast cells [38].

A cell's ability to exchange signals with its surrounding and to adapt its behavior accordingly is essential for our survival and the functionality of organisms with a high degree of switchability and dynamics [2], [11]. For many decades, the research focus was on biochemical cues such as protein structures [42] but since several years, it became evident that mechanical cues such as external forces, stiffness variations or topographic properties are equally significant [7], [11], [43], [44]. Mechanotransduction describes a cell's ability to respond to mechanical cues by transmission of

an external stimulus to specific structures and its translation into biochemical signals [12], [35], [36]. However, the involved mechanotransduction pathways are not fully understood yet [12], [27], [42]. Existing knowledge about mechanotransduction indicates that a better understanding of this subject will initiate new strategies for early disease detection, prevention of disease outbreaks or disease treatments [8]. For instance, the physical properties of tissues often change in disease [11], which can be utilized in early disease detection. Findings about the role of substrate stiffness for cell behavior will have an impact on the design of implant materials [7]. Additionally, deeper understanding of mechanotransduction will not only reduce the mismatch between the rather static *in vitro* and the very dynamic, reversible *in vivo* conditions [45] but reduce the number of necessary *in vivo* experiments, which is ethically favorable. Ultimately, this knowledge will affect a plethora of diseases such as deafness, muscular dystrophy, heart disease or cancer [12].

Although responsive behavior of proteins is often related to biochemical regulation, there are many proteins and biological systems that can be mechanically activated over a broad range of time scales (seconds to hours) [12], [27]. For instance, some proteins undergo a structural change upon external stimulation that can result in a functional change [10], [46], [47]. Allosteric regulations, for example, describe a force-induced conformational transition of proteins from a weakly bound state towards a state with higher binding strength that can act as so-called catch bonds [46]. In general, catch bonds describe bonds that strengthen upon applying tensile forces [48], which means that the lifetime is increased under tensile forces in contrast to slip bonds that decrease its lifetime [20], [46], [48].

Cells developed a variety of strategies to adapt their adhesion to external stimuli. Such concepts include direct strengthening of adhesion molecules (higher affinity) or enhanced avidity (number of available adhesion molecules) [4], [49]. But also the properties of the cellular anchor of an adhesion molecule can be altered, external loads can be distributed over multiple adhesion molecules [4], [20] or conformational changes can provide additional binding sites (e.g., talin unfolding to achieve vinculin binding) [20], [47], [50]. All these factors allow a fast and efficient remodelling of the cytoskeleton [7], [11]. This is, for example, highly relevant to guarantee fast reactions to blood shear flows or infections [7]. Cells use their focal adhesions to transform extracellular mechanical cues into a cellular response [28], [36]. For instance, integrin signaling and mechanosensitive ion channels are routes for mechanical signal transduction [10], [12], [51]. Additionally, it is believed that the cell nucleus is relevant for mechanotransduction [12], [27]. For instance, changes in the protein composition of the nuclear envelope influence nuclear deformability and can impair force transmission between nucleus and cytoskeleton [52].

Integrins

Integrins are an essential part of the adhesion complex responsible for biological functions, such as embryogenesis, immune response or inflammation, and they are generally accepted mechanosensors [6], [9], [29] that change between two affinity states in the presence of anions [4], [53]. Integrins are transmembrane proteins with

two subunits (α and β) that exist in different forms [6], [13], [15], [53]. Specific combinations of α and β bind to defined ligand partners [6], [9], [49]. For instance, $\alpha_5\beta_1$ specifically binds to fibronectin, whereas $\alpha_6\beta_1$ binds to laminin [4]. Mechanical stimuli can be used to improve and/or manipulate integrin clustering, ECM binding and/or the recruitment of focal adhesion proteins [29]. Hence, integrins have an essential role for mechanotransduction studies.

Mechanosensitive Ion Channels

In general, ion channels are membrane proteins that control the exchange of specific ions (e.g., calcium) across the cell membrane to regulate electrical signals or the cell volume [54]. The opening and closing mechanism (so-called gating process) of a certain ion channel can, for example, be controlled through voltage gradients, specific ligand binding or mechanical signals [2], [54]. The gating process of so-called mechanosensitive ion channels can be regulated through mechanical signals, such as stretch, pressure or shear [51], [55], [56]. Hence, they are an essential candidate to explain mechanotransductive behavior. Recently, a Nobel Prize was awarded to David Julius and Ardem Patapoutian for their discoveries of ion channels as receptors for temperature and touch [57]. This shows the ongoing research focus on mechanotransduction and the necessity to gain a comprehensive understanding of mechanotransduction pathways.

Multiple mechanosensitive ion channels have been discovered in various organisms (e.g., Piezo1, Piezo2, TRPV4, TRPM7, TMEM87a) [58]–[60]. Piezo1 exists in different cell types, such as endothelial cells or red blood cells, and in several organs (e.g., stomach, lung, bladder) [54], [61], [62]. Piezo1 has a propeller-like structure that forms a calcium selective pore [61], [63], [64], where calcium influx can be activated through force application [51]. Piezo1 proved to be essential for different functions and developmental steps [56], [63]. For instance, impaired development of the vascular system in Piezo1-deficient mice embryos is lethal [56], [64]. In addition, Piezo1 showed its significance in several diseases (e.g., metastasis [65], hemolytic anemia [61], pancreatitis [62]) and in inflammatory responses of the immune system [66].

1.1.3 Single Cells to Complex Tissues

Many cell functions are based on single cell behavior. However, cells specialized on specific skills and functions to build complex structures, such as the human body [1], [7]. For instance, neurons are designed for electrical signal transmission throughout the body [2], whereas bone tissue is specialized to bare high compression forces [7]. A network of cells with the same specialization is called tissue [1] and there are four different tissue types in animals: epithelial, connective, muscular and nervous tissue [1], [2]. Epithelial cell layers build the epithelial tissue covering all inner and outer organ surfaces [1], [2]. This forms a protective barrier against invasion of foreign substances or fluid loss [2]. The connective tissue is an important support structure in the whole body. It gives organs stability, strength and elasticity [2].

Muscular tissue allows muscle movement and contractions. For instance, skeletal muscle cells move the limbs or the cardiac muscle guarantees blood flow through the body. In the nervous tissue, neurons ensure signal transduction and glial cells have a support function and organize sufficient nutrients [1]. In all tissues, cell adhesion is an essential process as it permits the diverse and dynamic formation of cellular structures into organized structures [15].

Fibroblast Cells

Fibroblast cells are a major component of the connective tissue [2]. They are not fully differentiated cells, which means that they can differentiate into other cell types such as fibrocytes or epithelial cells and their main task is the synthesis of ECM proteins [67], [68]. Fibroblast cells grow to oval-shaped cells with many long irregular cytoplasmic extensions to communicate with each other [68], [69].

Fibroblast cells have an essential role for wound healing, tumor growth and skin regeneration [2], [70]. For instance, in skin, fibroblast cells provide strength and permeability producing collagen and elastin, which are essential for the resistance and elasticity of skin [71]. However, the activity of fibroblast cells decreases with age or external factors, such as UV radiation, resulting in a reduced collagen production that often leads to loss of moisture storage [71]. During wound healing, tissue injury stimulates the proliferation of fibroblast cells and the release of cytokines to support the damage repair. Here, collagen serves as a temporary wound closure until the contraction of so-called myofibroblast cells (i.e., a special form of fibroblast cells due to cytokine release) leads to a stable wound closure. However, incorrect production of myofibroblast cells can have severe medical implications (e.g., impaired wound healing, tumor growth) [68], [70]. In addition, fibroblast cells allow the development of *in vitro* models for the formation of new blood vessels from existing ones (so-called angiogenesis) [67]. Hence, fibroblast cells are of great interest for aesthetic and medical applications.

Fibroblast cells belong to the group of cells that were first reported to show mechanosensitive behavior [11]. For instance, the behavior of fibroblast cells correlates with the stiffness of their environment [11], [72]. On soft substrates, fibroblast cells show diffuse, dynamic adhesion complexes, whereas they form stable focal adhesions on stiff substrates [11]. This stiffness response is also reflected by their durotactic behavior (i.e., migration towards stiffer regions of a material) [73]–[75]. Fibroblast cells are even able to adapt their own stiffness according to the stiffness of their environment [72].

Their medical relevance and mechanosensitive character in addition to the uncomplicated cultivation in the laboratory make fibroblast cells the perfect candidate as a model cell for many mechanotransduction studies.

Human Embryonic Kidney Cells

In the 1970s, Graham et al. succeeded to transform human embryonic kidney (HEK) cells with sheared deoxyribonucleic acid (DNA) fragments of human adenoviruses (adenovirus type 5) and established the stable HEK293 cell line [76]–[78]. At that time, it was the only adenovirus transformed human cell line [76]. Although HEK293 cells have epithelioid character [76], they also exhibit neuronal character [79], [80] and their gene expression profile shows no specificity for a certain tissue [78], [79]. For instance, markers for neuronal cells and adrenal gland were observed [78]. Hence, HEK293 cells may not show typical behavior of kidney cells [79].

However, versatile transfection of HEK293 cells and good cell culture maintenance make them a preferred host for expression of recombinant proteins [77]. Hence, HEK293 cells became, in addition to HeLa cells (named after Henrietta Lacks), one of the most commonly used cells in cell biology studies [78]. For instance, HEK293 cells have been utilized investigating neurotropic viruses (e.g., poliovirus, rabies virus) [80], [81] and/or developing adenovirus vectors [82].

Dr. Kate Poole and her working group used transfected HEK293 cells to investigate the role of different mechanosensitive ion channels (e.g., Piezo1, TMEM87a) [51], [55], [60]. The absence of functional TMEM87a (renamed to Elkin1) in melanoma cells, for example, hinders mechanoelectrical transduction and cell motility [60]. Piezo1 is essential in disease progression (e.g., metastasis, hemolytic anemia) and inflammatory responses of the immune system [61], [65], [66].

1.2 Biofunctional Soft Materials

Since many cells react to environmental cues, the understanding of mechanotransduction and its underlying processes will help the development of biomaterials with different properties for different application fields [8]. For the realization of reliable *in vitro* studies, materials that represent the natural environment as precisely as possible are necessary [83]. For instance, cells experience various stiffness values ranging from less than 1 kPa in the brain to several GPa in bone tissue [11], [26], [32] and many cell processes are directly linked to substrate stiffness (e.g., cell proliferation and migration) [44], [75]. The stiffness of a material can, for example, be utilized to control the differentiation of stem cells into a desired tissue [84]–[88]. In addition, very soft substrates can prevent the formation of focal adhesions for some cells, whereas stiff substrates can support the formation of strong focal adhesions and actin stress fibers [38], [43], [88]. Thus, materials with variable stiffness that precisely mimic the physiological conditions of the relevant cells are required [26], [89]. Other material preferences are: cheap and easy production, optical clarity, inertness, non-toxicity and consistent properties that can easily be regulated (e.g., elasticity). Also, a versatile biofunctionalization with adhesion proteins is favorable to guarantee reliable cell-material interactions [90].

Over the years, a variety of materials has been developed [8], [91]. Commonly used examples are agarose [8], alginate [92], collagen [93], matrigel [8], polyacrylamide

(PAM) [94] or polydimethylsiloxane (PDMS) [91], to name some examples. However, usually not all of the abovementioned criteria are satisfied by one material. Hence, it is necessary to choose a material with regard to its suitability for a specific application field or requirement (e.g., elasticity, topography, biodegradability).

1.2.1 Polyacrylamide

Polyacrylamide (PAM) is a soft material that swells in water up to 90 % (so-called hydrogel) without dissolving [95]. Its porous network consists of crosslinked monomer chains that mimic the scaffold structure of the ECM [83]. PAM is produced from a mixture of acrylamide monomers and bis-acrylamide crosslinkers [44]. In addition, N, N, N', N'-tetramethylethylenediamine (TEMED) and ammonium persulfate (APS) are added to initiate a free radical polymerization [90], where oxygen inhibits the polymerization process [96], [97]. Hence, it is important to eliminate all oxygen from the solution prior to initiation of the polymerization [96]. In the end, a covalent network of long acrylamide chains with statistical crosslinks of bis-acrylamide is formed [90].

The mixture of acrylamide with different ratios of bis-acrylamide allows easy production of variable elasticities without alterations of the chemical properties [43], [83], [96]. The range of elasticities covers many physiological relevant tissue stiffnesses (ca. 1-100 kPa) [7], [42] but even elasticities of up to 740 kPa have been produced [42]. PAM has a high optical quality allowing microscopic investigations with no or less fluorescent effects [83], [96]. Disadvantageous for PAM is the non perfectly elastic behavior [87], [98]. Yet, PAM shows linear deformation for a large range of stress and recovers quickly once the stress is released [83], [87], [98].

1.2.2 Biofunctionalization

Although many cell types attach unspecifically to some materials (e.g., glass) [3], most materials require a coating with adhesion proteins such as fibronectin or collagen (so-called biofunctionalization) to promote or enable cell adhesion [96]. There are different possibilities to functionalize a material with specific adhesion proteins [87]. To guarantee a stable connection between a material and adhesion proteins, the materials used may need a modification (e.g., incorporation of molecules). For instance, acrylic acid N-hydroxysuccimide ester (a-NHS) can be added to a PAM solution prior to polymerization to allow a biofunctionalization with adhesion proteins [90]. In addition, a method called micropatterning allows functionalization of defined areas of a material [99], which is, for example, relevant for investigating the role of ligand densities for specific cell responses (e.g., cell spreading area) [14], [100]. To guarantee specific cell binding to glass surfaces, they can be treated with oxygen plasma to generate a negatively charged surface of OH^- groups. Then, the backbone of poly-D-lysine (PDL) or poly-L-lysine (PLL) can electrostatically bind to the glass surface and after treatment with glutaraldehyde, a stable coating with fibronectin can be realized [3], [101].

1.3 Atomic Force Microscopy

Mechanotransduction studies concentrate on how cells are affected by environmental cues, the measurement of forces exerted by cells or goal-oriented manipulations of cells and their behavior [102]. In the last decades, various techniques have been developed for investigating mechanotransduction. Atomic force microscopy (AFM), flow chambers [8], biomembrane probe [3], [8] or microneedle assays [39] are well-known techniques used to actively apply external forces to living cells, whereas changes of the cell environment such as material stiffness or drugs rather affect cells indirectly. In addition, traction force microscopy (TFM) allows the measurement of so-called traction forces to gain knowledge about how cells actively interact with their environment [8], [103], [104]. Techniques such as optical [8], [105] and magnetic tweezers [105] are commonly used to measure small interaction forces (e.g., single molecule forces) [3] or to apply forces to cells (e.g., manipulation with small beads). Since the invention of a cell balance with millisecond time resolution and picogram mass sensitivity by Martínez-Martín et al., it is even possible to measure the total mass of single or multiple adherent cells [106].

Among these techniques, AFM has emerged since its invention by Binnig, Quate and Gerber in 1985 as a versatile technique with outstanding properties for the investigation of mechanotransduction [8], [107]. Besides atomic resolution of surface topographies [108], a diversity of experiments can be conducted under physiological conditions (i.e., body temperature, fluids) without restriction of the cell type or adhesion molecules investigated [8], [108], [109]. Additionally, AFM can easily be combined with optical microscopy allowing the observation of cellular structures simultaneously to force or height measurements [8].

The general concept of AFM is the measurement of interaction forces between a sample and a force sensor (so-called cantilever) to gain knowledge about properties of the sample (e.g., topographic, elastic or adhesive properties) (see Figure 1.2) [108]. Such a cantilever is considered as a Hookean spring with a spring constant k [22]. Various possible spring constants allow measurements with a large force range from 10-10^6 pN [3], [109]. More precisely, a laser beam is directed to the cantilever tip and reflected to a position sensitive photodiode (see Figure 1.2 a)) [108]. Once the cantilever interacts with the sample surface, the cantilever deflects and the position of the laser spot on the photodiode is shifted, which is translated into the desired output signal (e.g., force or height signal) [108]. The imaging mode is generally used to extract information about the topography of a sample. Depending on the application, three different modes are available to control the exact interaction between a sharp tip at the cantilever front and the sample (i.e., contact, non-contact and intermittent/tapping mode) [108]. To record a complete image, the cantilever scans over a predefined region of the sample [108].

In the force spectroscopy mode, the force signal can be used to determine sample properties, such as elastic or adhesive properties. In contrast to imaging, the cantilever measures at single points or records point-to-point curves. These so-called force-distance curves display the force signal as a function of the distance between cantilever and sample. An example force-distance curve is shown in Figure 1.2 b). In

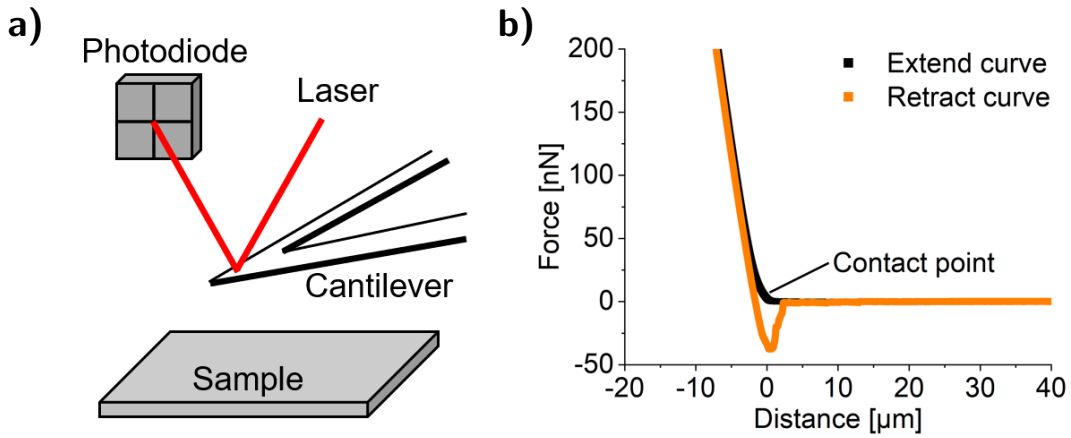

Figure 1.2: General visualization of an AFM setup to record force-distance curves. a) A laser is directed to a cantilever and reflected to a photodiode. The laser spot position deviates from the center of the photodiode according to interaction forces between cantilever and sample. b) The system measures the cantilever deflection translated into force as a function of distance between cantilever and sample. The resulting curve is called a force-distance curve. The approach curve (also called extend curve) contains information about elastic properties of a sample. The retract curve can be used to determine adhesive properties.

principle, a force-distance curve can be divided into three parts: approach, contact phase and retract.

Initially, a defined gap between cantilever and sample exists. Then, piezoelectric motors with subnanometer precision [108] move the cantilever towards the surface at a constant speed until a predefined setpoint force (i.e., defined cantilever deflection) is reached. The contact point is defined as the distance at which the force deviates from zero the first time (see Figure 1.2 b)). The additional movement towards the sample until the setpoint force is reached describes an indentation of the sample (so-called indentation depth). During the contact phase, the cantilever is usually kept at a constant force for a defined time (so-called contact time). Afterwards, the cantilever movement is reversed and the cantilever is retracted from the sample. The cantilever usually sticks to the sample surface due to adhesive properties of the sample. However, once the retract force is great enough, the cantilever snaps back to zero force.

The approach curve (or extend curve) of force-distance curves is often used for the determination of Young's moduli of soft materials, cells or cellular structures. This type of measurement is called AFM-based microindentation (see Section 1.3.1). The retract curve is widely used to measure interaction forces between single cells and multiple cells or materials. These experiments are called single cell force spectroscopy (SCFS) and explained in Section 1.3.2 [3].

1.3.1 AFM-based Microindentation to Determine the Elasticity of Soft Materials

Cells are able to sense and react to external forces and environmental cues, such as elastic or topographic properties [7], [12], [43], [44]. Both precise control and reliable measurement of elastic properties are crucial. Many techniques have been developed to measure material properties, such as AFM-based microindentation, nanoindentation, rheology and tensile testing. In tensile testing, a material is usually under uniform tension until failure and the Young's modulus of the material is determined from the linear region of the loading curve [110]. Rheology can be used to measure viscoelastic properties of a given material usually placed between two plates or a cone and a plate [111]. The upper plate or the cone is subjected to a defined rotation, while the material response is measured in terms of shear moduli [111]. The relation between storage and loss modulus determines whether a material is elastic or viscous [111]. Nanoindentation, often used for measuring hardness, indents a given material with a sharp indenter of known shape up to a defined indentation force or depth at high spatial resolution [112], [113]. In contrast to conventional hardness measurement techniques using microscopic images, material properties determined with nanoindentation (e.g., Young's modulus) are extracted from the loading-unloading curves [112], [114].

State-of-the-art techniques, like rheology or tensile tests, rather determine elastic properties on a macroscopic scale than on a microscopic scale. However, cells interact on a microscopic scale with materials [14], [20], [115] and the measurement method itself may affect the Young's moduli determined [87]. Nanoindenters can measure on the microscale but induce very high strains to the material indented, which might alter the outcome of the measurements. AFM-based microindentation enables semi global (i.e., creation of elasticity maps) and microscopic measurements with piconewton precision [3], [109]. An AFM is usually combined with light microscopy, a heating system and a chamber for measurements in liquids. This allows the determination of elastic properties under physiological conditions and consequently the quantification of cell mechanics (e.g., stiffness of different cell types) [72].

During such AFM-based microindentation experiments, a cantilever with a well-defined probe (so-called indenter) is pressed into a sample up to a predefined set-point force. An elastic theory (i.e., mathematical fitting model) is applied to the approach curve of the recorded force-distance curve to determine the Young's modulus of the sample. Different elastic theories have been developed to predict the relation between indentation depth and force. The most well-known ones are the Hertz, Johnson-Kendall-Roberts (JKR) or DMT (after Derjaguin, Muller and Toropov) [84], [116], [117]. While JKR and DMT include adhesion between probe and sample, the Hertz model neglects it [84], [116]–[118].

The Hertz model can be employed for different indenter shapes (e.g., spherical, parabolic, conical) [119]. Usually a stiff spherical indenter is attached to the cantilever and the equation for a parabolic shape is used to reduce the mathematical complexity (applicable for small indentation depths, see Equation (1.1)) [87].

$$F = \frac{4\sqrt{R}}{3} \frac{E}{1-\nu^2} d^{3/2} \tag{1.1}$$

Where F is the indentation force, R is the radius of the indenter, E is the Young's modulus, ν is the Poisson's ratio and d is the indentation depth defined as:

$$d = |d_{max} - cp| \tag{1.2}$$

where d_{max} is the distance value of the cantilever position at maximum indentation force and cp is the distance value of the cantilever position at the contact point. This relation is visualized in Figure 1.3. The cantilever movement starts at a distance value of 100 µm (convention of the AFM setup). With decreasing cantilever-sample distance, the distance values displayed also decrease. Hence, the distance value of the cantilever position at maximum indentation force is the lowest. Then, the indentation depth can be calculated from the absolute value of the difference between distance values at the contact point and the maximum force.

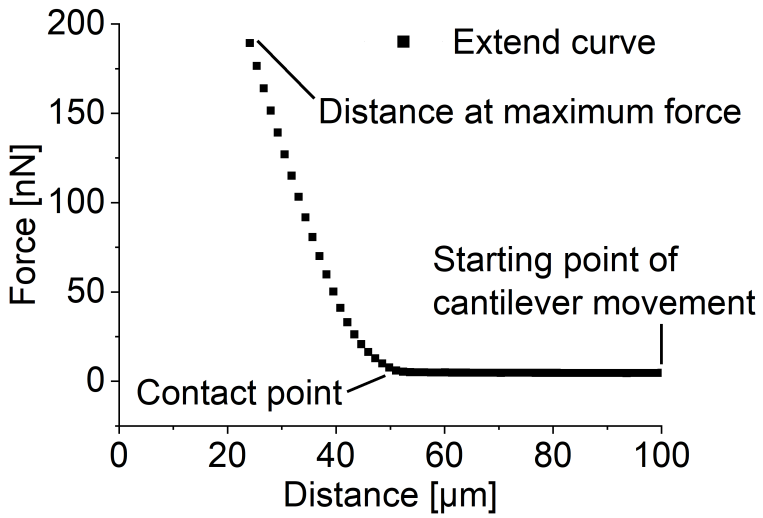

Figure 1.3: Visualization of the calculation of indentation depths. The example extend curve demonstrates the calculation of an indentation depth. The cantilever movement starts at a distance value of 100 µm (convention of the AFM setup) and the distance values displayed decrease with decreasing cantilever-sample distance. Hence, the distance value of the cantilever position at maximum indentation force is the lowest. The indentation depth can be calculated from the absolute value of the difference between distance values at the contact point and the maximum force.

A common drawback of most elastic theories is the use of assumptions that do not entirely hold. Especially hydrogels and other biomaterials often lack isotropy and homogeneity. Additionally, exact knowledge about the forces between indenter and sample is difficult to quantify or determine [117], [120]. Still, AFM-based microindentations allow the reduction of effects due to sample inhomogeneity. The recording of elasticity maps, for example, is a strategy to improve the outcome of

such experiments. However, this usually requires time-consuming analysis of huge data sets. Chapter 2 describes the development of a useful strategy to increase the overall reliability of AFM-based microindentations.

Furthermore, not all materials investigated are entirely elastic but show viscous behavior, too. Varying indentation speeds can reveal viscoelastic behavior and affect the Young's modulus determined. However, experimental details like the indentation speed are often missing in the literature. To address the importance of experimental details and stating them in scientific publications, I discuss the influence of different experimental details in Chapter 2.

1.3.2 Single Cell Force Spectroscopy to Characterize Cell Adhesion

The knowledge about cell adhesion is an integral part towards a better understanding of mechanotransduction. Forces are a common measure for the quantification of cell adhesion [103]. For instance, the forces exerted by cells, so-called traction forces, show how cells actively interact with their surrounding [38]. Forces necessary to induce cell reactions or rupture adhesion complexes provide insights into cell adhesion strength, cell viability and/or cell-material compatibility [8], [121]. This helps to determine the quality of implant materials (e.g., expected rate of tissue acceptance) [122], [123] or drug treatments for diseases [8]. Furthermore, it allows the characterization of different stages of cancer cells and the establishment of biomarkers to diagnose diseases at an early stage [8]. In principle, the inclusion of all such forces is necessary to achieve full perception of mechanotransduction and related processes.

There are multiple methods to measure cell-cell or cell-material interactions. For instance, centrifugation assays or flow chambers permit the measurement of cell detachment of multiple cells under shear stress [8]. Since intensity gradients of a strongly focused laser beam attract small objects towards the focus of the beam, so-called optical tweezers have been developed to trap and/or manipulate nano- to micrometer-sized objects with forces up to 100 pN [105], [124], [125]. AFM single cell force spectroscopy (AFM SCFS) is a versatile technique with an exceptional force range (10-10^6 pN) that enables the measurement of cell-material interactions under physiological conditions [3], [109]. This facilitates the measurement of living cells, which is essential as some cellular reactions (e.g., connection between transmembrane adhesion proteins and actin cytoskeleton) cannot be observed with dead cells [7].

In this thesis, I employ different strategies to measure cell detachment with AFM SCFS. For this purpose, a single cell that is attached to the front of a functionalized tipless cantilever serves as a probe (see Figure 1.4 a)) [3], [4]. The basic measurement (so-called "normal" mode) consists of the previously described parts (i.e., approach, contact phase and retract, see Section 1.3) to record a force-distance curve. For the approach, the cell is pressed onto a substrate (e.g., material, cell) until a predefined setpoint force (usually 0.5 nN) is reached. After a defined contact time (seconds to

minutes, see Figure 1.4 a) Contact phase), the cantilever is retracted to completely detach the cell from the surface (see Figure 1.4 a) Retract). The retract curve of the recorded force-distance curve contains the relevant information about the interaction forces between the cell and the substrate (see Figure 1.4 b)).

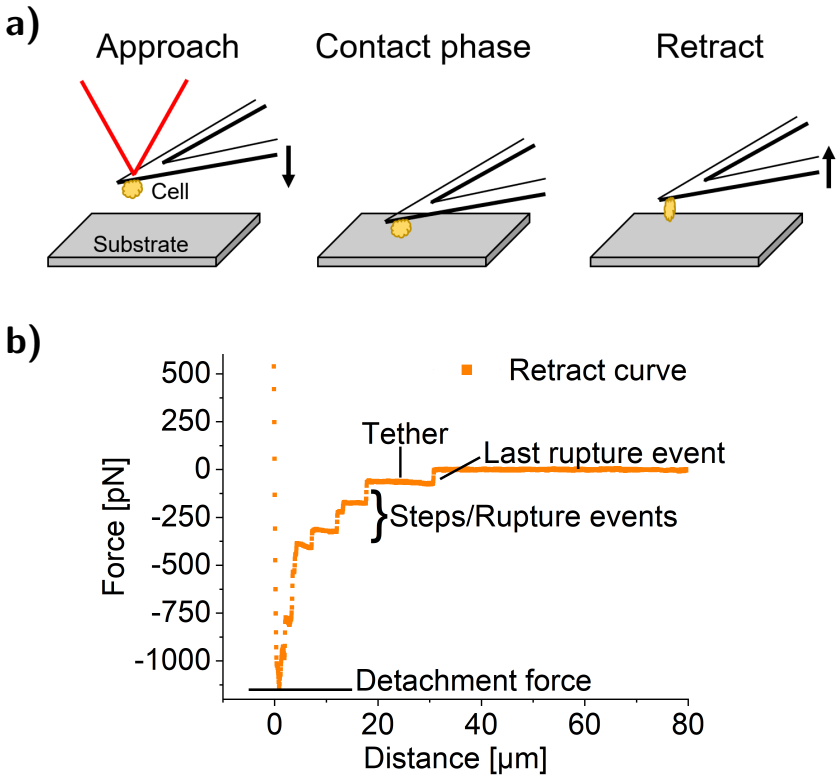

Figure 1.4: General visualization of AFM single cell force spectroscopy. a) During approach, the cantilever presses the cell on to the substrate until the setpoint force is reached. The contact phase takes a few seconds to minutes while the cantilever is kept at constant force to guarantee a steady cell-substrate interaction. Finally, the cantilever is retracted to detach the cell from the substrate. b) Example force-distance curve that contains the relevant information about the cell-substrate interaction (e.g., detachment force, last rupture event). A tether depicts a plateau region prior to a rupture event.

A closer look at the retract curve shown in Figure 1.4 b) reveals specific points and regions of interest. Once the cantilever starts to retract, the force load is released from the cell and the measured force intersects zero force at the contact point. With further cantilever retraction, an increasing negative force occurs due to cell-substrate interactions. The linear relation between force and distance mainly results from elastic cell stretching [4], [26]. The minimum of the force-distance curve is reached at a critical pulling force (so-called detachment force) that roughly gives the total cell adhesion strength [4]. Then, a step-like pattern (i.e., sudden decrease in force) illustrates rupture events of receptor-ligand bonds (see Figure 1.4 b)).

The height of a step is a measure for the adhesion strength of the ruptured bonds [3], [126]. These steps can result from multiple bond ruptures or neighboring bonds can partially adopt the force load, which leads to a smaller height [126]. Additionally, a functionalization with a lectin such as concanavalin A (conA) may be interpreted as

receptor-ligand rupture, which complicates the interpretation of rupture events [3]. However, the last step (so-called last rupture event) is generally considered a single receptor-ligand bond rupture but can also result from several bonds rupturing at the same time [3], [126].

The distance of a single receptor-ligand bond rupture is a measure for the bond lifetime since

$$t_{bond} = d_{rupture}/v \tag{1.3}$$

where t_{bond} is the bond lifetime, $d_{rupture}$ is the distance of the bond rupture and v is the pulling speed [3], [22]. The distribution of bond lifetimes allows investigation of biological bond kinetics [3], [22].

The slope of a plateau region preceding a step indicates if a tight connection to the cytoskeleton existed. A stable connection to actin (e.g., typical for matured focal adhesions) is displayed by a steep negative slope [4], [126]. A horizontal plateau (slope close to zero) means that the receptor was only attached to the cell membrane [4] and leads to an extraction of viscous tubes (so-called tethers) that hinder bond rupture [3]. A tether can act as force clamp [3], [4], which keeps the loading rate at almost zero (see Equation (1.4)) [3]. Furthermore, the force remains less than the bond breaking level [4]. Hence, the detachment energy (dissipated energy during cell-substrate separation [3]) increases linearly for a very long pulling distance [4].

$$r = dF/dt = 0 \tag{1.4}$$

Where r is the loading rate, F is the setpoint force and t is the time.

The strength of biological bonds increases logarithmically with increasing loading rate, which makes the loading rate an essential parameter for adhesion force measurements [127], [128].

Chapter 2

Mechanical Characterization of Biomaterials with AFM-based Microindentation

2.1 Introduction

Many cells show mechanosensitive behavior, where the stiffness has an extraordinary role. For instance, the differentiation of stem cells into different tissue types due to variable substrate stiffness is a common example [84]–[88] but also the beating of cardiomyocytes is affected by the stiffness [129], [130]. Two main factors are of great importance for mechanotransduction studies: The availability of suitable materials and reproducible techniques for the characterization of these materials. More precisely, materials are necessary that possess desired material properties and/or can easily be adapted to them [89]. For instance, materials that precisely mimic the extracellular matrix are of interest [94], [131]. On the other hand, reproducible and quantitative techniques to measure the material properties are required to fully predict and understand their interactions with cells or tissues [117].

Although AFM-based microindentation stands out compared to other common characterization techniques like nanoindentation, rheology, there are some drawbacks that make the measurements inconsistent and/or difficult to compare. Drawbacks are mostly related to technical issues (e.g., cantilever calibration, fitting model) or missing information (e.g., insufficient details in scientific publications) [87]. To calculate the Young's modulus from AFM-based microindentation data, a mathematical fitting model is applied to the data. These elastic theories, such as the Hertz model, usually need strong assumptions such as substrate homogeneity and isotropy or exact knowledge about the forces between the substrate and the measuring device [117], [120]. However, these assumptions are often not entirely met for soft materials that are usually used as biomaterial [120]. Other elastic models exist to overcome some of the Hertz models' disadvantages (e.g., DMT or JKR [117], [118]). Yet, the Hertz model is still the most commonly used elastic model to characterize elastic properties of hydrogels [84], [117]. The scientific community apparently prefers to work with many approximations instead of choosing more sophisticated models. This makes a full statement of all experimental parameters necessary. However, detailed descriptions such as indentation force or speed are often not specified in publications,

which hinders reliable comparisons between works of different research groups [132]. Most of the developed improvements of the Hertz model instead concentrate on descriptions of more complex force interactions between the substrate and the indenter (e.g., adhesive forces [118]) or on corrections for the experimental designs (e.g., thin film substrates [98]) instead of focusing on considerations regarding the inhomogeneity, anisotropy of soft materials or the reliability of measurements.

A major advantage of AFM is the ability to measure multiple indentation curves at different positions of a sample to reduce effects due to sample inhomogeneity. Furthermore, a variety of experimental parameters like indentation force or speed can easily be applied and possible alterations of Young's moduli can be revealed. However, recording a large number of indentation curves leads to effortful data analysis. Although most of the analysis can be automated, the impact of the indentation depth on the Young's modulus measured is not incorporated in standard AFM analysis software until now. Buxboim et al. showed for PAM (most commonly used hydrogel in biophysical research [87]) that the Young's modulus depends on the indentation depth [133]. It is inevitable that knowledge about the role of the indentation depth for the elastic response of a material is essential [87]. These factors underline the lack of standardized measurement settings that also consider the dependence of the Young's modulus on the indentation depth and make the need for more sophisticated experimental procedures with statistical approaches obvious.

I here present the development of a self-made algorithm to automatically analyze AFM-based microindentation data (see Section 2.3). This algorithm calculates Young's moduli for different indentation depths of one measurement cycle (i.e., one indentation curve). The result is a so-called *E-d* curve that displays the Young's moduli calculated as a function of indentation depth. Then, the algorithm detects Young's moduli in a region without dependence on the indentation depth. Hence, the role of the indentation depth on the Young's modulus calculated is considered. Additionally, the algorithm chooses that Young's modulus calculated with minimized fitting error. These considerations increase the reliability and comparability of such indentation measurements.

I prove the added value of our new algorithm through a systematic investigation of how different experimental parameters affect the outcome of the measurement of elastic properties of PAM samples (see Section 2.4). The display of the *E-d* curves generated is essential to guarantee a reliable investigation of the impact of various experimental parameters. We employed the commonly used Hertz model as proof of principle, but our algorithm can be adapted to other, more sophisticated fitting models. Finally, I elaborate the diverse elastic characterization of soft materials and biological samples with AFM-based microindentation.

2.2 Experimental Design

In this thesis, small and stiff beads attached to tipless cantilevers were used to indent soft materials up to a defined setpoint force (see Figure 2.1 a)). During this process, force-distance curves were recorded at different positions of the samples. The Hertz

model was fitted to the extend curve of the force-distance curves to calculate the Young's modulus of the materials.

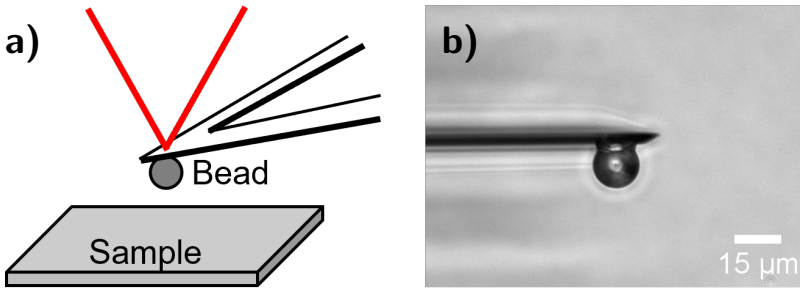

Figure 2.1: Setup of AFM-based microindentation experiments. a) Single stiff beads were attached to tipless cantilevers and used for the indentation of soft samples with defined setpoint forces and indentation speeds. b) Representative image of a successful bead attachment with homemade sideview cantilever holder.

2.2.1 Cantilever Preparation

The experiments were conducted on the CellHesion® 200 or the NanoWizard® 3 setup (see further details in Appendix B.1). Tipless cantilevers of type HQ:NSC35 (MikroMasch, Innovative Solutions Bulgaria Ltd.) were used. The spring constant of each cantilever was calibrated five times on glass in air with the thermal noise method implemented in the JPK control software. The averaged spring constants were used for the experiments (1.35-1.89 N/m). The sensitivities of the cantilevers were measured on glass in water directly prior to an experiment. Single beads were attached to the cantilevers with two component glue (UHU Plus Schnellfest or Endfest, UHU GmbH & Co. KG). Beads with diameters of 6.47 µm (glass, microparticles GmbH), 15.0 µm (polystyrene, Merck Millipore) or 21.82 µm (glass, microparticles GmbH) were used (diameters given by the manufacturers). A homemade cantilever holder was used to check the successful attachment of the bead from the side (see Figure 2.1 b)). For further details see [134].

2.2.2 Sample Preparation

Pretreatment of Glass Slides

A stable fixation of the materials used is necessary to realize reliable indentations. Glass substrate holders were used for indentations of PAM, because a fixation directly in a petri dish was not possible. Glass slides ($20 \cdot 20$ mm^2) were cleaned three times with ethanol and bidest. water, followed by an incubation in sodium hydroxide (NaOH, 2.5 M, Sigma-Aldrich) for 10 min. The glass slides were cleaned in bidest. water in an ultrasonic bath for 10 min and then rinsed with ethanol. Afterwards, the glass slides were incubated in a mixture of 97 % ethanol, 2 % 3-(Trimethoxysilyl)propyl methacrylate (Sigma-Aldrich) and 1 % acetic acid (Sigma-

Aldrich) for 15 min. In the end, the glass slides were twice shaken in ethanol for 5 min at 80 rpm and baked at 120°C for 1 h.

Production of Polyacrylamide

PAM samples were produced from a mixture of 1500 µl acrylamide (40 %, Bio-Rad Laboratories, Inc.), 900 µl bis-acrylamide (2 %, Bio-Rad Laboratories, Inc.), 25 µl APS (10 wt% in aqueous solution, Bio-Rad Laboratories, Inc.) and 2575 µl bidest. water. After degassing for 10-20 min in a desiccator, 7.5 µl TEMED (Sigma-Aldrich) was added to start the polymerization. Thin samples were produced by sandwiching 10 µl PAM solution between a $20 \cdot 60$ mm^2 coverslip and a pretreated glass slide. For the production of bulk samples, the PAM solution was added to custom-made Teflon™ molds with depths of 1 mm or 2 mm and were covered with pretreated glass slides. The polymerization time was 40 min. Before use, the samples were swollen in bidest. water for at least four days.

2.2.3 Indentation Experiments

Each sample was fixed to a petri dish (TPP® Techno Plastic Products AG) with biocompatible two component glue (Reprorubber®) and the sensitivity of the cantilever used was measured in bidest. water on a hard reference material prior to each measurement. 10 force-distance curves with up to 25 positions each were recorded in bidest. water with setpoint forces of 300-400 nN, indentation speeds of 0.1-100 µm/s, sample rates of 2050 Hz and pulling lengths of 10-50 µm.

2.2.4 Data Processing

The approach curves of the force-distance curves recorded were used to calculate the Young's moduli of the materials used. At first, the baseline and the tilt of the curves were corrected and the tip-sample separation was calculated with the JPK data processing software (version 6.1.104, JPK Instruments). A self-made MATLAB (version R2015a, The MathWorks®, Inc.) algorithm was used for an automatic calculation of the Young's modulus in a region where the Young's modulus was independent of the indentation depth. For this purpose, a least squares fitting function was used to fit the Hertz model to the force data. The Young's modulus and the contact point were the fitting parameters. The fitting process repeated with increasing fit range in each cycle. This way, the Young's modulus was calculated for multiple indentation depths (presented in so-called *E-d* curves, i.e., Young's modulus as a function of indentation depth). A standard deviation filter was applied to the *E-d* curves to check for groups of data points (5 consecutive data points) with similar Young's moduli. Variances below 5 % of the maximum standard deviation were accepted as constant Young's moduli (i.e., plateau region). *E-d* curves with higher variances were discarded for further analysis. In the plateau region, the Young's

modulus with the least χ squared (squared sum of residuals) was considered as the representative value. The force-distance and *E-d* curves were controlled manually if large variations or striking values of Young's moduli were observed and, if necessary, discarded. However, a sufficient number of remaining Young's moduli was monitored. For further details and the developed algorithm see [134].

MATLAB (version R2015a, The MathWorks®, Inc.) or Origin 9.1.0 (OriginLab Corporation) was used to create the graphs presented. All boxplots follow the convention described in Appendix B.2.

2.3 Investigation of Automatic Data Processing Software

The comparability of AFM-based microindentation is mainly impaired due to omitted experimental details in scientific publications and the use of fitting models with necessary assumptions that are not completely met by the materials investigated [120]. The development of new fitting models mainly concentrates on the consideration of physical phenomena such as thin film effects. Additionally, the impact of indentation force, and with this indentation depth, on the Young's modulus calculated is often not reported or ignored.

In the framework of my dissertation, my colleague Steven Huth and I have completely revised the self-made algorithm that I developed during my master thesis and we extended it by an automatic detection system so that finally a reliable algorithm could be implemented that is now capable of extracting Young's moduli from indentation data with high precision and reproducibility. For this purpose, we developed a MATLAB algorithm that iteratively fits a single force-distance curve with increasing fit ranges. For each fit range (i.e., iterative step), a single value for the Young's modulus was calculated. This permits the display of the Young's moduli as a function of indentation depth, which we call an *E-d* curve.

2.3.1 Application of a Fitting Model

The application of a mathematical fitting model is necessary to extract Young's moduli from indentation data. Plastic deformations may alter the elastic response of a material during force loading [135]. Hence, the retract curve of force-distance curves are usually used to determine the Young's modulus. However, an AFM cantilever often sticks to soft materials during retraction. This can alter the retract curve of a force-distance curve and hinders the precise determination of the contact point, which in turn is highly relevant to determine the indentation depth from the force-distance data recorded (see Equation (1.2)) [136]. To verify the usage of the extend curve, we excluded plastic deformation during the indentations. For this purpose, 100 indentation curves were recorded at one position of a thin PAM sample with a setpoint force of 300 nN. Figure 2.2 a) shows the negligible variation of Young's moduli calculated at one position. Additionally, Figure 2.2 b) presents

a representative force-distance curve, where the extend and retract curve do not differ in regions that are relevant for the fitting process. Ultimately, this justifies our technically easier approach to utilize the extend curves.

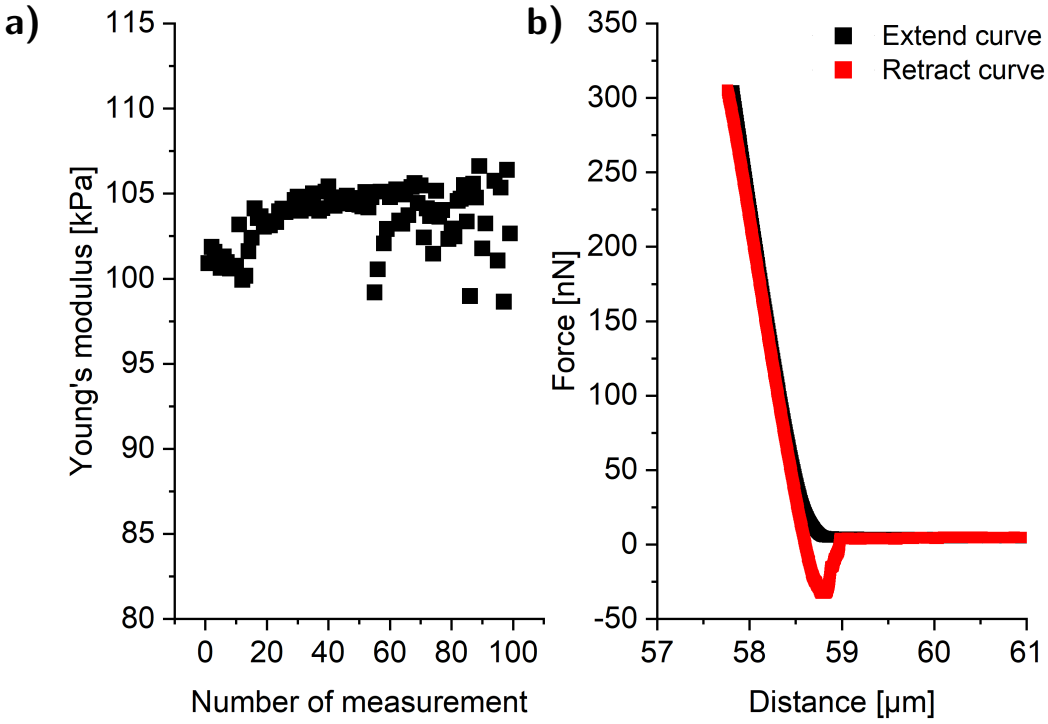

Figure 2.2: Indentations of a thin PAM sample with 300 nN at a single position elucidate the use of extend curves. a) There is no significant change of Young's moduli calculated for 100 indentations at one position of a thin PAM sample (300 nN, 1 µm/s, 21.82 µm bead). b) In regions relevant to the fitting process, the high similarity of extend and retract curve justifies the usage of the extend curve for the calculation of Young's moduli. The force-distance curve shown at 1 µm/s is representative for all indentation speeds investigated. We published this graph in Huth et al. [134].

2.3.2 Introduction of So-called *E-d* Curves

Since an underlying substrate can have negative effects and may manipulate the results [72], we integrated the impact of the indentation depth on the Young's modulus calculated. For this purpose, our algorithm iteratively fits a force-distance curve with increasing fit ranges in each iteration step and calculates a Young's modulus for each corresponding indentation depth. A larger fit range corresponds to a larger indentation force. Consequently, the iterative steps simulate multiple indentations of a material with different high indentation forces. Hence, the algorithm virtually calculates the corresponding Young's moduli for different indentation forces. We call the resulting curve an *E-d* curve (see Figure 2.3 a)).

In principle, the Young's modulus has a zero or low value for small indentation depths but increases to a plateau region with stable Young's moduli above a cer-

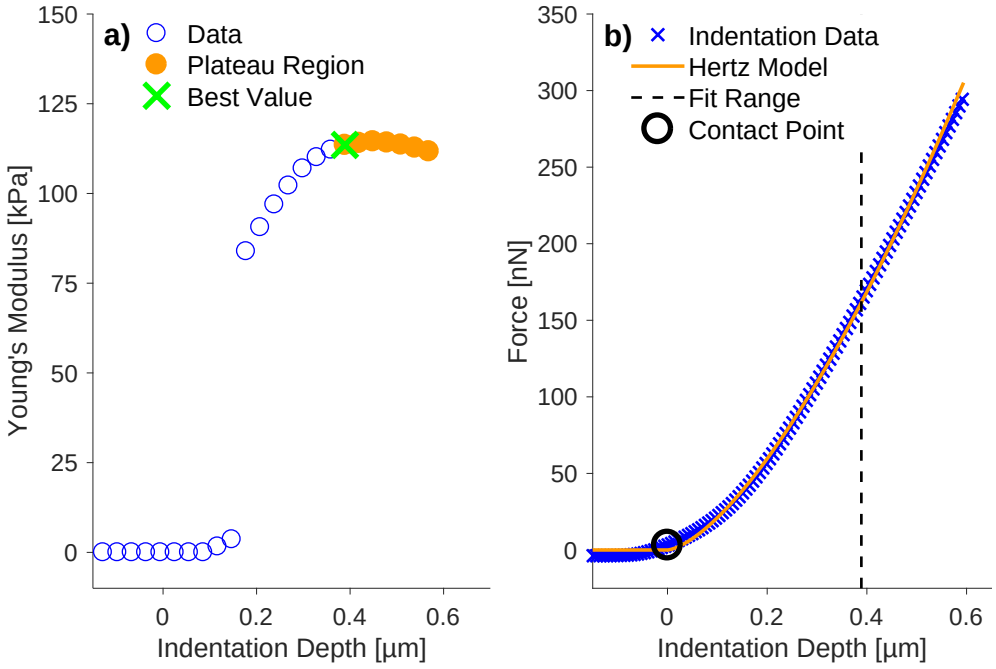

Figure 2.3: Example E-d and force-distance curve from the indentation of a thin PAM sample. a) Young's moduli as a function of indentation depth. A sufficiently high indentation force is necessary to reach a plateau region of Young's moduli calculated (i.e., independence of Young's modulus on indentation depth), which is highly relevant for the reliability and comparability of elasticity measurements. We designed our algorithm in a way that it automatically detects a plateau region of an *E-d* curve. Hence, the reliable analysis of huge amounts of data (e.g., various measurements at different positions) is guaranteed. Orange dots show the plateau region determined, whereas the green cross indicates the Young's modulus with minimized fitting error (see Section 2.3.3). b) Force-indentation depth curve with contact point marked with a black circle and fit range for the Young's modulus determined with minimized fitting error. We published this graph in Huth et al. [134].

tain indentation depth. It can be assumed that a value from this plateau region describes the elastic behavior of a material the best. Consequently, an indentation with a sufficient force to reach a sufficiently high indentation depth is crucial for the determination of Young's moduli regardless of the indentation depth.

However, several parameters might affect the indentation depth necessary to reach a plateau region. These may include material roughness, indenter roughness or material elasticity. Further research is necessary to investigate such dependencies but the examination of *E-d* curves reduces the risk of incorrect calculations of Young's moduli drastically. Indentation depths above 10 % of sample thickness are commonly considered to induce artifacts due to substrate compression or thin film effects [114], [120], [137]. *E-d* curves can easily be used to verify if indentation depths employed violate this threshold. A control of force-distance curves is not sufficient as they do not contain the necessary information about the stability of Young's moduli calculated (see Figure 2.3 b)). Furthermore, the use of enough indentation force cannot

be verified from force-distance curves. However, this is highly important to guarantee repeatable and comparable results of the Young's modulus. Hence, we propose always including the calculation of *E-d* curves. This is applicable also for other indentation techniques, such as nanoindentation.

2.3.3 Automatic Detection of Young's Moduli

To determine the Young's modulus with high precision and to reduce effects due to sample inhomogeneity, it is crucial to record a lot of indentation data. Our strategy was to include the impact of the indentation depth on Young's moduli measured but to automate the whole analysis of indentation data to allow a more comprehensive investigation of the elastic properties of soft biomaterials. For this purpose, a local standard deviation filter was used in our algorithm that checks for groups of consecutive data points with variances below a predefined threshold. The user can choose the threshold for the variance and the number of consecutive data points freely. We decided on a threshold of 5 % of the maximum standard deviation for each curve and a group of five data points in each *E-d* curve. If these requirements are not fulfilled, this force-distance curve is discarded. Although our algorithm calculates Young's moduli automatically, the computation time is of economic interest. To take this into account, the data between the contact point and the maximum indentation depth was divided into 30 equally large fit ranges. This has two main advantages: First, the computation time decreases drastically, and second, a group of five consecutive data points in the *E-d* curve represents many more data points in the corresponding force-distance curve. In addition, a color coding was introduced to the graphs to visualize the different analyzing steps. A detected plateau region is marked in orange in all *E-d* curves (see Figure 2.3 a)). Additionally, our algorithm defines a "best value" for the Young's modulus where the fitting error is minimized (indicated by the green cross in Figure 2.3 a)). The value of the fitting error is quantified by the squared sum of the fitting residuals (so-called χ). In each corresponding force-distance curve, the fit range used is marked with a dashed line and the contact point is indicated by a black circle. The Hertzian line is shown in orange overlaying the blue crosses of indentation data (see Figure 2.3 b)).

In the end, the algorithm saves text files that contain all relevant information including the thresholds and parameters applied, such as indenter radius and Poisson's ratio, to increase the transparency and reproducibility. In addition, all force-distance and *E-d* curves are saved. This gives the user the chance to check the curves manually if unusual values of Young's moduli are observed. However, the yield of usable Young's moduli (i.e., number of successfully analyzed curves) needs to be high in order to reliably display the elasticity of a material. Further information about the exact procedure of the algorithm is described in Section 2.2.4 or [134].

2.3.4 Verification of our Newly Developed Algorithm

There are many fitting models, but the Hertz model is still the most commonly used and easiest fitting model [84], [117]. The presentation of indentation data (force over

indentation depth) in a double logarithmic plot is an easy approach to extract the Young's modulus from indentation data. Applying the logarithm to the equation of the Hertz model (Equation (1.1)) it follows:

$$\log(F) = \log(\frac{4\sqrt{R}}{3}\ \frac{E}{1-\nu^2}d^{3/2}) = 3/2 \cdot \log(d) + \log(\frac{4\sqrt{R}}{3}\ \frac{E}{1-\nu^2}) \tag{2.1}$$

Where F is the indentation force, R is the radius of the indenter, E the Young's modulus, ν the Poisson's ratio and d is the indentation depth. This means that the Hertz model becomes a straight line with a slope of 1.5 in a double logarithmic plot of force versus indentation depth. Hence, the extraction of the Young's modulus would result from a simple linear fit. However, this approach is not applicable for elastic models that contain sums instead of power laws. An equation like $\log(d^{3/2} + f(d))$, where f is some function that depends on the indentation depth d, cannot be simplified. Both modern [98], [138] and classical [118], [139] theories often consist of sums. As we wanted to create an algorithm that is easily accessible by many researches, we decided to use a fitting approach that is certainly computationally more intensive but is compatible with other elastic theories.

We verified that our approach produces the same results as the accepted approach of fitting the range of force-distance curves that show a slope of 1.5 in a double logarithmic coordinate system. For this purpose, the indentation data of a thin PAM sample was plotted in a double logarithmic plot where the indentation depth was calculated by subtraction of the contact point from the indentation data. The contact point was determined from a Hertzian fit of the entire force-distance curve. An example force-indentation depth curve is shown in Figure 2.4 a). To determine the region where the Hertz model is applicable (i.e., the slope of the indentation data is 1.5), the slope of the force-indentation depth curve ($\Delta log(force)/\Delta log(indentation\ depth)$) was plotted versus the indentation depth (see Figure 2.4 b)). As PAM is not perfectly elastic, slopes between 1.25 and 1.75 (indicated by the dashed orange lines) were accepted and the respective region was also marked in orange in Figure 2.4 a). Then, the distributions of Young's moduli calculated with the double logarithmic approach and our newly developed algorithm were compared. The result is presented in Figure 2.5. A student's t-test was applied to prove that our approach has no significant difference (n.s.) to a method of standard scientific practice.

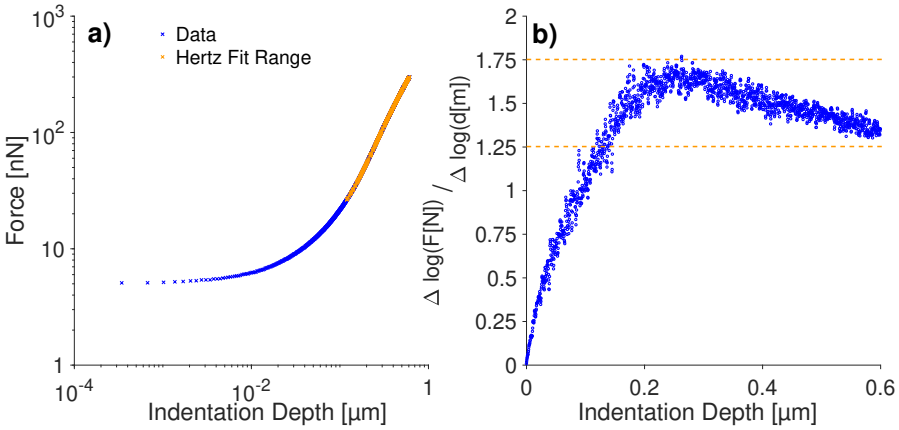

Figure 2.4: Determination of the fit range for a double-logarithmic fitting approach of the Hertz model. a) Example force-indentation depth curve shown in a double logarithmic plot. The contact point was determined from a complete fit of the force-distance curve and was subtracted from the distance values to calculate the indentation depth. A Hertz fit is only allowed in the orange region of the force-indentation depth curve. b) Plot of slope $\Delta log(force)/\Delta log(indentation\ depth)$ versus indentation depth (data from a)). Perfectly elastic materials would show a slope of 1.5 (perfect fit of Hertz model). As PAM is not perfectly elastic, slopes between 1.25 and 1.75 (indicated by the dashed orange lines) were allowed for the calculation of Young's moduli (orange region in a)). We published this graph in Huth et al. [134].

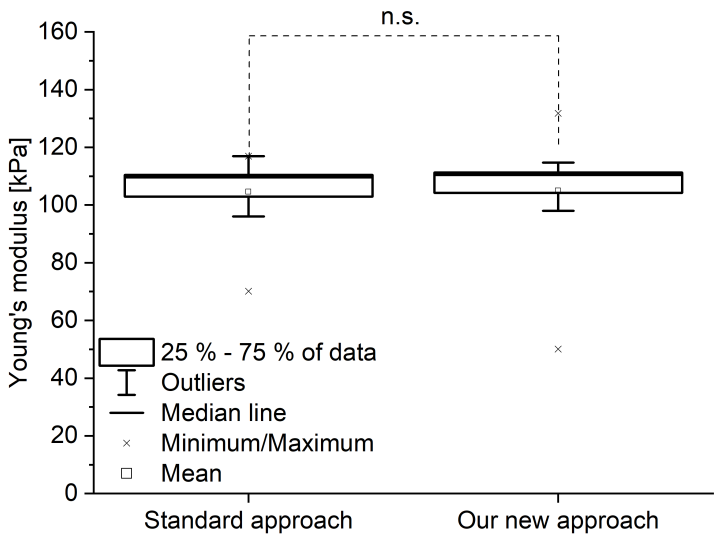

Figure 2.5: Distributions of Young's moduli calculated with our new approach and calculated by the standard double-logarithmic approach show no significant difference. A student's t-test confirms no significant (n.s.) difference between both approaches. Hence, our approach provides the same Young's moduli as a method of standard scientific practice. We published this graph in Huth et al. [134].

2.4 Systematic Measurement of the Elasticity of Polyacrylamide

To prove the applicability of our new algorithm, a systematic measurement of PAM samples at many different positions with a variation of measurement parameters such as indenter radius and indentation speed was conducted. We chose the simple Hertz model for data evaluation as proof of principle. However, our algorithm can easily be adapted to other, more sophisticated elastic models.

2.4.1 The Role of the Indenter Size

From the example *E-d* curve in Figure 2.3, it is clear that a minimum indentation depth is necessary to measure a stable Young's modulus. At the same time, the Hertz model limits the use of spherical indenters to small indentation depths [119]. A larger indenter size results in a larger possible indentation depth. This means that the indentation depth necessary serves as minimum applicable indenter radius to fulfill the requirements of the Hertz model. However, the indentation with an indenter induces a defined strain in the material. Simplified, the smaller the indenter size, the larger the strain induced, which can result in a material stiffening (increased Young's modulus) [140]. The Hertz model is only valid for small strains, which makes the verification of the effects of variable strains on the measurement of elastic properties necessary. For this purpose, a thin PAM sample was measured at 3 different sample positions (10 indentation curves each) with beads of different sizes at an indentation speed of 20 µm/s. Beads with diameters of 6.47 µm, 15.0 µm or 21.82 µm glued to AFM cantilevers were used (sizes given by the manufacturers). The setpoint force necessary to reach plateau regions in the resulting *E-d* curves was 300 nN, except for the 15 µm bead where it was 400 nN.

The resulting distributions of Young's moduli are presented in Figure 2.6 and show a clear decrease of the Young's modulus measured with increasing indenter diameter. This clearly shows that the indenter size is a crucial factor for indentation experiments and that a minimum applicable indenter size exists. It is best to calculate possible strains before indentation experiments. The strain ϵ is defined as

$$\epsilon = a/R \tag{2.2}$$

where a is the radius of the contact area between the surface and an indenter with radius R [141], [142]. For the Hertz model, the contact area is defined as $\sqrt{Rd}$ with d as indentation depth [139]. With this definition, the strain for the Hertz model can be calculated with

$$\epsilon = \sqrt{d/R}. \tag{2.3}$$

Thus, the largest bead investigated probably yields the most reliable results, as it induces the smallest strains. Smaller indenter sizes exceed the strain limit. This is

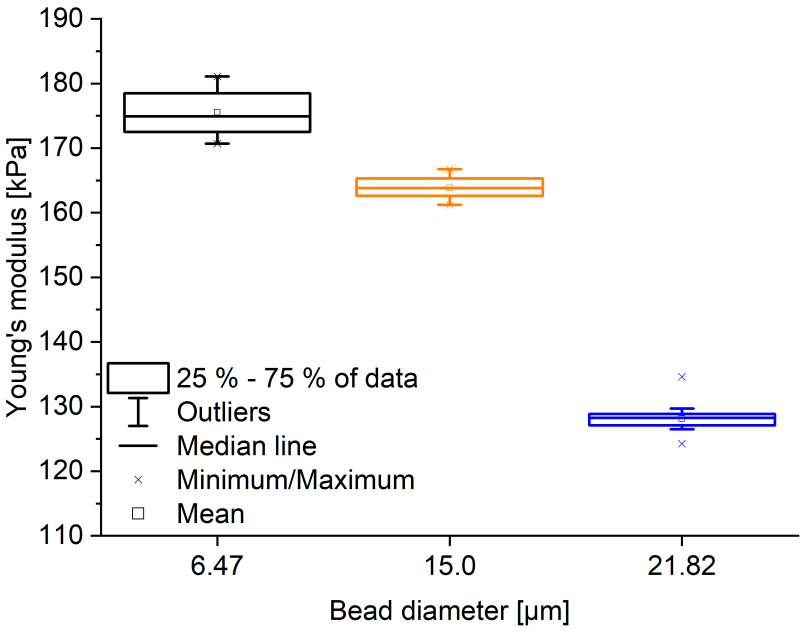

Figure 2.6: Variation of Young's moduli measured due to indentation with varying indenter sizes. A thin PAM sample was indented with beads of 6.47 µm, 15.0 µm or 21.82 µm diameter (sizes given by the manufacturers) with an indentation speed of 20 µm/s. The setpoint force was 300 nN or 400 nN. Each box shows the distribution of Young's moduli measured at 3 different sample positions (10 indentations per position). The Young's moduli measured clearly decrease for the largest indenter diameter of 21.82 µm in comparison to the smaller indenter diameters. Since smaller indenters induce larger strains in the material, this decrease most probably results from the strain induced. Additionally, the Hertz model is no longer applicable at high strains. We published this graph in Huth et al. [134].

supported by the fact that the distribution of Young's moduli for the largest indenter size is the smallest. As a consequence, we employed all further experiments with a 21.82 µm bead (size given by the manufacturer).

2.4.2 The Influence of the Sample Thickness

It is well known that the measurement of elastic properties of a soft material can be affected by a stiff underlying substrate if the soft layer is too thin or the indentation depth is too high [72], [98], [120]. Generally, the indentation depth should be limited to 10 % of the sample thickness [120], [137]. A key advantage of our *E-d* curves is that altered Young's moduli due to underlying substrates can be easily detected, for instance, if Young's moduli increase as a function of indentation depth or if a second plateau region in the *E-d* curves is visible. The latter may indicate impacts from the underlying substrate, whereas a missing detection of a plateau region in the *E-d* curve indicates insufficient high setpoint forces.

We investigated how the thickness of a sample affects the measurement of Young's

moduli independently from the underlying substrate. For this purpose, a thin, a 1 mm and a 2 mm PAM sample were indented with indentation depths much smaller than 10 % of their thickness (setpoint forces: 300 nN to 400 nN, indentation speeds: 1 µm/s or 20 µm/s). Representative *E-d* curves of these measurements are shown in Figure 2.7.

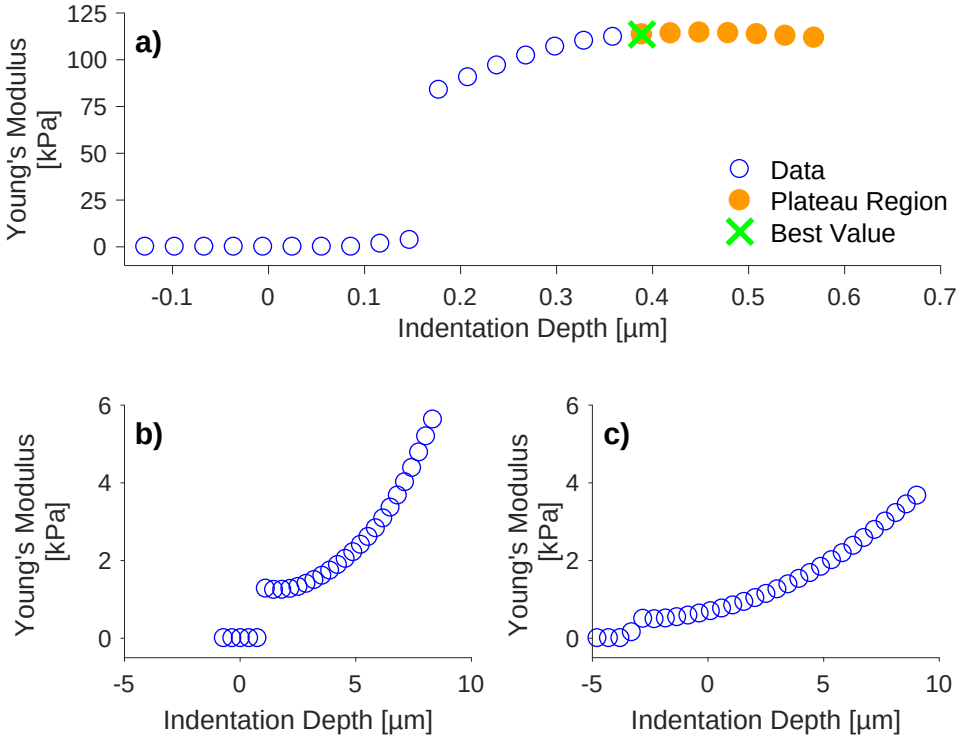

Figure 2.7: Impact of PAM thickness on the Young's moduli measured. a) A thin, b) a 1 mm and c) a 2 mm thick PAM sample were indented with a bead of 21.82 µm diameter (setpoint forces: 300 nN to 400 nN, indentation speeds: 1 µm/s or 20 µm/s). a) The representative *E-d* curve shows the expected progress with a plateau region above ca. 0.4 µm. b) and c) The representative *E-d* curves show increasing, however, low Young's moduli up to indentation depths of ca. 10 µm without detection of a plateau region. Such indentation depths clearly exceed the strain limitation of the Hertz model and suggest the existence of a maximum sample thickness for AFM-based indentations. We published this graph in Huth et al. [134].

A clear difference of the progress for the sample types is visible. The Young's moduli at very low indentation depths are almost zero and show an increase with increasing indentation depth. For the thin sample (Figure 2.7 a)), the typical plateau region is reached at ca. 0.4 µm. However for the thicker samples (Figure 2.7 b) and c)), it was not possible for our algorithm to detect a saturation of Young's moduli, even at indentation depths larger than 10 µm. Also, the values of Young's moduli are in a much lower range. Indentation depths above several µm exceed the strain limit of the Hertz model even for the largest indenter size used in this study and consequently prohibit a reliable determination of Young's moduli, even if our algorithm would have been able to extract a plateau region.

AFM cantilevers are usually installed in the system at a 10° angle, which can lead to a tangential force added to the perpendicular movement. This can result in a sliding of the cantilever over the surface or the cantilever can shear the sample if the friction between the surface and the cantilever is high enough [143], [144]. For thick samples, this effect might be enhanced due to the production in Teflon™ molds that can alter the surface structure compared to the thin sample. Consequently, our hypothesis is that the absence of the plateau region stems from a combination of sample thickness and inclination angle of the AFM cantilever. This is supported by indentation measurements of thick samples with a home-built indenting device where a horizontal indenter movement was restricted (previously described in [94]). Figure 2.8 shows an example graph of an indentation of a thick sample with the home-built indenting device where our algorithm indeed determined a plateau region in the *E-d* curve. Similar to the AFM indentation data, a zero value exists for very low indentation depths followed by an increase with increasing indentation depth up to a region of indentation depths where the Young's moduli are stable and a plateau region was determined with our algorithm. The necessary indentation depth is a little higher than for the thin sample measured with the AFM but the Young's moduli determined are in the same range. Consequently, an AFM-intrinsic limitation for the sample thickness seems to exist that could be solved with the use of tilt-corrected cantilevers. However, the abovementioned observations emphasize once more the relevance of *E-d* curves to check for Young's moduli independently of the indentation depth.

2.4.3 The Role of the Indentation Speed

Biomaterials may not always be entirely elastic but can exhibit viscoelastic properties. Hence, the timescale of characterization techniques can have an impact on the Young's moduli determined. To investigate the role of the indentation speed, thin PAM was indented with diverse indentation speeds at 25 different positions with an setpoint force of 300 nN. The results determined by our algorithm are shown in Figure 2.9. The Young's moduli measured increase with increasing indentation speeds, except for measurements recorded with 100 µm/s, which show Young's moduli similar to those at 20 µm/s.

As PAM is not entirely elastic but exhibits viscoelastic behavior [145], the dependence of Young's moduli on indentation speed was expected. A quasi-static situation (i.e., very slow indentations like 0.1 µm/s) allows the measurement of Young's moduli independent of viscoelastic behavior. Yet, the distributions of Young's moduli for indentation speeds of 0.1 µm/s and 1 µm/s are the largest of all indentation speeds. In addition to reducing viscoelastic effects through quasi-static situations, the number of force-distance curves that can be analyzed with our algorithm (i.e., the yield of usable curves) is of importance. If the number of correctly analyzed force-distance curves is too small, the indentation data is not well described by the model used and cannot accurately represent the characteristics of a sample. The yield of usable curves is 100 % for all indentation speeds, except for 0.1 µm/s and 1 µm/s, where the yield is 28.67 % and 87.20 %, respectively. This agrees with the

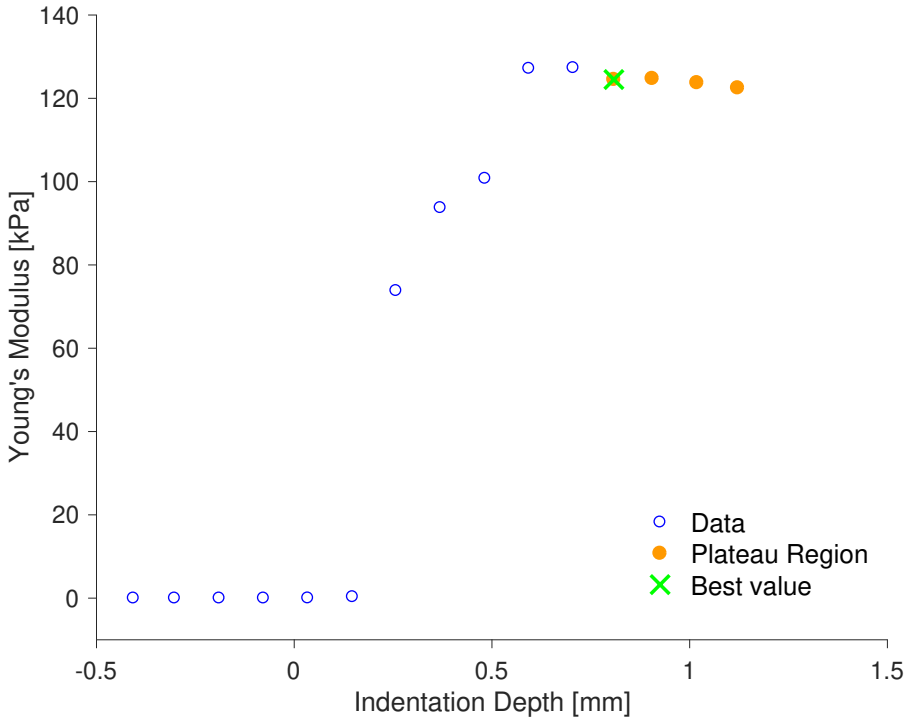

Figure 2.8: Macroscopic indentation of a thick PAM sample reveals a plateau region in the E-d curve. A home-built indenter setup (previously described in [94]) was used for the indentation of a 3 mm thick PAM sample (1 mm indentation depth, 0.5 mm/s indentation speed, spherical indenter with 6 mm diameter). Although the indentation depth of 1 mm exceeds the Hertz model limitations, the representative *E-d* curve shows a trend similar to *E-d* curves for thin samples (qualitative interpretation). Consequently, the prevention of interfering artifacts due to sample shearing could be realized by tilt-corrected AFM cantilevers. We published this graph in Huth et al. [134].

broad distribution of Young's moduli, too. A yield of less than 30 % is definitely not sufficient to guarantee reliable determinations of Young's moduli.

Another relevant aspect to consider is the time consumption for indentation experiments. Although the measurements can run mostly alone, measurements with 0.1 µm/s take more than several hours. For instance, recording 150 force-distance curves takes more than 8 h if the distance to the surface is only 10 µm, which is often not possible. Measurements of 250 force-distance curves would take more than 13 h, which makes it inefficient. Increasing the indentation speed to 1 µm/s decreases the measurement time to a tenth. The drastically increased yield of usable force-distance curves and the large reduction in measurement time makes 1 µm/s the preferred indentation speed for our PAM samples.

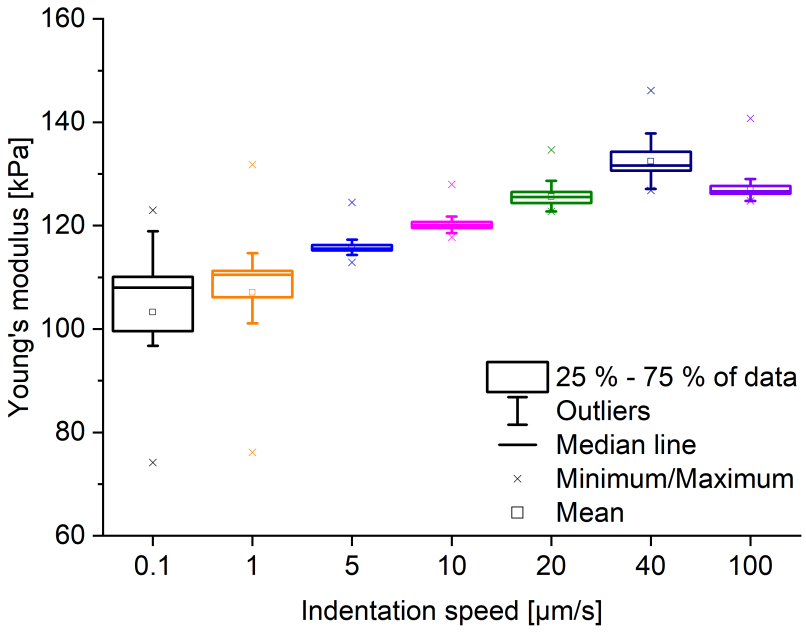

Figure 2.9: Variation of Young's moduli as a function of indentation speed for a thin PAM sample. Using 300 nN, 150 or 250 force-distance curves (10 curves at each of 15 or 25 positions) were recorded with 0.1 µm/s or 1 µm/s to 100 µm/s, respectively, on a thin PAM sample and Young's moduli were determined with our algorithm. Increasing indentation speeds result in increasing Young's moduli, except for 100 µm/s. Since PAM is not perfectly elastic, a dependence of Young's modulus on indentation speed is most likely due to the viscoelastic properties of PAM [145]. However, at longer timescales such as a quasi-static situation of 0.1 µm/s, viscoelastic properties are negligible [117]. We published this graph in Huth et al. [134].

2.4.4 The Impact of the Sample Positions and Repetitive Measurements at the Same Position

Knowledge about the influence of sample positions on elastic properties is of great importance, especially for scientific research where variations of Young's moduli can affect the outcome of experiments. For example, cells can adapt their behavior to local differences in elastic properties [11], [75] or the displacement of fluorescent beads used to measure traction forces might be affected by local inhomogeneities of Young's moduli [146]. The distributions of Young's moduli measured at 15 different positions on a PAM sample were compared with the results from multiple indentations at single positions to investigate the role of sample positions. The results are displayed in Figure 2.10. The distributions of the different positions are partially very small (e.g., position 4) but also have a variability (e.g., position 11 or position 14). Additionally, the distributions overlap or are entirely different between positions (e.g., positions 9 and 10). This shows that the variation due to positional differences and the variation on the same position are of high importance and that both factors need to be included in a reliable determination of Young's

moduli. A possible explanation for variations between different positions is related to the porous structure of PAM. The pores of PAM are in the µm regime [147], [148]. Hence, variations can result from indentations on pores and/or the PAM matrix itself. A clear consequence is the necessity to evaluate a large number of force-distance curves measured at various positions on the sample (i.e., generation of so-called elasticity maps). This ensures reliable average values of Young's moduli. However, sophisticated automatic algorithms to evaluate the data are highly relevant to make this possible. The algorithm presented demonstrates a systematic analysis that includes the relevance of indentation depth on Young's moduli and an automatic minimization of the fitting error.

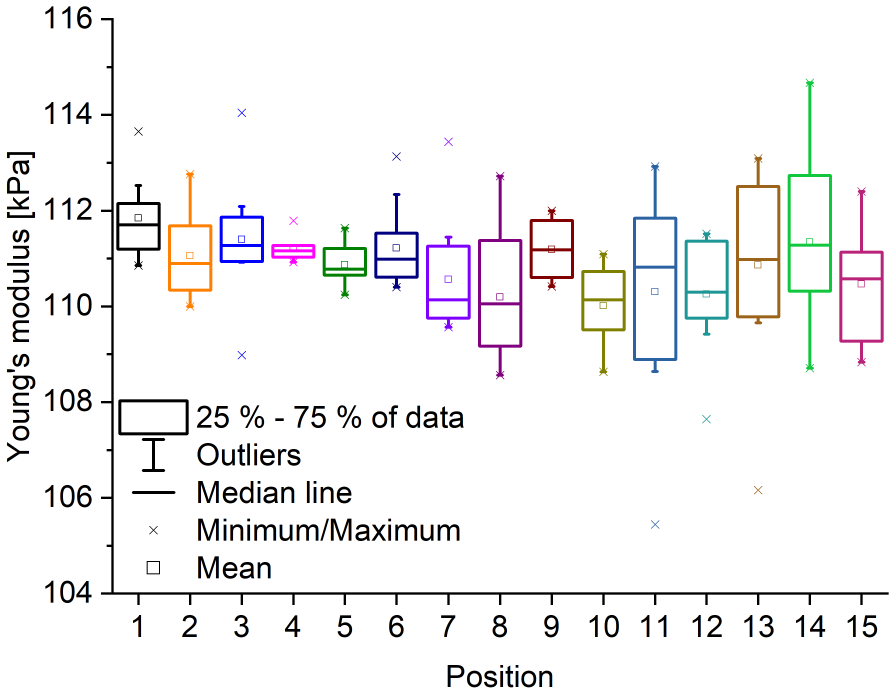

Figure 2.10: Variation of Young's moduli measured on different positions of a thin PAM sample. 15 different positions of a thin PAM sample were indented (300 nN, 1 µm/s, 21.82 µm bead diameter). The variations of Young's moduli measured at single positions and between different positions are both required to describe the elastic properties of a material reliably. We published this graph in Huth et al. [134].

2.5 Conclusion

Many cells sense and respond to the properties of their environment, which initiated many different research questions and required materials with varying material properties. In order to quantify the material stiffness, a reproducible, reliable and quantitative yet easily adaptable and feasible technique is required. Various tech-

niques have been employed to characterize elastic properties of materials. AFM-based microindentation is one of the most-used techniques but lacks consistency, for example due to omitted experimental details [87]. In addition, the dependence of Young's moduli on indentation depth is mainly ignored and/or not reported [87], [133] and reliable automatic analysis is missing.

In this chapter, I presented a new and versatile strategy for the reliable determination of Young's moduli. For this purpose, my colleague Steven Huth and I developed a MATLAB algorithm that iteratively fits the Hertz model to recorded indentation data to calculate a Young's modulus for each fit range (i.e., virtually for each indentation force). The display of an *E-d* curve shows the dependence of Young's moduli on indentation depth. This allows the detection of a value for the Young's modulus in a region where it is independent of the indentation depth. A reliable and fast analysis of huge data sets is guaranteed through a systematic and automatic detection of the plateau region and the extraction of the Young's modulus with the minimized fitting error.

I demonstrated a systematic analysis of how various experimental parameters (e.g., indenter size, indentation speed) affect the outcome of Young's moduli measurements to prove the applicability and necessity of our algorithm developed. I made clear that the specification and discussion of such values in scientific publications is essential to ensure the reproducibility and comparability of AFM-based microindentation experiments. Our proposed strategy to respect and reduce possible error sources consists of the following steps: Initially, it is required to check the computed *E-d* curves for a successful detection of a plateau region (i.e., sufficiently high setpoint forces). Especially the free choice of cantilever spring constants enables measurements of a large range of Young's moduli (hundreds of Pa up to low GPa regime). Limited by the setpoint force used and the desired spatial resolution, the largest indenter size possible should be used to minimize strains induced. As shown for PAM, the indentation speed can have a great impact on the Young's moduli measured. Hence, we propose employing a quasi-static indentation speed (e.g., 0.1 µm/s to 1 µm/s or the lowest possible), chosen so as to give a sufficient high yield of analyzable curves. Further considerations necessary are related to the storage and/or swelling time before the measurement. Studies show that the Young's modulus of a material can change over time [87]. Hence, it is essential to measure materials under stable conditions, either always after the same amount of time or after they have reached a stable state. As the experimental temperature may also have an impact on the Young's modulus calculated, Denisin et al. proposed to measure at the working temperature of the material to ensure the most reliable results [87]. I showed that our algorithm can be used to record elasticity maps and permits the determination of Young's moduli on a spatial scale similar to cell interactions. This is especially important if the materials investigated show inhomogeneity at the nano- and/or microscale. The analysis of elastic properties at many different positions of a material allows the application of statistical methods to overcome variations due to inhomogeneity.

Since our proposed method is independent of the elastic theory applied and indenting device, it has broad applicability and enables a more comprehensive study of

elastic properties of soft biomaterials. Our method may even be an important step towards high throughput measurements of hydrogels [149]. The relevance of our investigations to different application fields is confirmed through recent scientific publications that take up our work. Liamas et al., for example, investigated the effect of Young's moduli on frictional properties of protein-coated soft substrates, which is of medical relevance due to their role in causing pain in arthritis or xerostomia [150]. Although their work employed the JKR model, it emphasizes the use of *E-d* curves to extract stable Young's moduli [150]. Marin-Tapia et al. support the relevance of published experimental parameters of AFM-based microindentations during their work on corneal scaffold materials, such as collagen fibrils [151]. Finally, Zaman et al. used our method to measure Young's moduli of individual epithelial cells of a monolayer for the investigation of their apical morphology related to the formation of microvilli [152].

The abovementioned scientific publications underline once more the essential role of our method and its broad applicability. Additionally, I conducted several AFM-based microindentation experiments on mouse brain slices on a microscale for the improvement of glioblastoma treatment (collaboration with the Research Training Group GRK2154 "Materials for Brain", results not shown). My colleague Steven Huth and coworkers, on the other hand, developed a novel technique to measure traction forces simultaneously to microneedle experiments. They employed our method to accurately determine the necessary elastic properties [153]. Ultimately, my collaboration partner Joel Christian published a new strategy for the micropatterning of soft hydrogels to conduct TFM experiments on defined arrays and a so-called local UV illumination traction force microscopy (LUVI-TFM) to release cell tractions at specific regions without enzymatic treatment. I contributed to his work with the determination of the elastic properties of the substrates used [154].

Chapter 3

Manipulation Systems for Cell Manipulation and Stimulation

3.1 Introduction

Elastic properties are an important factor to investigate and manipulate cell behavior. For instance, programmed cell death (apoptosis) of fibroblast cells is favored on soft substrates [155] or a process called durotaxis allows cells, such as muscle cells and neurons, to adapt their migration according to substrate stiffness [11], [74], [75], [156]. Recently, it was proven that even cancer cells can show durotactic behavior [157].

In the first section of this chapter, I explain the role of layer thickness as an indirect factor of stiffness on fibroblast cell morphology (see Section 3.2). Previous research showed that cells can sense an underlying stiff material up to several µm, which is larger than what cells can deform in general [75], [158], [159]. However, elasticity alone is not responsible for the alteration of cell behavior. Other material properties (e.g., specific microstructures) or external factors (e.g., shear) can influence cells (e.g., cell migration or alignment) [14], [25], [156].

Deeper understanding of factors that influence cells is of medical relevance and can considerably promote prevention of, early diagnosis of and/or treatments for disease. In addition, strategies for a targeted manipulation of cells and their behavior is essential. For instance, the controlled differentiation of stem cells towards specific lineages or tissues is desirable for tissue engineering applications [84]–[86], [88], [117], or the control of cell migration towards specific regions can be utilized for pathogenic cell capture (e.g., *Acanthamoeba castellanii*) [94].

In addition to stiffness variation, there are multiple ways to manipulate cells passively. For instance, cell adhesion is strongly correlated to ligand density or spacing gradients of ligands [14], [160] but also shape and geometry of the environment (so-called curvotaxis) are relevant for cells as they affect cell spreading [161], [162]. Active manipulation of cells, on the other hand, actively applies an external stimulus to a single cell or multiple cells and a wide range of methods have been developed [156]. For instance, light-triggered activation of molecules or electrochemical stimulation can be utilized to enable a switching of ligand molecules [34], [163], [164]. Substrate

stretching devices allow cell stretching through stretching of the cell substrate at different strains and frequencies [165]–[168], which has also been combined with studies on microstructured substrates [25]. Recently, surface acoustic wave (SAW) sensors showed potential as cell manipulation technique [169], [170], whereas microfluidic devices have been employed to apply shear similar to the *in vivo* situation [171].

I focus in my thesis on external manipulation techniques to shear single cells or to apply oscillatory forces to single cells in combination with the investigation of initial adhesion via AFM single cell force spectroscopy. In Section 3.3, I explain the development of a new method to apply shear forces on single cells that allows the measurement of cell detachment directly after a shear process. In Section 3.4, I describe an unprecedented way of *in situ* cell manipulation that offers an almost unlimited range of stimulation parameters for investigating the role of oscillation frequency and amplitude on cell detachment.

3.2 Perceived Substrate Stiffness to Manipulate Cell Morphology

3.2.1 Introduction

In animals, the range of stiffness values covers multiple orders of magnitude (hundreds of Pascal for brain tissue up to the GPa regime for bone tissue) [32], [133] and the stiffness of the cell environment proved to play a crucial role in mechanotransduction pathways, which offers various ways to manipulate cell behavior [11], [84]–[86], [117], [156].

The impact of substrate stiffness on cells can be utilized for tissue engineering (i.e., design and production of artificial organs) [172] and/or disease diagnostics [10], [37], [173]. For instance, atherosclerosis can increase arterial stiffness limiting blood pressure-induced expansion and contraction of an artery [37]. Singh et al. analyzed numerous studies and showed that the degree of liver stiffness is linked to several diseases (e.g., cirrhosis, hepatocellular carcinoma) and death of patients with chronic liver diseases [173]. Moreover, Harkness et al. showed that joint stiffness varies during the day affecting the disease activity in rheumatoid arthritis [174]. Hosseini and coworkers showed that cancer cells can adapt their stiffness according to their cell cycle [175]. During mitosis, the cells showed increased stiffness compared to the interphase [175]. Furthermore, the stiffness is highly relevant for the design of implant materials. For applications in bone tissue, for example, very stiff materials up to the GPa regime may be required to provide sufficient support (e.g., hip replacement) [176], [177]. However, high stiffness can also produce a large mismatch of elastic properties between implant material and tissue that can affect the implant acceptance [178], [179]. For instance, deep brain stimulation devices implanted in the brain for treatment of Parkinson's disease are usually made of electrodes in the GPa regime, whereas brain tissue is in a low kPa regime [180]. Hence, scar formations due to the large stiffness mismatch can impair brain stimulation and/or signal

transduction of healthy brain cells [89], [179]–[181]. Also, cartilage wear and bone fracture can result from a stiffness mismatch of cartilage and stiff implant materials after joint replacements of hip or knee [178].

Hence, the development of implant materials towards implant designs and/or materials that mimic the surrounding tissue are necessary [180]. Since new designs and developments take time and are expensive, another approach that allows the use of established materials is the coating of a stiff implant material with a soft layer [178], [180], [182]. Thus, the material appears softer if the layer thickness is sufficiently large. Elastic measurements of thin films reveal that underlying stiff substrates can have an influencing factor [98], [120]. It is reasonable that cells with the ability to respond to stiffness variations can sense stiff underlying materials up to a certain layer thickness (so-called thickness sensing threshold) [133]. Hence, to establish soft coatings for stiff implant materials, it is essential to investigate the role of layer thickness for cell behavior.

The general concept of research projects that explore thickness sensing thresholds involves the seeding of cells on a soft material (often PAM [21], [133] or collagen [75], [93]) fixed to a stiff underlying substrate (usually glass) and to investigate the cell behavior by means of different cell parameters (mostly cell spreading area) [75], [93], [133]. The stiffness of the materials used is generally in the lower kPa range (1-35 kPa) [75], [93], [133].

Previous research has shown the existence of thickness sensing thresholds for various cell types. For instance, Buxboim et al. suggested a thickness sensing threshold of ca. 3.4 µm for mesenchymal stem cells on 1 kPa PAM [133]. The works of Engler and coworkers show no significant difference between smooth muscle cells on a 5 µm and a 70 µm thick layer [75], [88] and concluded that smooth muscle cells cannot sense deeper than 5 µm [75]. Maloney et al., on the other hand, determined a much larger thickness sensing threshold of ca. 60 µm for NIH-3T3 fibroblast cells on 5.6 kPa PAM [21]. In addition, Shing et al. propose a relevance of the substrate material for the value of the thickness sensing threshold determined [93]. In contrast to Buxboim et al., Shing et al. suggest a thickness sensing threshold for mesenchymal stem cells above 130 µm on a 2 kPa stiff collagen substrate and justified these findings with strain stiffening effects of collagen [93].

Knowledge about thickness sensing thresholds will allow the reduction of implant coatings to a minimum thickness necessary for prohibiting negative impacts of stiff materials. Hence, the volume of required material decreases, which is of economical interest (e.g., reduced costs for material and production time) and is desirable to reduce the risk of side effects and/or complications, such as inflammations.

Here, I present an experimental setup to investigate the influence of layer thickness on cell morphology. For this purpose, fibroblast cells were seeded on functionalized PAM with different thicknesses fixed to glass. After one day, the cell morphology was investigated with phase contrast microscopy. The output of this project resulted from the collaboration with Galen Ream, a student who worked under my supervision and guidance. I show that the cell spreading area and the cell circularity (cell shape parameter) are strongly correlated to the layer thickness of PAM. Further-

more, I suggest that the thickness sensing threshold determined is independent of the layer stiffness. Initial experiments with fibrosarcoma cells (a malignant tumor of the connective tissue) show no clear correlation between cell parameters and layer thickness. This indicates that specific cell types may not have a defined thickness sensing threshold.

3.2.2 Experimental Design

The experimental design to investigate the impact of layer thickness on cell behavior is shown in Figure 3.1. Varying volumes of PAM solution were polymerized on glass to realize hydrogel layers of different thicknesses on a stiff underlying substrate. A biofunctionalization was used to promote cell adhesion. Cells were seeded on the samples and investigated with phase contrast microscopy to characterize their cell spreading area and cell circularity.

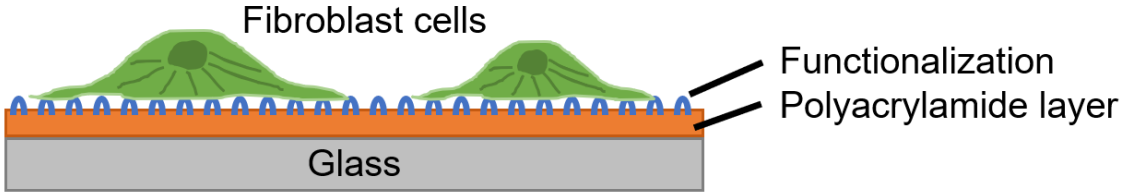

Figure 3.1: Experimental design to investigate the impact of layer thickness. Variable amounts of PAM solution were polymerized on glass to produce layers of variable thicknesses. Cells were seeded on the functionalized PAM and observed with phase contrast microscopy.

Production of Polyacrylamide

The production of PAM samples is similar to the procedure described in Section 2.2.2. Different bis-acrylamide concentrations were used to vary the mechanical properties of the samples. At first, the constituents shown in Table 3.1 were mixed and degassed. Then, 0.75 µl TEMED (Sigma-Aldrich) and 2.50 µl APS (Bio-Rad Laboratories, Inc.) were added directly before deposition. Samples with 5 % bis-acrylamide are referred to as "soft" (ca. 23 kPa), whereas 18 % bis-acrylamide samples are called "stiff" (ca. 175 kPa). The mechanical characterization was conducted with a home-built indenter system (see Appendix C).

Thickness variation was realized with custom-made Teflon™ molds (heights of 100 µm, 400 µm and 4 mm, diameter of 10 mm) or deposition between two glass slides. A pretreatment of the glass slides with methacrylate was necessary to achieve tight bonding between the PAM and the glass. The treatment was the same as described in Section 2.2.2.
To produce thin samples, 5.00 µl of PAM solution were deposited on a pretreated glass slide and covered with an untreated, round glass slide (diameter of 12 µm). For thicker samples, 80 % of the total volume of a Teflon™ mold were filled with the PAM solution and covered with a pretreated glass slide. After 60 min of polymerization, the samples were sterilized 15 min in 70 % ethanol. Then, they were

Table 3.1: Constituents used

Chemicals **Crosslinker concentration**	5 vol%	18 vol%
a-NHS[1] (0.01 mg/µl, Sigma-Aldrich)	300.00	255.00
Acrylamide (40 %, Bio-Rad Laboratories, Inc.)	150.00	150.00
Bis-acrylamide (2 %, Bio-Rad Laboratories, Inc.)	25.00	90.00
HEPES[2] (100 mM, pH 5.5, Sigma-Aldrich)	5.00	10.00
NaOH[3] (2.5 M, Sigma-Aldrich)	5.00	3.00
Bidest. water	11.75	-

[1] Acrylic acid *N*-hydroxysuccimide ester
[2] 2-[4-(2-Hydroxyethyl)piperazin-1-yl]ethane-1-sulfonic acid
[3] Sodium hydroxide

washed three times with phosphate buffer saline (PBS) and swollen in bidest. water for 2 days. All samples were produced in triplicates (i.e., three samples for each volume used).

Biofunctionalization of Polyacrylamide

For experiments with fibroblast cells, the samples were incubated overnight in 100 µl fibronectin (10 µg/ml in 1x PBS, Advanced BioMatrix, Inc.). Prior to cell seeding, each sample was rinsed with PBS.

For experiments with fibrosarcoma cells, the samples were incubated in 70 % ethanol for 15 min and then rinsed with sterile HEPES (Sigma-Aldrich). Then, the samples were incubated overnight in 400 µl of sterile collagen solution (0.5 mg/ml in 0.02 M acetic acid, Sigma-Aldrich). Prior to cell seeding, each sample was rinsed with PBS.

Cell Culture

Rat embryonic fibroblast (REF 52-wt) and fibrosarcoma (HT1080) cells were cultured following the standard procedure described in Appendix B.3. The medium used for fibroblast cells was Dulbecco's Modified Eagle's Medium (DMEM, Biochrom) supplemented with 10 % fetal bovine serum (FBS, Biochrom), 1 % penicillin streptomycin (Pen/Strep, Biochrom) and 1 % GlutaMAX-I (Biochrom). The medium used for fibrosarcoma cells was DMEM supplemented with 10 % FBS and 1 % Pen/Strep. 0.05 % Trypsin/0.02 % EDTA solution (Sigma-Aldrich) was used for cell detachment. 30,000 cells were seeded on each sample and incubated overnight at 37°C and 5 % CO_2.

Imaging with Phase Contrast Microscopy

The next day, the samples were imaged with phase contrast microscopy (IX81, Olympus, software: cellSens Dimension, version 1.12) with 4x and 10x objectives. 10-15

randomly distributed images were recorded for each magnification. Afterwards, the samples were washed with PBS and the imaging process was repeated.

Determination of Sample Thickness

The thickness of each sample was determined from the z-levels recorded at the focus plane of the top glass surface or the PAM surface. For this purpose, the imaging process was started at the interface of the PAM border and the glass surface, where the glass surface was kept as base level. Then, the z-level was recorded throughout the imaging process. The thickness was calculated from the difference between glass z-level and PAM z-level.

"Thin" samples refer to samples with a thickness below 70 µm, "intermediate thick" samples cover a thickness range between 70-200 µm and "thick" samples are thicker than 200 µm.

Determination of Cell Parameters

A semi-automatic analysis of each image was conducted with ImageJ (version 152a). For this purpose, contaminants and severe clustering were manually excluded from the analysis. Then, the background noise was reduced and the image was converted to a 8-bit greyscale. Manual thresholding was used to produce a binary image, where high intensities were converted to black and low intensities to white pixels. Afterwards, the program automatically determined the number of pixels for each particle cluster above a pixel width of 80 pixels or 120 pixels for images recorded with 4x magnification or 10x magnification, respectively. Each image analyzed was compared to its original to guarantee accurate cell representation. At last, the cell spreading area A was calculated from the number of pixels and the cell circularity C from Equation (3.1).

$$C = 4\pi A/p^2 \tag{3.1}$$

with p as the perimeter of the cell [97]. A cell circularity of 1 defines a perfectly round cell, whereas a value of C = 0 represents an elongated cell.

The graphs presented were created with Origin 9.1G (OriginLab Corporation) and show the mean values of cell spreading areas or cell circularities with standard deviations as error bars.

3.2.3 Assessment of the Experimental Design

In mechanotransduction studies, PAM fixed to glass is a standard system [21]. Since the production from a precursor solution permits the adaptation of the volume used to generate variable thickness, PAM is the perfect candidate for investigating thickness effects. In addition, the use of different ratios of the crosslinker bis-acrylamide allows easy production of variable elasticities without alterations of the chemical

properties [43], [83], [96]. PAM can be sterilized with ethanol and swells in water or physiological relevant media [95]. As cell attachment to bare PAM is limited, a defined cell attachment is realized through a biofunctionalization with fibronectin. To avoid any impacts due to ligand density fluctuations, a constant concentration of adhesion ligands (here: fibronectin at 10 µg/ml in 1x PBS) was realized throughout the experiments.

A secure fixation of the material used (here: PAM) to the underlying stiff substrate is crucial to ensure that effects related to cellular traction forces (e.g., applied mechanical stresses) are limited to the cell-material interface [133]. Otherwise, a deformation or rupture at the material-substrate interface could occur due to cellular traction forces [21], [75]. Furthermore, external loads in cell culture (e.g., media exchanges) or fluid shear stresses *in vivo* can partly detach a material from the stiff underlying substrate [133]. Thin samples are more prone to such influences than thick samples [133]. If a glass slide is treated with a mixture of methacrylate, ethanol and acetic acid (so-called silanization), PAM can easily be attached to the treated glass with high stability.

To make thin samples, the PAM solution was deposited on a silanized glass slide and covered with an untreated glass slide. The respective thickness of the samples was defined by the volume used. However, the sizes of available pipettes limit the possible minimum volume to around 1 µl. Additionally, it was not possible to produce smooth and intact PAM with very small volumes of PAM solutions. The samples were partially ruptured (see Figure 3.2) or the glass slide was not completely covered with solution. In many cases, both types of faulty production occurred together. The minimum successful layer thickness was ca. 20 µm.

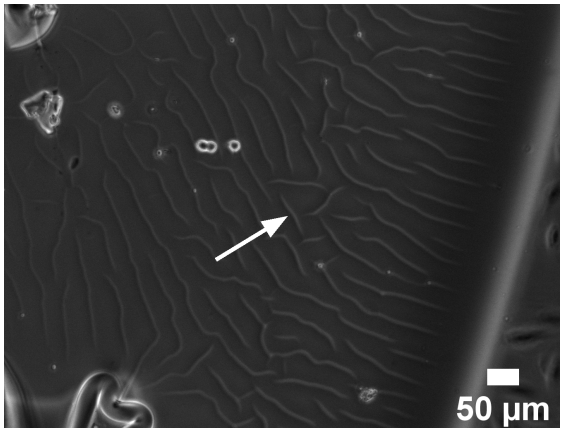

Figure 3.2: Phase contrast microscopy image of thin, partially ruptured PAM. The minimum successful layer thickness was ca. 20 µm since the production of smooth and intact PAM with small volumes of PAM solution was not possible. The sandwiching method produced partial ruptures of the PAM (see white arrow). Scale bar 50 µm.

Another chance to produce very thin PAM samples is the use of small beads within the PAM solution that serve as spacers between both glass slides [75], [133]. However, such beads are usually made out of glass and remain in the samples throughout the experiments. Cells are able to deform substrates up to 0.5 µm in the axial di-

rection [159] and around 2 µm in the lateral direction [75], [158]. Hence, a stiff bead within the material can certainly influence the experiment. For samples with lateral sizes of centimeters, it may be possible to arrange the glass beads only at the edges.

Parameters that describe cell-material interactions include cytoskeleton organization, cell morphology, adhesion forces or cell migration [4], [60], [133], [183]. The labelling of cytoskeletal filaments such as actin may require advanced microscopy techniques, often transfection or fixated, dead cells and a quantification of observations may be difficult. The characterization of cell adhesion forces, on the other hand, is usually limited to short time adhesion [109]. Cell morphology, such as cell spreading area, can easily be determined from microscopy images, however, it must be ensured that loose cell-material attachments are excluded.

3.2.4 Cells Sense a Stiff Underlying Substrate

Fibroblast cells were seeded on differently thick PAM samples that were tightly bound to glass. A sufficient fibronectin functionalization was used to guarantee a high density of adhesion sites on the surface. The cells were observed with phase contrast microscopy after one day of incubation in culture medium. The convention for the different sample types is as follows: Samples produced from a solution with 5 % bis-acrylamide are named "soft", whereas samples with 18 % bis-acrylamide are named "stiff". "Thin" samples have a thickness below 70 µm, "intermediate thick" samples cover a thickness range of 70-200 µm and "thick" samples are thicker than 200 µm.

Figure 3.3 shows representative phase contrast images of fibroblast cells on thin (top row) and thick (bottom row) PAM for 5 % bis-acrylamide (soft, left column) and 18 % bis-acrylamide (stiff, right column). A clear difference of cell shapes is visible between thin and thick PAM. While cells on thin PAM occupied larger sample areas and were more elongated, cells on thick PAM were mainly round and some clustered together. To ensure that round cells were indeed adherent to the PAM, a washing procedure similar to a wash assay was conducted [8]. A comparison between both bis-acrylamide concentrations showed no clear difference in cell shape in the microscopy images. A home-built indenting device (previously described in [94]) was used to measure the elastic properties of bulk PAM samples and our MATLAB algorithm developed (see Chapter 2, [134]) was used to determine the Young's moduli. The results are shown in Appendix C. Soft samples had a Young's modulus of ca. 23 kPa and stiff samples of ca. 176 kPa. These values cover a reasonable range of different tissues such as spleen, thyroid, muscle, skin, bladder, cornea [32], [184].

To quantitatively explain differences between the various thicknesses and the two bis-acrylamide concentrations, the cell spreading area and the cell circularity (see Equation (3.1)) were determined. For this purpose, a semi-automatic image analysis was used with ImageJ (see further details in Section 3.2.2). A mean value of all cells for each image analyzed was extracted. The results are shown in Figure 3.4, where each symbol represents the mean value of at least five microscopy images and the error bars show the standard deviations. Black squares show results from soft

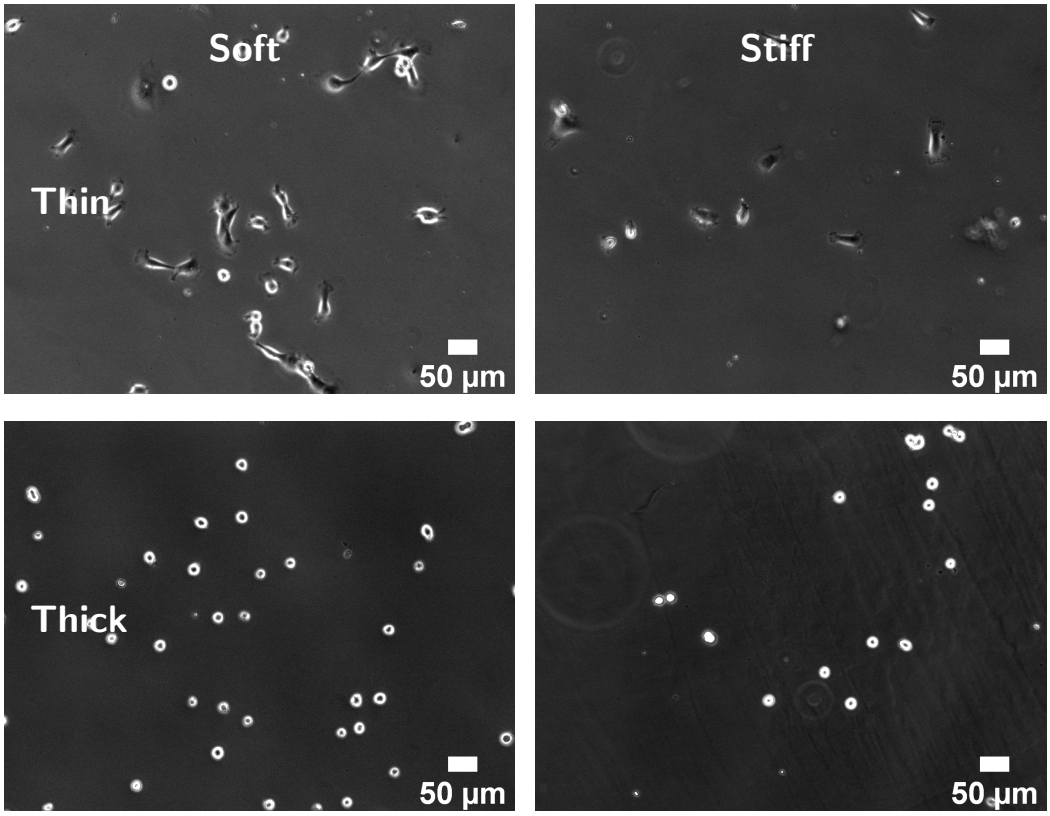

Figure 3.3: Representative phase contrast images of fibroblast cells on thin (top) and thick (bottom) hydrogels for both stiffness values. Cells on thin PAM spread more and were more elongated than cells on thick PAM. An increased thickness resulted in round cells with more clustering. No clear difference is visible between fibroblast cells on soft (left) and stiff (right column) PAM. Scale bar 50 µm.

samples and orange diamonds refer to results from stiff samples.

Figure 3.4 a) shows the cell spreading area as a function of the layer thickness for both stiffness values. For low thickness values, mean cell spreading areas are between ca. 650-1100 µm^2. However, at ca. 70 µm layer thickness, mean cell spreading areas drop to values around 400 µm^2 for larger thickness values. This shows that the fibroblast cells change their spreading area according to the layer thickness. As fibroblast cells show increased spreading on stiffer substrates, this suggests that they sense and respond to the stiff underlying glass. The progress of the cell circularity is shown in Figure 3.4 b). For easier comprehension, the y-axis (i.e., values for cell circularity) is inverted. For thin samples, the value is in a low regime (0.2 to 0.4), whereas thicker samples resulted in mean cell circularity values above 0.5. The transition point is at ca. 70 µm as well. The cell circularity reflects the shape of a cell (see Equation (3.1)), where small values refer to elongated cells and a value of 1 defines a perfectly round cell. Hence, cells seeded on thin PAM samples show an elongated cell shape as shown in Figure 3.3 that represents a good attachment to the substrate. On thicker samples, on the other hand, the cells show only a small, round shape, which is associated with a weak cell-PAM connection.

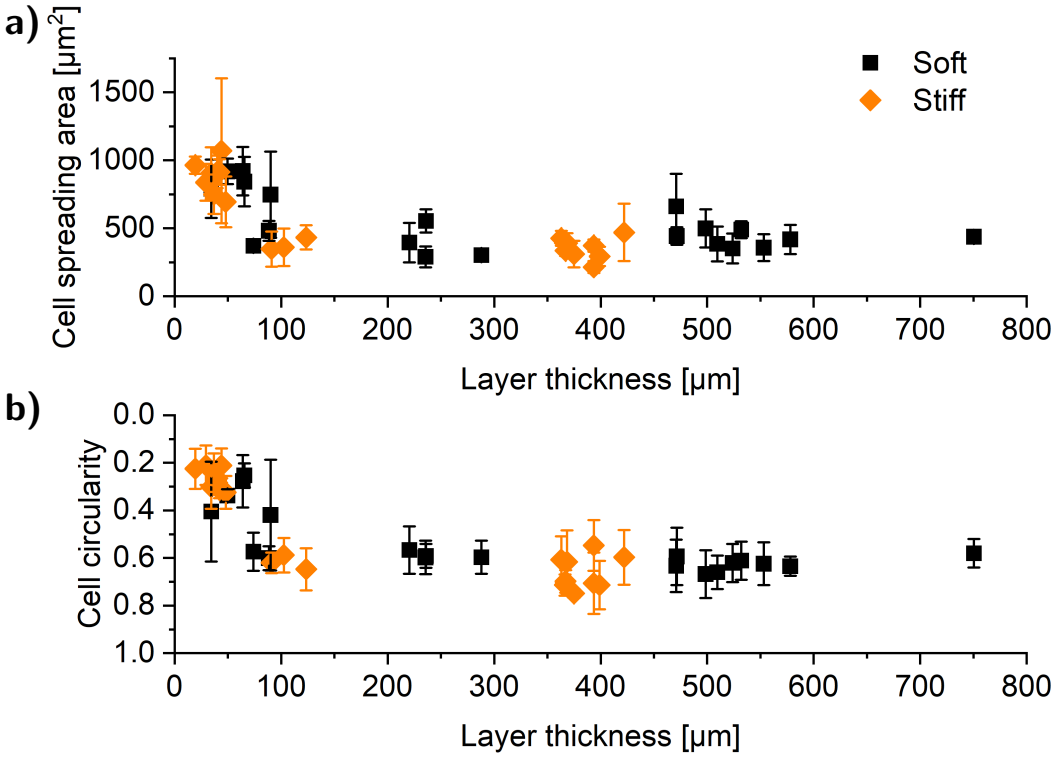

Figure 3.4: Cell parameters of fibroblast cells determined as a function of layer thickness for soft and stiff PAM. a) Fibroblast cells have larger cell spreading areas on thinner PAM samples. Larger layer thicknesses led to decreased cell spreading areas. The transition point is at a layer thickness of ca. 70 µm, where the cell spreading area saturates at around 400 µm^2. b) Fibroblast cells on thin PAM show cell circularity values between 0.2-04. With increasing layer thickness, the cell circularity increases to a plateau region of around 0.6 above a layer thickness of ca. 70 µm. The dependence of cell parameters on layer thickness suggests a so-called thickness sensing threshold of ca. 70 µm. Fibroblast cells sense the stiff underlying glass up to this thickness threshold and adapt their cell spreading behavior accordingly.

These observations agree well with the work of Maloney et al.. They observed that NIH-3T3 fibroblast cells show changed behavior at a thickness above 60 µm on materials with 5.6 kPa [21]. Combining their work and the results shown here, a large stiffness range (5.6 kPa up to 176 kPa) is covered that all show similar results. This suggests that fibroblast cells show a so-called thickness sensing threshold independent of the stiffness of the material, although previous works showed that fibroblast cells are able to detect and respond to material stiffness [7], [156]. For instance, NIH-3T3 fibroblast cells migrate towards stiffer regions of a material or change their migration direction when approaching softer regions [38], [156]. Additionally, it was observed that some cells exert larger traction forces and increase their cell spreading area on stiffer materials [156].

The tight fixation of PAM to the stiff glass limits the material deformation through traction forces and reduces the flexibility of the material. Hence, the material appears stiffer and cells adapt their behavior as if the material were stiffer (e.g., increased spreading) [21], [75]. Furthermore, the degree of material flexibility affects

adhesion structures and it was shown that cells show reduced spreading on more flexible substrates [43]. In addition, an underlying stiff substrate can lead to an increase of the effective stiffness of the material [21], [185], which supports the idea that the material appears stiffer for the cells. This suggests that some cells actively adapt and regulate their contractility according to environmental conditions [156]. For instance, cells can deform substrates up to a low micrometer range [75], [158], [159]. However, the previously reported behavior and the thickness sensing thresholds of fibroblast cells observed here exceed several micrometer. Hence, it can be assumed that cells detect, amplify and convert such input signals into intracellular responses [27], [156].

3.2.5 Sensing Threshold is Linked to Cell Type

Research shows that the thickness sensing threshold depends on the cell type. So far, it is unknown if it is to some extent related to the degree of mechanosensitivity of cells or to their respective environment (e.g., cell or tissue stiffness, structure). For instance, fibroblast cells show a high degree of mechanosensitivity and high affinity to stiff environments (e.g., migration to stiffer regions) [38], [156]. This could explain their large thickness sensing threshold.

A remaining question is how cells of softer tissues react to the experimental design presented. For instance, cell morphology of microglia and astrocytes can correlate with substrate stiffness [89] and a foreign body response in brain tissue can impair implant functionality [181]. Hence, the expected response to layers of varying thickness on a stiff underlying substrate would be a reduction in spreading on thin layers and increasing spreading with increasing layer thickness. To investigate if this expectation is correct, fibrosarcoma cells were used in the same experimental design and their reactions to different layer thicknesses were tested as a proof of principle. Fibrosarcoma cells are highly motile cancer cells of the connective tissue [92]. Fibrosarcoma cells are formed from mesenchymal fibroblast cells, which make them a perfect candidate for comparison.

The fibrosarcoma cells (HT1080, Lammerding Lab, Cornell University, USA, [186]) were seeded on collagen coated PAM layers of variable thickness fixed to glass. After one day of incubation, the samples were washed and observed with phase contrast microscopy. Figure 3.5 shows mean values and standard deviations of a) the cell spreading area and b) the cell circularity as a function of layer thickness for soft (black squares) and stiff (orange diamonds) PAM samples. The cell parameters investigated (i.e., cell spreading area and cell circularity) show no clear dependence on the layer thickness. A comparison with the results from my studies on fibroblast cells shows that the cell spreading area of the fibrosarcoma cells is in a similar range as cell spreading areas of fibroblast cells on thin PAM samples, whereas the cell circularity is rather in the range of cell circularities of fibroblast cells determined on thick PAM samples. It was shown that invasive cancer cells can penetrate into soft materials, such as PAM [187]. In addition, cancer cells can adapt to their environment [17], [36], [175], [188]. Here, this could explain their limited preference for specific thickness values.

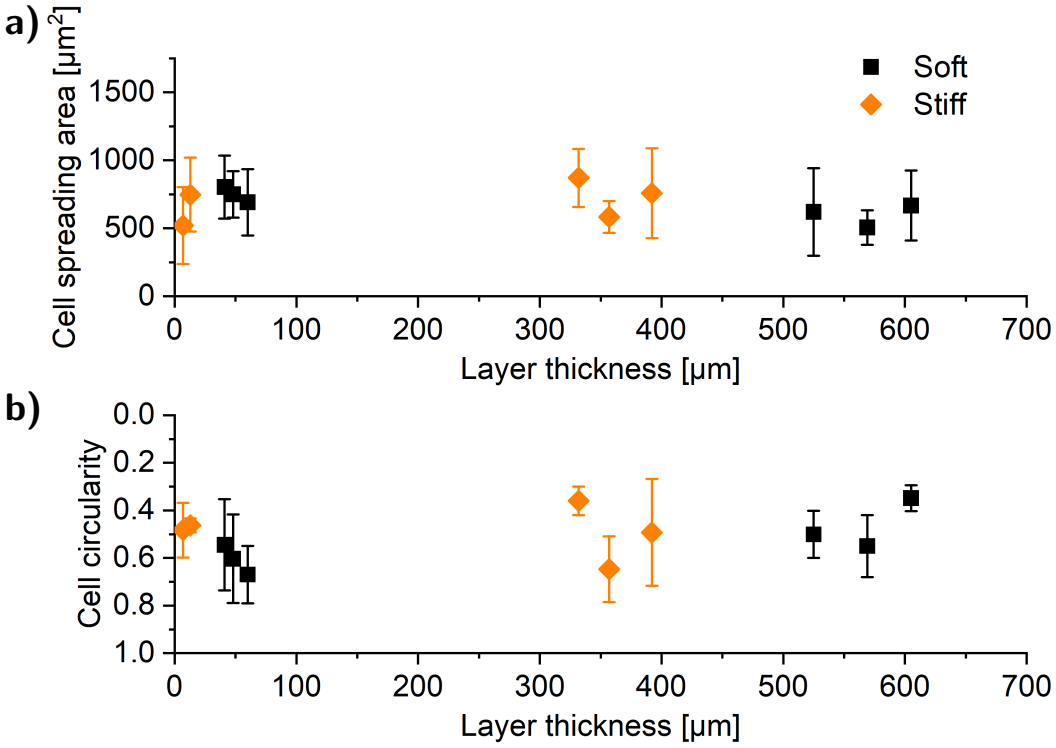

Figure 3.5: Cell parameters of fibrosarcoma cells determined as a function of layer thickness for soft and stiff PAM. a) Cell spreading areas of fibrosarcoma cells are in a similar range as cell spreading areas of fibroblast cells on thin PAM samples. b) Values for cell circularity of fibrosarcoma cells are rather similar to cell circularities of fibroblast cells on thicker PAM samples. However, no clear correlation between cell spreading area or cell circularity and layer thickness is visible.

3.2.6 Conclusion

The ability of cells to sense and respond to substrate stiffness proved to be an important factor in mechanotransduction studies and for the development of material designs for medical applications [11], [84]–[86], [117], [156]. The existence of a so-called thickness sensing threshold (i.e., depth of cell sensing) emphasizes the need for a comprehensive study of cell behavior.

Here, I presented a system to measure the impact of layer thickness on cell morphology and showed that the layer thickness has a significant influence on fibroblast cells. Until now, most researchers focused on the spreading area as representative cell parameter [75], [93], [133] but I showed that the cell circularity is equally relevant. I supported the findings of Maloney et al. that fibroblast cells might have the largest thickness sensing threshold of all cells investigated so far [21]. In addition, I showed that the thickness sensing threshold of fibroblast cells is not affected by the stiffness of the layer material used (PAM with stiffness range of ca. 5.6-176 kPa). Previous works usually published the results of only one stiffness [75], [133]. Hence, I can only speculate if a stiffness independent thickness sensing threshold exists for other cell types as well. Further research should focus on correlating actin fibers and/or trac-

tion forces to the thickness sensing threshold to improve the overall understanding of mechanotransduction.

Initial investigations of fibrosarcoma cells (a malignant cell line derived from mesenchymal fibroblast cells) showed no clear correlation between cell spreading and layer thickness. Although the number of samples measured was limited, these findings suggest either that their thickness sensing threshold is larger than the thicknesses investigated (above 600 µm) or, which is more likely, that these cells have no clear preference for a certain layer thickness, thus indirectly the substrate stiffness. Further research on materials without pores (e.g., PDMS) may show if fibrosarcoma cells indeed have a thickness sensing threshold.

3.3 AFM-based Shear System for Single Cell Manipulation

3.3.1 Introduction

Several factors, such as material stiffness or topographic properties, can influence cell behavior [9], [11], [32]. For instance, some cells align with substrate structures, such as channels, in a process called contact guidance [9] or endothelial cells adapt to the curvature of vessel walls [189]. Furthermore, cells are subjected to a variety of active external forces (e.g., pushing, pulling). Since blood and endothelial cells are constantly exposed to shear in blood vessels [167], [190], it is of medical interest to maintain normal shear conditions [190], [191] and/or to understand possible alterations of shear conditions. For instance, vascular functionality depends on normal shear flows, where reduced shear flow can impair vascular wall functions (e.g., vasodilatation, endothelial cell repair), which can in turn increase the risk for atherosclerosis (formation of plaques that constrict the vessel) [37], [190], [192], [193]. A blood vessel may dilate as a result of atherosclerosis and an aneurysm that increases blood disturbances or may rupture can form if the dilatation is too large [194]. Especially near vessel junctions, impaired shear flow can promote blockage of the vessel (so-called thrombosis) [191], [193]. Also, disturbed shear flow can affect vascular inflammation through altered gene expression of endothelial cells towards proinflammatory genes [190], [191].

To prevent, medicate and cure such diseases, it is essential to understand the role of shear on cells and their adhesion. Although integrins, protein-tyrosine kinases and the structural integrity of actin are believed to have essential roles in shear-induced cell reactions [20], [190], it is still unclear how exactly cells sense shear and what signaling pathways or genes are involved [191], [195]. Yet, vascular smooth muscle cells regulate their proliferation and migration to shear conditions and orient perpendicular to the shear direction [191], whereas endothelial cells align with shear directions [191], [192], [195]. Also, leukocytes, such as macrophages or dendritic cells, align with the shear direction [196]. Noria et al. showed a shear-induced disassembly and subsequent reassembly of adherens junctions with remodeled F-actin

distribution [24]. For instance, actin reorganization was observed for endothelial cells [192] and amoeba *Dictyostelium discoideum* [36]. Hence, external shear can initiate a dynamic redistribution of forces and successive cell-cell or cell-substrate ruptures [153] and/or affect immediate gene expression [190]. Some cancer cells (e.g., epithelial bladder type) seem to increase their spreading area under shear conditions [36]. A dependence of critical shear stress on cell confinement was shown by Couzon et al., where increased confinement lowered the shear stress necessary for cell detachment [36]. This dependence vanished above a certain channel height (i.e., disappearing role of confinement) [36].

Riveline et al. proposed that integrins as part of focal complexes can act as individual mechanosensors [29] and might be responsible for the translation of shear conditions into biochemical signals [190]. Furthermore, the initiation of cell adhesion can be controlled through shear flow since it mediates the activation of β-integrin [8]. Also, shear can increase the size of focal adhesions [29], [36], [197] and induce a directional elongation of them similar to the structure of focal adhesions during cell spreading or locomotion. The recruitment of adhesion proteins such as vinculin or paxillin enables a downstream signaling pathway [29].

Different strategies exist to investigate the impact of shear [190]. For instance, flow chambers or microfluidic devices allow the simulation of shear conditions similar to shear conditions experienced in blood vessels [8]. For this purpose, adherent or floating cells are usually subjected to variable fluid flow conditions within channels of defined geometry [190], but various researchers enhanced basic microfluidic devices [23], [198], [199]. For instance, Rupprecht et al. developed a microfluidic device to investigate detachment kinetics with real-time videomicroscopy [198]. A microneedle assay as described by Riveline et al. utilizes a thin needle that is brought in contact with a cell and moved along its surface applying shear to the cell [29]. Majedi and coworkers applied oscillatory forces using a shaker device [200], whereas Kouzbari et al. developed a custom-built cone and plate device applying both physiologic, steady shear and pathologic, oscillatory shear (abrupt change of rotation direction) [201]. Onaizah et al. followed a different approach by beam oscillation in close proximity to adherent cells, measuring the intracellular calcium response to investigate the propagation of calcium signalling [202]. In addition, Hagiwara and coworkers used beam oscillation to induce a defined streamline within the medium [203].

Although the abovementioned examples show the universal role of shear conditions and the diversity of methods for applying shear, the impact of shear on single bond strength has not yet been investigated, to my knowledge. Furthermore, sparsely understanding exists on how cancer cells are affected by shear. Shear forces may have a significant impact on cancer cells, especially during metastasis through the blood flow. Only recently, Huth et al. developed a technique to apply shear forces with a microneedle while measuring the distribution of traction forces [153]. Hence, new and more advanced techniques will allow a comprehensive study of cell behavior affected by shear conditions.

Here, I present an experimental setup to investigate the impact of various shear distances on cell detachment. For this purpose, a single fibroblast cell was attached

to a functionalized AFM cantilever and brought into contact with a substrate. During cell-substrate contact, the cell was sheared for a defined distance at a constant speed. Then, the cantilever was retracted to measure cell detachment. The outcome of this project resulted from the cooperative work with Yannic Hallier, a student who worked under my supervision and guidance. I show that the cell detachment is affected by the shear process and propose that certain shear distances improve cell detachment, whereas larger shear distances are harmful to cells. In addition, I show that shear decreases single bond strengths. To account for increased contact areas during the shear process, I developed a bidirectional shear process.

3.3.2 Experimental Design

The general concept to apply shear via AFM was a targeted and controlled movement of the stage during direct cell-substrate contact (see Figure 3.6). For this purpose, the stage was moved with constant speed in the x-direction for a defined distance (so-called shear distance). Afterwards, the cantilever was retracted with a predefined speed in the z-direction to detach the cell from the substrate.

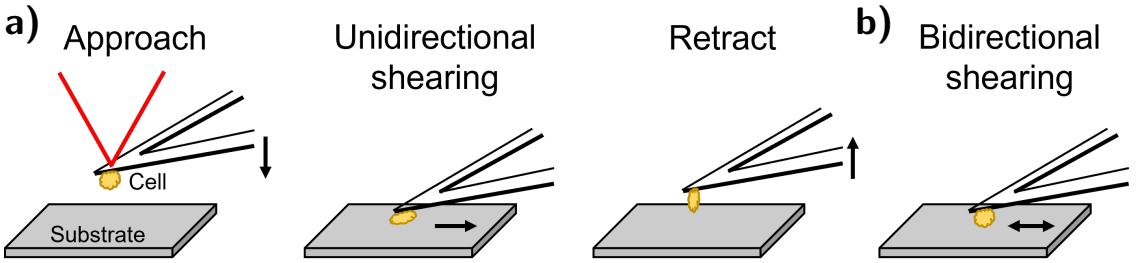

Figure 3.6: Visualization of the experimental design for AFM-based shear. a) A single cell was attached to an AFM cantilever. Then, the cantilever approached the substrate with a defined speed until a predefined setpoint force was reached. During cell-substrate contact, a unidirectional shear process was realized through a defined movement of the motorized stage beneath the substrate. It was essential that a consistent cell-substrate contact exists. Afterwards, the cantilever was retracted to completely detach the cell from the substrate. b) A bidirectional shear process was realized with a defined back and forth movement of the stage at a defined frequency for a certain duration instead of unidirectional shear.

Cantilever Calibration

The experiments were conducted on the CellHesion® 200 setup (see further details in Appendix B.1). Tipless MLCT-o10 cantilevers (type A, Bruker Corporation) were calibrated at five positions on glass. For this purpose, the sensitivity was determined in the linear regime of the approach curve of a force-distance curve (setpoint force: 2 V, speed: 15 µm/s) and the spring constant was measured with the thermal noise method (correction factor of 0.871). The mean value of the spring constant was used for the experiments, whereas the sensitivity had to be measured for each experiment.

Cantilever Functionalization

Calibrated cantilevers were washed 5 min in acetone before irradiation with UV light for 15 min. Then, the cantilevers were incubated in 50 µl of biotin-BSA (0.5 mg/ml in 0.1 M $NaOHCO_2$, pH 8.6, Sigma-Aldrich) overnight at 37°C. The next day, the cantilevers were washed 5 min in PBS and incubated in 50 µl streptavidin (0.5 mg/ml in 1x PBS, Sigma-Aldrich) for 10 min. They were washed 5 min in PBS again and incubated in 50 µl biotin-conA (0.2 mg/ml in 1x PBS, Sigma-Aldrich) for at least 20 min. Prior to use, the cantilevers were washed with PBS.

Biofunctionalization of Substrates

FluoroDish (World Precision Instruments, WPI) petri dishes with glass bottoms were used for all cell experiments. The glass bottom was functionalized with poly-D-lysine (PDL) by WPI. 500 µl glutaraldehyde (10 µl/ml in bidest. water) were added for 30 min. Then, the dish was washed extensively three times with water or PBS and incubated with 500 µl fibronectin (10 µg/ml in 1x PBS, Advanced BioMatrix, Inc.) overnight at 4°C. Prior to use, the dish was washed with PBS and filled with 3 ml CO_2 independent medium (Gibco).

Cell Culture

Rat embryonic fibroblast cells (REF 52-wt) were cultured according to Appendix B.3 in DMEM (Biochrom) with 10 % FBS (Biochrom) and 1 % Pen/Strep (Biochrom). A solution of 0.05 % Trypsin and 0.02 % EDTA (Sigma-Aldrich) was used for cell detachment. Cells were seeded in 6-well plates for the experiments and resuspended in CO_2 independent medium (Gibco) directly before use.

AFM-based Shear Experiments

A petri dish heater (JPK Instruments) was used to keep the temperature constant at 25°C. After the sensitivity of the cantilever was determined, 100 µl cell suspension were added to the petri dish. The cantilever was placed directly above a suitable cell and approached manually with 5 µm steps until contact with the cell. Then, the cantilever was retracted several µm to guarantee that the cell was successfully attached to the cantilever. 5-10 min incubation time ensured proper spreading on the cantilever.

For all experiments, a setpoint force of 0.5 nN and a cantilever speed of 10 µm/s in z- and x-directions with shear distances between ca. 1-9 µm were used. The contact times varied due to different shear distances (see Table 3.2).

Each cell was measured through two cycles with one cycle consisting of 20 force-distance curves without shear (referred to as "normal") and 20 force-distance curves with shear (so-called "shear"; i.e., detachment measurement after shearing the cell). This resulted in 80 force-distance curves maximum for each cell. The force-distance

curves were recorded alternately between two positions on the substrate. A specific script for the experimental planner of the JPK control software was necessary to conduct the shear experiments.

Table 3.2: Shear distances and contact times used

Shear distance [µm][1]	Contact time [s][1]
1	3.5
3	4.5
5	5
7	5.5
9	6

[1] Approximate values

Data Processing

Retract curves of the force-distance curves recorded were analyzed with the JPK SPM data processing software (version spm-6.0.63, JPK Instruments). At first, the curves were smoothed and the baseline was corrected for tilt and offset. Then, the tip-sample separation and the contact point were calculated. Afterwards, the curve minimum (i.e., detachment force) and the area under the retract curve (i.e., detachment energy) were measured. Additionally, the last rupture event (i.e., final step of the retract curve) was analyzed for its height.

Origin 9.1G (OriginLab Corporation) was used to create all graphs presented. The graphs show either mean values of a certain cell parameter (e.g., detachment force) calculated from up to 20 force-distance curves with standard deviations as error bars or boxplots that follow the convention described in Appendix B.2.

3.3.3 Establishment of AFM-based Shear System

The aim of this project was to investigate the impact of shear on cell detachment. Usually a fine needle is placed close to an adhering cell and moved along it to shear the cell up to several micrometers [29]. However, this makes the parallel measurement of cell detachment impossible. AFM single cell force spectroscopy is a perfect tool to characterize cell detachment and in principle the AFM cantilever can be used to shear a cell similar to the abovementioned method. To realize the combination of shear and cell detachment measurements, it is necessary that the cell is attached to the cantilever. Then, this arrangement permits two ways to apply shear: movement of the cantilever along the x- or y-direction or movement of the substrate underneath the cantilever. In both scenarios, the consistent interaction of the cantilever (or more precisely, the cell) with the substrate is necessary to guarantee a reliable shear situation. Especially the cantilever height (i.e., force

applied) is required to be constant throughout the experiment and the shear distance applied needs to be precise.

Most AFMs that can move the cantilever in the x- or y-direction are used for imaging purposes, thus usually having a short z-range (i.e., available distance for cantilever approach and retract; e.g., 15 µm at the NanoWizard® 3). However, a much larger z-range is usually necessary to detach a whole cell from a substrate. The CellHesion® 200 (JPK Instruments) was specifically developed for cell experiments and has a z-range of 100 µm but a movement in x- or y-direction is not possible. To circumvent this drawback, a motorized stage was used in combination with the CellHesion® 200 allowing a controlled movement of the substrate. Since a movement of the stage during cantilever-substrate contact can cause perturbations, it is usually prohibited by the software. The implementation of such a stage movement was realized in cooperation with Dr. Thomas Henze from JPK Instruments. For this purpose, JPK Instruments released a specific software version for our setup and we developed a Python script to regulate the shear process. For the conduct of a shear experiment, it is necessary to load the Python script into the software. Starting the script results in the following steps: cantilever approach up to predefined setpoint force, small break before cantilever movement along predefined direction (here: x-direction) for a specific length (i.e., shear distance) followed by immediate cantilever retract to completely detach the cell from the substrate.

The motorized stage used was developed to measure at single positions with micrometer precision but not for movement along a certain direction. Preliminary experiments showed that the predefined shear distance entered into the Python script deviated from the actual shear distance applied (i.e., movement along the substrate). To guarantee reliable shear distances, the relation between predefined shear distances (i.e., shear distance entered into the Python script) and actual shear distances applied was measured. For this purpose, a range of 1-19 µm shear distances was applied and each corresponding real shear distance was measured from microscopy images. The results are presented in Figure 3.7, where each square shows the mean value of 5 measurements with the standard deviation as error bars.

The relation between predefined shear distance and actual shear distance applied is almost linear. The values used for the shear experiments conducted are shown in Table 3.3. The contact times previously shown in Table 3.2 are included for greater clarity.

The aim of this study was to investigate the impact of shear on cell detachment. To allow a direct comparison of shear situations (so-called “shear” mode) to standard, no shear situations (so-called “normal” mode), single cells were measured through two cycles, where one cycle was defined as a subsequent measurement of normal and shear modes. To verify successful cell-cantilever attachment, the first cycle started with normal detachment measurements as previously described as single cell force spectroscopy in Section 1.3.2. In short, a defined cell-substrate contact was produced through repetitive cantilever movement in the z-direction (approach and retract). Then, during the shear mode, the abovementioned Python script was applied to shear the cell for a predefined shear distance. To identify the persistence of shear (i.e., lasting impact on the cell), the described order was repeated in a second cycle.

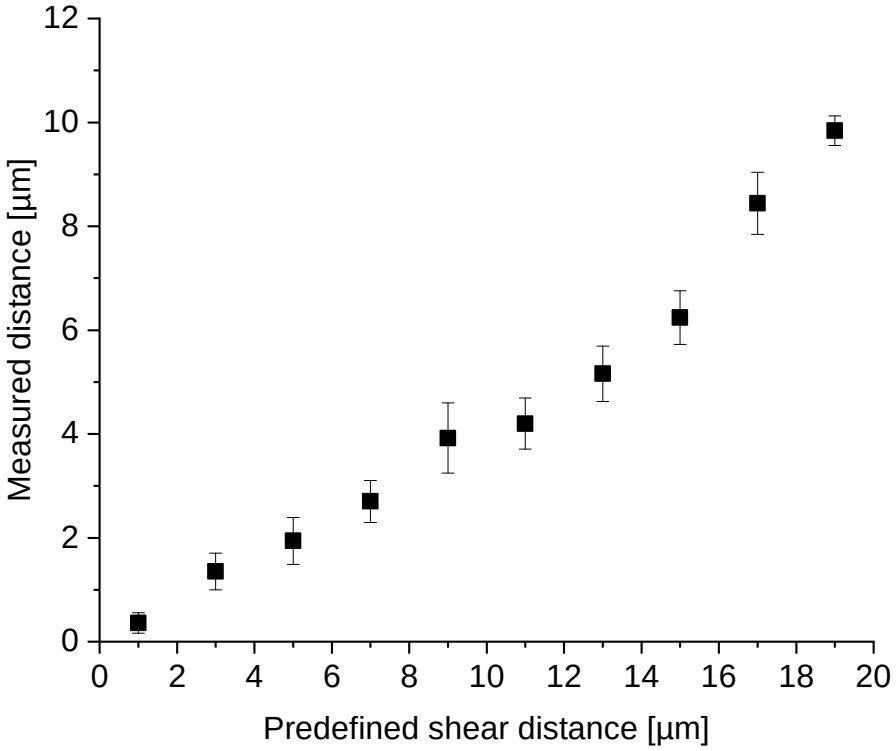

Figure 3.7: Relation between predefined shear distances and actual shear distance applied. Values for the shear distance between 1-19 µm were entered in the Python script as predefined shear distance. The actual shear distance applied was measured from microscopy images and shows an almost linear relation to the predefined shear distances.

Table 3.3: Overview of predefined and actual shear distances applied and resulting contact times

Predefined shear distance [µm]	Applied shear distance [µm][1]	Resulting contact time [s][1]
2	1	3.5
7	3	4.5
13	5	5.0
16	7	5.5
18	9	6.0

[1] Approximate values

All measurement parameters (e.g., setpoint force, speed, shear distance, contact time) were kept constant throughout the measurement of a single cell to avoid side effects from experimental parameters. From experience, it was clear that cells only survive a limited number of force-distance curves, yet a sufficient number of curves

is necessary to reflect cell detachment reliably. Hence, 20 force-distance curves were recorded for each mode. This gave a total of 80 force-distance curves for each completely measured cell.

3.3.4 Fibroblast Cells Are Affected by AFM-based Shear

A single fibroblast cell was attached to a functionalized cantilever. After an initial incubation time, a first cycle of normal detachment (no shear) and shear measurements was conducted. At first, 20 force-distance curves were recorded without shear with a setpoint force of 0.5 nN and 10 µm/s approach and retract speed. Then, 20 force-distance curves were recorded with shear. For this purpose, the cantilever was approached to the substrate with 10 µm/s up to 0.5 nN setpoint force, then the stage moved along a predefined direction for a defined distance to shear the attached cell (shear distances between ca. 1-9 µm) and in the end, the cantilever was retracted with 10 µm/s. After finishing this first cycle, the whole process was repeated to record a second cycle. All recorded force-distance curves were analyzed for the detachment force, detachment energy and the height of the last rupture event (so-called last rupture force).

Figure 3.8 shows the retract curves of representative force-distance curves for a normal cell detachment (black squares) and cell detachments after shear with shear distances of 1 µm (orange diamonds), 3 µm (blue upward-pointing triangles) and 9 µm (magenta downward-pointing triangles). The normal measurement showed the expected progress, whereas small and medium shear distances resulted in larger detachment forces (i.e., minimum of retract curve) and detachment energies (i.e., area under the curve). The additional progress of the curves (e.g., number of rupture events) was similar to normal curves. However, large shear distances showed a significant reduction of the detachment force, and detachment energy as well as a limited number of rupture events was visible. Hence, small and medium shear distances reinforced cell detachment, whereas larger shear distances resulted in reduced cell detachment compared to normal detachment measurements.

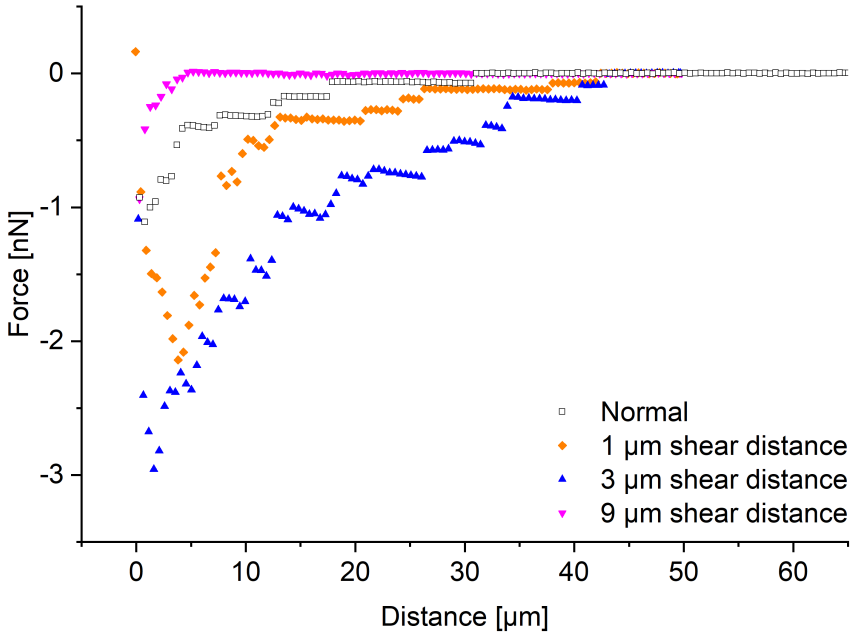

Figure 3.8: Representative retract curves show a positive impact of smaller shear distances. The retract curves of measurements with shear distances of 1 µm (orange diamonds) and 3 µm (blue upward-pointing triangles) showed increased curve minima (i.e., larger detachment forces) and areas under the curve (i.e., larger detachment energies) compared to retract curves of normal measurements (black squares). Larger shear distances (here: 9 µm, magenta downward-pointing triangles) resulted in reduced detachment forces, energies and a limited number of rupture events. Hence, small and medium shear distances reinforced cell detachment, whereas larger shear distances resulted in impaired cell detachment (e.g., decreased curve minimum, reduction of rupture events) compared to normal detachment measurements.

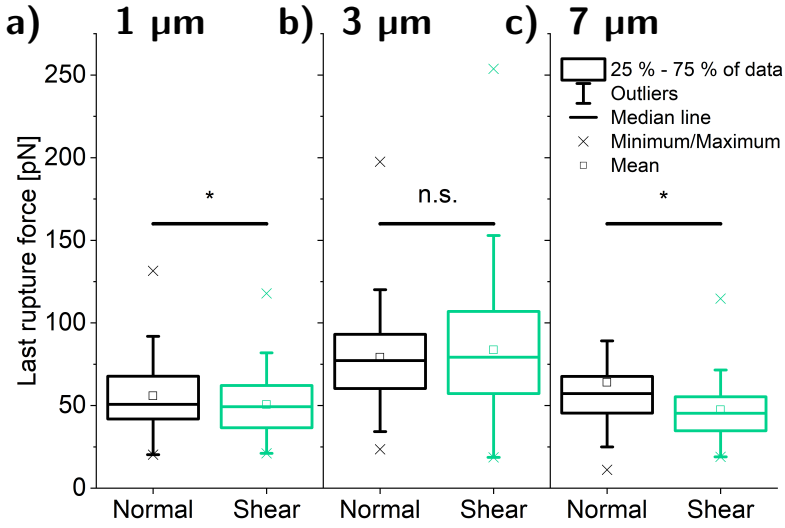

Figure 3.9: Variations of last rupture forces for measurements with variable shear distances as a function of a "normal" and a "shear" mode. Comparison of distributions of the last rupture forces measured for shear distances of a) 1 µm, b) 3 µm and c) 7 µm. The graphs for the remaining shear distances are shown in Appendix D. All last rupture forces decreased for the shear mode (significance level of * $p < 0.05$), except for 3 µm shear applied, where no significant (n.s.) difference was measured. Such decreases are likely associated with weakening of single bond strength.

Figure 3.9 shows the distribution of the last rupture forces for "normal" and "shear" modes measured with shear distances of a) 1 µm, b) 3 µm and c) 7 µm, respectively. The boxplot and significance levels follow the convention described in Appendix B.2. The graph for 1 µm is representative for a shear distance of 5 µm and the graph for 7 µm shows similar results to shear distances of 9 µm (see Appendix D).

For measurements with shear distances of 1 µm, 5 µm, 7 µm and 9 µm, the last rupture forces decreased significantly compared to the normal measurement. For a shear process of 3 µm, no significant (n.s.) difference was observed. A decrease in last rupture force indicates a weakening of the single bond strength. Since a slip bond has a smaller lifetime and withstands lower rupture forces, shear might induce a mechanism that can unhook a catch bond forming a slip bond [204].

Figure 3.10 shows the mean detachment forces (left column) and energies (right column) for shear modes measured with shear distances of 1 µm, 3 µm and 7 µm each for four cells. For simplicity, cell numbers are renamed to cell 1-4. Each symbol represents the mean value of up to 20 force-distance curves analyzed and the error bars denote the standard deviations. The different modes ("normal", "shear") are displayed on the x-axis. The graphs measured with 3 µm are representative for measurements with a shear distance of 5 µm, whereas the graphs for a shear distance of 7 µm show similar results to measurements with shear distances of 9 µm (see Appendix D).

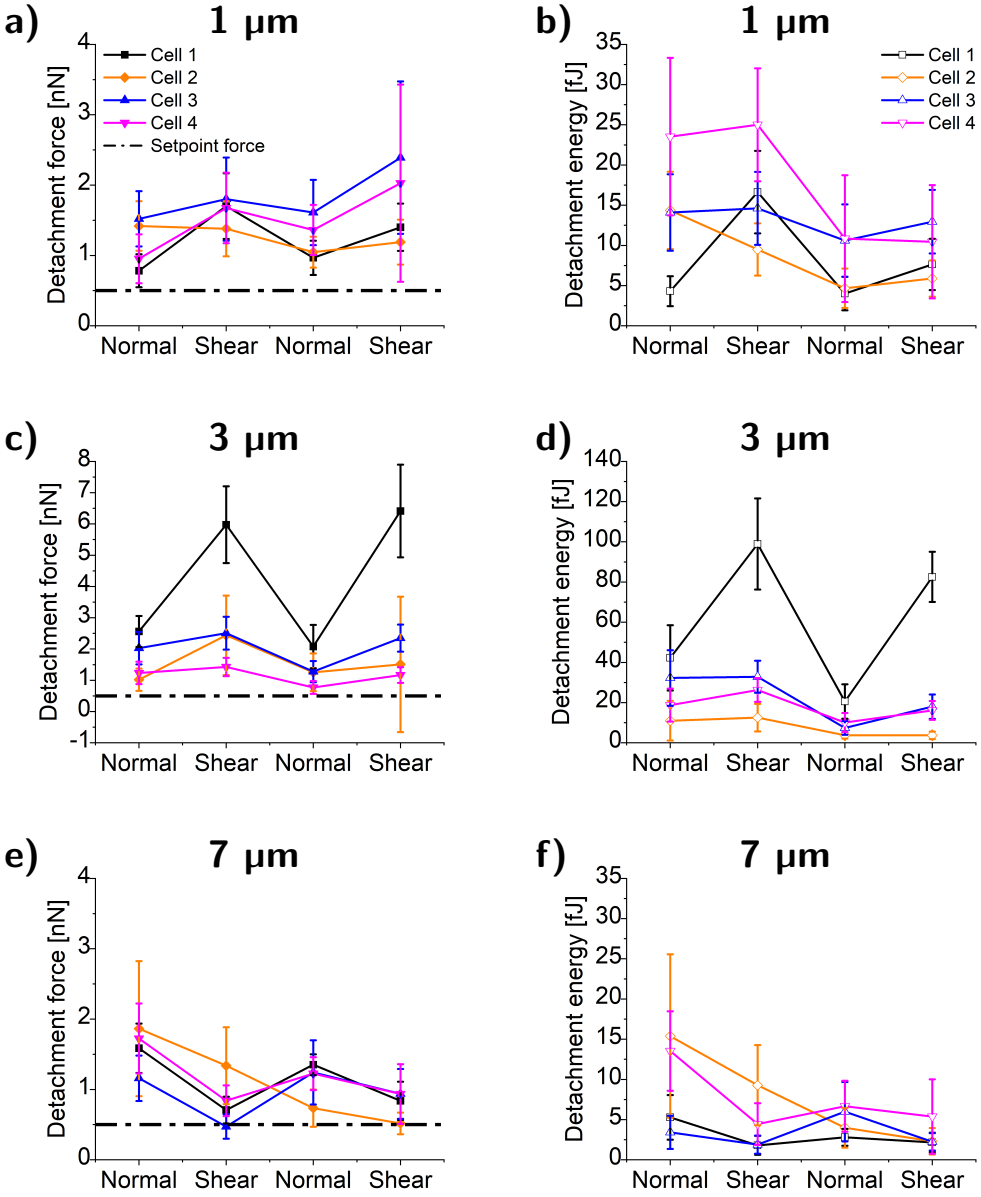

Figure 3.10: Mean detachment forces and energies for variable shear distances as a function of "normal" and "shear" modes. The left column shows the mean values of detachment forces measured with shear distances of a) 1 µm, c) 3 µm and e) 7 µm. The right column (b), d), f)) shows the mean values of detachment energies measured with the same shear distances. The error bars denote the standard deviations and the graphs for the remaining shear distances are shown in Appendix D. For simplicity, cell numbers are renamed to cell 1-4. For shear distances of 1-5 µm, increased detachment forces and energies were determined compared to results of the normal measurements, whereas shear distances of 7-9 µm reduced the detachment forces and energies. No memory effect (i.e., altered detachment forces or energies) was visible for the second normal measurements but the second shear process showed similar results to the first shear process. Since the detachment forces for 1 µm increase even further during the second shear mode, an overall reinforced cell detachment can be concluded for a shear distance of 1 µm. Shear distances larger than 7 µm, on the other hand, seemed to be harmful to the cells since a decrease of both detachment forces and energies was determined (e.g., partial ruptures during shear process).

At first, 20 force-distance curves were recorded without shear (so-called "normal") to test the cell-cantilever attachment and to serve as a basis for the shear modes. Then, 20 force-distance curves were recorded with a certain shear distance (e.g., 1 µm, see Figure 3.10 a)). For shear distances of 1-5 µm, larger detachment forces were determined compared to the results of the normal measurements. However, shear distances of 7-9 µm reduced the detachment forces determined. Then, a second cycle of first 20 normal, followed by 20 shear measurements was conducted. During the second normal measurement, the detachment forces determined returned to the level of the first normal measurement and then again showed increased detachment forces for shear distances up to 5 µm during the second shear mode or reduced detachment forces for shear distances above 7 µm. Since the detachment forces during the second shear mode for 1 µm increase even further than during the first shear mode, an overall reinforced cell detachment can be concluded for a shear distance of 1 µm. An almost overall constant progress was detected for shear distances of 3-5 µm, where cell 1 for 3 µm and cell 3 for 5 µm show exceptions from this observation. Additionally, I suggest that shear distances larger than 7 µm resulted in partial ruptures during the shear process, which might be harmful to the cells. In general, the progress of the detachment energy is similar to the progress of the detachment force, yet less pronounced. Exceptions are, for example, cell 4 measured with a shear distance of 1 µm and cell 1 measured with a shear distance of 7 µm.

Since the last rupture force for a "shear" situation decreased (except for 3 µm shear distance), the increased detachment forces for shear distances up to 5 µm may result from an increased number of bonds, a higher rate of rebinding during the retract phase or a change of the tethers prior to a bond rupture. Furthermore, it may be possible that certain shear distances induce a conformational change or deformation mechanism of binding proteins that initiates internal signaling [20], [192]. For instance, talin unfolding is known to allow the binding of additional adhesion proteins, such as vinculin, which can lead to a growth of focal adhesions [47] but also fibronectin can provide additional binding sites upon stretching [29]. Hence, cell detachment is impeded. Since larger shear distances have an adverse effect on cell detachment, I propose that a possible conformational change cannot compensate the cell damage due to large shear. Besides integrins, there are mechanosensitive ion channels that can open upon external forces [60], [65], [66]. For instance, Piezo1 is known to open due to membrane stretch, indentation and/or deflection of underlying pillars [51]. Since a shear process could induce similar forces to the membrane of a cell as a deflection assay, the opening of ion channels may be triggered to adapt cell detachment.

Pressing a cell onto a substrate with a defined setpoint force leads to a specific contact area between cell and substrate. The size of the contact area can be related to the level of adhesion [109] and, in general, larger setpoint forces result in larger contact areas, which means that more integrins can bind to the substrate [14], [160]. This ultimately makes it more difficult to detach a cell from a substrate [205]. A similar effect might have occurred in these experiments since the contact area most likely increases during the shear process. However, it is reasonable that only certain shear distances have an impact. Insufficient shear distances may have no

or hidden effects, whereas large shear distances can have an adverse impact on the cell-substrate interaction. This is justified by the assumption that large shear distances partially rupture the cell already during the shear process in addition to the subsequent retract phase. The observation of decreasing detachment forces and energies for the second "normal" measurement suggests that larger shear distances were harmful to the cells. As seen in Table 3.2, the shear distances used lead to various contact times between 3.5-6 s. A longer contact time gives a cell more time to attach to a substrate. This will usually result in larger detachment forces [109]. Since larger shear distances (i.e., larger contact times) favored cell detachment, it is probable that a combination of the abovementioned explanations emerged.

3.3.5 Development of AFM-based Bidirectional Shear

In the previous section, I explained the relevance of contact area and contact time for the impact of the shear process on cell detachment. The contact time is always directly linked to the shear distance and can only be influenced through variation of shear speeds, which will most likely affect the outcome as well. However, there are different ways to manipulate the contact area. Here, I discuss three possible ways to take the impact of the contact area into account: correlation of contact area and cell detachment, specific pattern of ECM proteins and bidirectional shear to maintain a constant contact area.

The first solution would be the continuous observation of the contact area during the experiment and the resultant correlation of cell detachment measured and contact area. Advanced microscopy techniques such as total internal reflection fluorescence microscopy (TIRFM) are required to achieve high resolution of the exact cell contact area. In addition to the high complexity of data interpretation and the high costs involved, cell variability would make the correlation very complex. Hence, I focused on more promising alternatives.

The production of substrates functionalized with ECM proteins of a defined micropattern could be another solution. Since integrin-ECM binding is necessary for the formation of focal contacts due to external forces [29], a treatment of the areas between the micropatterned areas (e.g., PLL-PEG coating [196]) is required to prohibit cell attachment other than the desired areas. Preliminary experiments showed that the implementation of micropatterned substrates into the shear system presented is difficult. Since a defined cell-micropattern interaction is required to determine the resulting contact area, it is necessary that the ECM proteins are visible. For this purpose, ECM proteins with fluorescent labels can be used. My collaboration partner Joel Christian (Department of Cellular Biophysics, Max Planck Institute for Medical Research, Heidelberg) produced glass substrates with fluorescently labeled fibronectin at a PRIMO system (Alvéole) and I tested these samples in our system. However, it was not possible to conduct all experimental steps required (successful cell attachment, cantilever positioning) prior to the measurements without losing the fluorescence of the fibronectin (bleaching effect).

The third solution was the application of back and forth shear for a defined shear distance with a defined frequency for a defined time (i.e., number of periods). I

call this "bidirectional shear" as the cell is sheared back and forth at the same position (see Figure 3.6 b)). This guarantees a consistent contact area throughout the experiment. Since the frequency of a stimulation can influence cell behavior as well, a great benefit of bidirectional shear is the chance to investigate the impact of varying frequencies on cell detachment.

Bidirectional shear was not possible with the motorized stage previously used because the precision was not large enough and a precise change of direction was not possible on a short time scale. Fortunately, I was able to install a motorized stage with nanometer precision (so-called TAO module, JPK Instruments) on our AFM setup. I developed another Python script together with Dr. Thomas Henze (JPK Instruments) that allows precise application of bidirectional shear. The user can freely choose the shear distance (theoretically up to limit of the stage of 100 µm), the shear frequency and the number of periods. Furthermore, it is possible to decide for a sinusoidal or triangular signal for the shear process.

3.3.6 Conclusion

Shear proved to be essential for cells and their behavior. For instance, the size and orientation of focal adhesions can be altered by shear [29]. In addition, it was shown that shear processes can have a permanent impact on actin reorganization, whereas migration rates recover [192]. The role of shear flow disturbances for vascular functionality and/or blood clot formation bolsters the medical interest in studies of different shear conditions. However, detailed knowledge about the role of single bond strengths has been missing until now. Although fibroblast cells are not constantly under the influence of shear, they are exceptional mechanosensors and may give important evidence as to how different shear conditions can be utilized.

Here, I presented a system to shear a single cell with AFM that allows the parallel measurement of cell detachment. For this purpose, a single cell was attached to an AFM cantilever and sheared for a defined distance during cell-substrate contact with the help of a motorized stage. To my knowledge, such a shear system is unique and, in principle, it can be used for different cell types, notwithstanding possible necessary adaptation of the experimental parameters (e.g., setpoint force, contact times) [4]. To prove the applicability of the system presented, fibroblast cells were used as proof of principle. I showed that last rupture forces (i.e., single bond strengths) were affected by the shear process and led to a significant decrease for all shear distances applied, except for 3 µm. Furthermore, I showed that shear distances up to 5 µm reinforced detachment forces and energies compared to cell detachment measurements without shear. However, larger shear distances investigated seem to harm the cell as decreased detachment forces and energies were determined. It is reasonable that these shear distances rupture some parts of the cell already during the shear process (i.e., before the actual retract phase). Since the last rupture forces decreased for all but measurements with shear distances of 3 µm, I suggest that the enhancement of cell detachment observed was related to a higher number of bonds, increased rebinding events during the retract and/or influenced tethers prior to a rupture event. In addition, the shear process as described here increases the

cell-substrate contact area. Hence, more integrin binding occurs, which impedes cell detachment (i.e., increase of detachment force and energy). However, a combination of the abovementioned observations is likely.

Riveline et al. reported that shear-induced growth of focal complexes started 1 min after starting to shear a cell [29], whereas actin remodeling required ca. 5 min [192]. Since the recording of a single force-distance curve took ca. 20 s, both focal complex growth and actin remodeling were likely initiated during the shear process presented. I recommend using staining techniques to visualize adhesion proteins or actin transfection as previously reported by Oakes and coworkers for future experiments [183], [206]. Cell detachment investigated by flow showed that not only the arrangement of adhesion bonds related to number, distribution and strength impacts cell detachment but cell spreading area and the surface topography of cells are crucial as well [207]. Hence, the visualization of the cell contact area via total internal reflection fluorescence microscopy, for example, would be beneficial for a more comprehensive study of the impact of shear.

To account for an increased contact area, I developed bidirectional shear with AFM that permits a back and forth movement of the stage to apply shear distances with a defined frequency. Further research will be necessary to identify the role of bidirectional shear for cell detachment.

In addition to the visualization of the cell contact area, the combination with TFM similar to the work by Huth et al. will allow a profound study of the force transmission of cells [153]. Ultimately, the findings about the impacts of shear conditions will help treatment of diseases, such as atherosclerosis, and the development of new implant materials (e.g., invention of biomaterials that promote cell adhesion upon mechanical stimulation).

3.4 AFM-based Modulation System for Single Cell Manipulation

3.4.1 Introduction

In the body, blood pressure stretches blood vessel walls [12], body movements compress bone tissue [7], [202], blood flow shears blood cells and endothelial cells of the blood vessel [167], [190], [208], heart muscle contraction and expansion changes constantly [209] or smooth muscle cells permanently experience dynamic mechanical loading due to breathing [210], to name some examples of external cues. The mechanical loads experienced in bone tissue can regulate the bone growth and/or fracture repair [202], [211]. For instance, mechanosensitive osteocytes (part of the bone matrix) regulate the bone structure according to the mechanical load experienced [202], [211], [212] and the functionality of bone tissue depends on mechanical stimuli for activating signalling pathways that remodel bone [211], [212]. In addition, both exhausting exercise and inactivity can affect bone mass or can lead to joint dysfunction [51], [213].

The research field of mechanotransduction tries to utilize the ability of cells to sense and respond to external cues for medical purposes. For instance, targeted stem cell differentiation allows advanced strategies for tissue engineering purposes, or pathogenic cell capture, as proposed by Gutekunst et al., offers new possibilities for disease prevention [94]. But also the detection of cell stiffness variations as result of tumor formation is essential for disease diagnostics [175]. In addition, oscillatory stimuli are essential for artificial pacemakers that guarantee the functionality of the heart muscle through electrical impulses [214].

The investigation of systems aiming to dynamically control cell adhesion through oscillatory stimulation will be beneficial for tissue engineering applications and/or the development of new strategies for implants [163]. Substrate stretching systems, such as reported by various research groups, allow simultaneous investigation of mechanical stimulation on multiple cells or cell collectives [165]–[168], [215]. These studies showed that many cells (e.g., fibroblast cells, arterial smooth muscle cells, adipose derived stem cells) respond to substrate stretching [165], [168], [215]. Under static strain, cell orientation is often parallel to the stretch direction, whereas cyclic stretching results in perpendicular cell alignment [168], [215]. Three main factors have been proposed to affect cell orientation under cyclic stretching: duration, amplitude and frequency [167]. Dartsch et al. showed that stretch amplitude and time required for cell orientation correlate [165]. Cell orientation occurred faster and with higher degrees under larger stretch amplitudes [165]. Jungbauer et al. supported these findings and showed that the time required for cell orientation relates also to stretch frequencies having faster orientation at higher frequencies [168]. Moreover, a cell-dependent frequency threshold exists that induces cell orientation [168]. In addition, Rabbani et al. showed that cyclic stretching at 1 Hz leads to cell stiffening of adipose derived stem cells and differentiation towards smooth muscle cells [215]. Hatami et al. combined substrate stretching with micropipette aspiration to characterize mechanical properties of cells and showed that larger stretch amplitudes and longer duration lead to lower deformation and a stiffening of the endothelial cells investigated [216]. Since thermoresponsive materials, such as poly(*N*-isopropylacrylamide), often used to switch between adhesion promoting and impeding situations prevent local and fast stimulations [163], Kadem et al. established a light-triggered switching of biofunctionalized azobenzenes fixed to a substrate that allows mechanical stimulation of integrin receptors on a millisecond time scale [217]. The experiments showed increased cell detachment upon oscillation of the azobenzenes and Kadem et al. concluded a transmission of the mechanical stimulus from azobenzenes to integrins that triggers a mechanotransduction pathway to reinforce cell detachment [217]. Hippler et al. developed a 3D microenvironment, in which cells adhere to four platforms that stretch the cells upon expansion of the underlying substrate [218]. Within the first 30 min of cell stretching, cells reach a new equilibrium with doubled traction forces and a remodeled actin cytoskeleton at stretches up to 25 %. Hippler et al. proposed the necessity of actomyosin contractility for mechanical homeostasis (natural equilibrium state). Surface acoustic wave (SAW) sensors have been adapted for usage in biological applications [169], [170], [219]. For instance, Sivanantha et al. utilized a SAW system for selective removal of cell populations and showed that malaria-infected red blood cells could be easier re-

moved from a substrate than healthy red blood cells suggesting the use of the SAW system in rapid diagnostics [219]. Guo et al. developed a cell manipulation system with SAWs that allows the manipulation of intercellular distances, the shape of cell aggregates in suspension and a subsequent transformation to the adherent state [170]. Due to the high degree of control over cell arrangement, the cell-cell and/or cell-substrate communication can be investigated [170]. In addition, quartz crystal microbalances are a special type of SAW that can be utilized for monitoring cell spreading [121]. Its resonance oscillation is very sensitive to material adsorption on the quartz surface. Hence, cell adhesion based on ligand-receptor interactions can be detected with high precision, whereas loose attachment due to unspecific binding is not detected [169]. Heitmann et al. exploit the previous findings to investigate how lateral oscillation amplitudes affect adhesion kinetics and showed the existence of a critical oscillation amplitude that prevents cell adhesion to the quartz surface [169]. Adhesion of all cell lines investigated was impossible at an amplitude of 35 nm but was not sufficient to disrupt stable cell-substrate interactions once formed [169]. Since extracellular domains of integrins extend around 20 nm out of the membrane, Heitmann et al. concluded that integrin binding is not possible at larger oscillations [169]. The works of both Weafer et al. and Irons et al. developed AFM-based techniques to dynamically compress adhering cells with a bead attached to an AFM cantilever [210], [213]. Irons et al. applied amplitudes of 400-2000 nm with a fibronectin-coated bead to smooth muscle cells and showed that large amplitudes lead to bond ruptures during the oscillation [210]. Weafer et al. used a 150 µm bead inducing strains of 0-25 % or 10-35 % to osteoblast cells at 1 Hz and showed that osteoblast cells are resistant to dynamic compression and stretching as long as a contractile actin cytoskeleton exists, whereas cells with chemically disrupted actin cytoskeleton showed less or no resistance [213], [220].

Although these examples show a variety of stimulation schemes, there is no technique employing an *in situ* manipulation of single cells that is capable of correlating stimulation frequencies and amplitudes to initial cell adhesion and single bond strengths, to my knowledge. I aim to fill this gap with an experimental setup that allows the application of oscillatory forces to single cells and the subsequent correlation of stimulation parameters (frequency and amplitude) to initial cell adhesion. For this purpose, a single cell was attached to an AFM cantilever that was modulated with a defined frequency and amplitude during cell-substrate contact. After the contact phase, the cantilever was retracted and cell detachment was measured.

In a first phase, I investigated the role of modulation settings on fibroblast cells and showed that large amplitudes increase cell detachment, whereas very small amplitudes seem to be harmful to cells. In addition, the step positions determined followed the same trend as detachment forces and energies. Since reference measurements applying larger setpoint forces showed increased cell detachment as well, I suggest a combined effect of modulation and additional force due to the modulation applied. In a second phase, the student Johanna Buck worked under my supervision and guidance to investigate the role of the mechanosensitive ion channel Piezo1. For this purpose, oscillatory forces were applied to human embryonic kidney cells with or without Piezo1. Since stronger cell detachment was detected, the contact time

was reduced and a 3 s modulation at 2 Hz was successfully established. Initial results indicate a slight impact of Piezo1 modulation on initial cell adhesion.

3.4.2 Experimental Design

The general concept to apply oscillatory forces via AFM was a precise repetitive movement of the cantilever in the z-direction while the cell was in contact with the substrate (see Figure 3.11). For this purpose, the cantilever movement was modulated with a predefined frequency and amplitude to induce a defined oscillation of the cantilever. This kind of cantilever movement is similar to oscillations made while imaging a sample's topography.

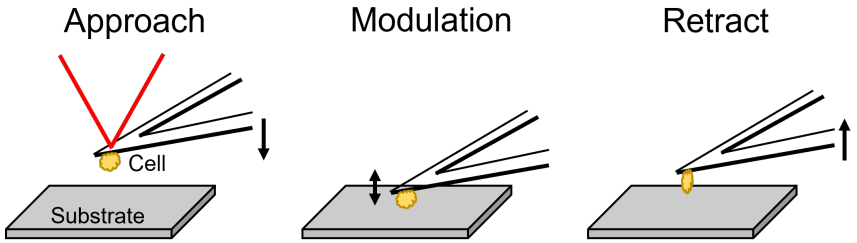

Figure 3.11: Visualization of the concept to apply oscillatory forces with AFM. A single cell is attached to a cantilever and approached to the substrate. A modulation segment replaces the contact phase, where the cantilever is modulated with a defined frequency to induce an oscillation. After a defined number of periods, the cantilever is retracted to detach the cell from the substrate.

Cantilever Preparation

The experiments were conducted on the CellHesion® 200 or the NanoWizard® 3 setup (see further details in Appendix B.1). Tipless MLCT-o10 cantilevers (type A, Bruker Corporation) were calibrated on glass in air. For this purpose, 5 force-distance curves were recorded at 9 different positions with a setpoint force of 3-4 V and a speed of 10 µm/s. The baseline was corrected for tilt and offset and the slope of the linear region of the approach curve was calculated with the JPK data processing software (version 6.1.172, JPK Instruments). Then, the sensitivity was calculated from the inverse mean of the slopes and the spring constant was calibrated once by applying the thermal noise method. The spring constant determined was used for all experiments. The cantilevers were functionalized with conA as described in Section 3.3.2. Prior to cell attachment, the sensitivity was determined with one force-distance curve and the abovementioned settings.

Biofunctionalization of Substrates

The functionalization of substrates was conducted similar to Section 3.3.2. However, a fibronectin concentration of 20 µg/ml in bidest. water with an overnight incubation at room temperature was used. To improve the cell attachment process, only 100 µl

fibronectin solution was used to partially cover the petri dish (marked on the bottom of the petri dish).

Cell Culture

Rat embryonic fibroblast cells (REF 52-wt) were cultured as described in Appendix B.3 in DMEM with 10 % FBS. Accutase™ (Sigma-Aldrich) was used for cell detachment. Cells were seeded in 6-well plates for the experiments and resuspended in CO_2 independent medium (Gibco) directly before use.

Human embryonic kidney cells (HEK293T, courtesy of Dr. Kate Poole, University of New South Wales, Sydney, Australia) were cultured at 37°C with 5 % carbon dioxide content and passaged at 80-95 % confluency. For this purpose, the cells were washed with PBS and incubated with Accutase™ (Sigma-Aldrich) for 1-2 min at 37°C. Then, the cell suspension was centrifuged at 200 g for 4 min. The supernatant was removed and the cell pellet was resuspended with fresh medium. The medium of the control cells (Piezo1 knock-out) was DMEM (Gibco) with 10 % FBS (Sigma-Aldrich, F9423), 1 % Pen/Strep (Gibco) and 4 µg/ml blasticidin (10 mg/ml stock solution, Sigma-Aldrich). The medium for the Piezo1 cells contained additional 100 µg/ml hygromycin (50 mg/ml stock solution, Carl Roth). The seeding densities varied between 1:4 and 1:20 for culturing. The maximum passage was 15. For experiments, 40,000-100,000 cells were seeded in 6-well plates and harvested with 600 µl EDTA (0.02 % in PBS, Sigma-Aldrich). The other steps remained the same but the supernatant was resuspended with CO_2 independent medium (Gibco). The Piezo1 cells required an induction with tetracycline (1.0 µg/ml in bidest. water, Carl Roth) 4 h prior to cell harvest, which was conducted not later than 5 min after the induction time ended.

AFM-based Modulation Experiments

A petri dish heater (JPK Instruments) was used to keep the temperature constantly at 36°C. After the sensitivity of the cantilever was determined, 100 µl cell suspension were added to the petri dish. The cantilever was placed directly above a suitable cell and approached manually with 1 µm steps until contact with the cell. Then, the cantilever was retracted several µm to guarantee that the cell was successfully attached to the cantilever. 15 min incubation time ensured proper spreading on the cantilever. For all experiments, a setpoint force of 0.5 nN, a cantilever approach and retract speed of 5 µm/s and a contact time of 5 s (REF 52-wt) or 3 s (HEK293T) were used. Each cell was measured through three cycles, where one cycle consisted of 20 force-distance curves without modulation (so-called "normal") and 20 force-distance curves with modulation (so-called "modulation"; i.e., detachment measurement after modulation of the cell) or with additional force applied (so-called "reference"). The modulation was controlled with a modulation segment of the force ramp designer implemented in the AFM control software and oscillation frequencies of 1-10 Hz and amplitudes of 10 nm or 1000 nm were applied. A maximum of 120 force-distance curves were recorded for each cell.

Data Processing

Retract curves of the recorded force-distance curves were analyzed with the JPK SPM data processing software (version 6.1.65, JPK Instruments). At first, the baseline was corrected for tilt and offset. Then, the tip-sample separation and the contact point were calculated. Afterwards, the curve minimum (i.e., detachment force) and the area under the retract curve (i.e., detachment energy) were measured. Additionally, the last rupture event (i.e., final step of the retract curve) was analyzed for its step height (so-called last rupture force), step position as well as slope and length of the plateau region prior to the rupture.

Origin 9.1G (OriginLab Corporation) or Python was used to create all graphs presented. The boxplots follow the convention described in Appendix B.2.

3.4.3 Establishment of AFM-based Oscillatory Manipulations

The general idea of the project was the application of oscillatory pushing and pulling on single cells to investigate the impact of different oscillation frequencies and amplitudes on cell detachment. The AFM is an excellent tool to measure cell detachment and navigation of cantilever movements via piezomotors permits a precise stimulation. The force ramp designer implemented in the JPK control software allows a free configuration of each individual experimental step (so-called segment). The simplest set for normal cell detachment measurements would contain three segments: approach, contact and retract.

I used the force ramp designer to implement a so-called modulation segment instead of the contact segment. It is a preinstalled segment at the NanoWizard® 3 that induces a cantilever oscillation at a defined frequency and amplitude for a defined number of periods, which defines the duration of the oscillation (e.g., 5 periods at 1 Hz results in a 5 s oscillation during cell-substrate contact). However, a cantilever oscillation at a large z-range was not intended by JPK Instruments as it may induce perturbations. Hence, the activation of the modulation segment at the CellHesion® 200 was required to allow cantilever oscillation at large z-ranges (i.e., ca. 100 µm), which are necessary to measure whole cell detachments.

After the successful activation, I modulated single fibroblast cells with different modulation frequencies and amplitudes (see Figure 3 in Appendix E). Since cell detachment measured with AFM single cell force spectroscopy correlates with the setpoint forces applied and the cantilever oscillation applies additional forces to the cell, I checked force-time curves for the degree of additional forces during the modulation segment. Figure 3.12 shows force-time curves for a) a pilot modulation (10 nm, 1 Hz, 5 periods) and b) a normal measurement (0.5 nN, 5 s contact time).

After the setpoint force of 0.5 nN was reached (dashed line), the force applied increased by a multiple of the setpoint force throughout the modulation segment (see Figure 3.12 a)), which was not indented. To prove that the increased force was specifically related to the modulation segment, Figure 3.12 b) shows an example

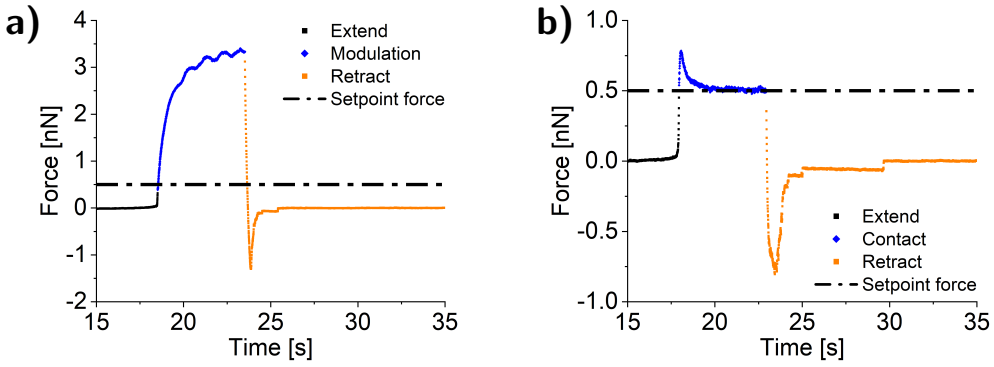

Figure 3.12: Visualization of representative force-time curves. a) The representative force-time curve for a pilot modulation with a 10 nm amplitude and 1 Hz frequency shows that the force applied increased by a multiple of the setpoint force throughout the modulation segment. This produced an unpredictable artifact of additional force applied resulting in a larger contact area that was not intended and would have been difficult to interpret due to its arbitrariness. b) The representative force-time curve of a normal measurement shows that the force applied was steady at the setpoint force after an initial small increase.

force-time curve of a normal mode. Initially, the force exceeded the setpoint force although it relaxed to the setpoint force after the first second of the contact phase. Hence, the modulation segment presented induced an unpredictable artifact that applied additional force to the cell resulting in a larger contact area. Contact area and cell detachment correlate but this artifact produced rather arbitrary impacts on the cell, which was not desired and would have been difficult to interpret. For instance, the artifact was even more pronounced at modulation measurements with 1000 nm amplitude, where forces of more than 40 nN were reached during the modulation (see Figure 4 in Appendix E).

Ultimately, I detected that the discontinuous movement of the cantilever during the modulation segment was related to the z-closed loop. The z-closed loop corrects for nonlinearity and hysteresis of the piezo that controls the cantilever movement. The enabled z-closed loop led to complications during the establishment of AFM-based shear, and to keep all AFM experiments consistent, I initially decided for a disabled z-closed loop for all further experiments. However, I discovered that a disabled z-closed loop hinders a reliable modulation segment, whereas the activation of the z-closed loop made predictable modulations possible. Figure 3.13 a) shows a representative force-time curve of a modulation with 1000 nm amplitude at 1 Hz. The maximum force applied was constant at ca. 2 nN. Additionally, Figure 3.13 b) shows that the desired amplitude of 1000 nm was applied steadily.

Since larger setpoint forces can have an impact on cell detachment (e.g., detachment forces and energies) [205], a reference measurement that accounts for the additional force applied during the modulation was necessary. For this purpose, I implemented another approach segment in the force ramp designer that moved the cantilever the same distance towards the substrate as the value of modulation amplitude. I decided to keep the cantilever speed for the second approach at 5 µm/s. Hence, a holding

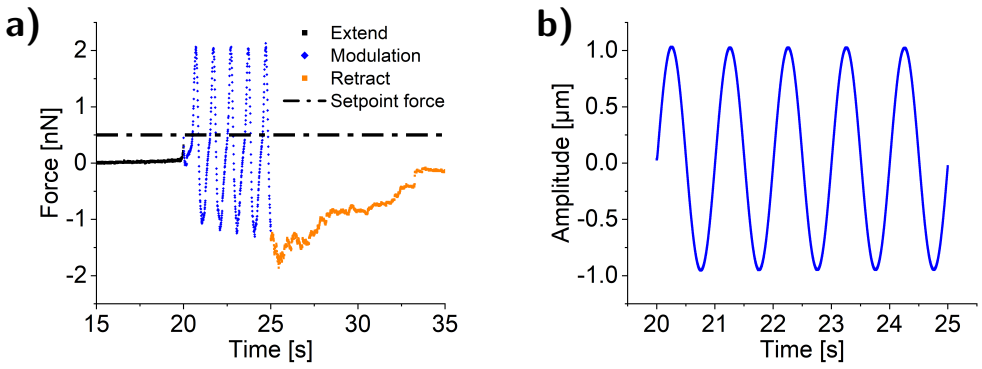

Figure 3.13: Activation of the z-closed loop enables a predictable modulation. a) The representative force-time curve shows a consistent force during the modulation segment (1000 nm amplitude, 1 Hz frequency, 5 periods). b) The illustration of the amplitude applied as a function of time shows a reliable application of the desired amplitude of 1000 nm. This verifies a reliable and predictable modulation if the z-closed loop was enabled.

segment was required to keep the cell-substrate contact constant at 5 s in total. For instance, reference measurements for a 1000 nm amplitude modulation applied an additional 1000 nm distance to the cell during the contact phase, followed by a 4.8 s holding segment to keep the overall contact time consistent with the modulation measurements. The examination of force-time curves revealed an initial force increase during the second approach (see Figure 6 in Appendix F). Since additional distance increases the force applied, this was partially expected. However, that the force maximum applied was larger than the forces applied during modulations was unexpected. Nevertheless, I decided for the exact additional distance and the constant cantilever speed to keep these experimental parameters consistent throughout the experiments.

3.4.4 Oscillatory Forces Affect the Initial Cell Adhesion of Fibroblast Cells

After the successful implementation of predictable modulation segments, a single fibroblast cell was attached to a functionalized cantilever and incubated for 15 min. Then, a first cycle of normal detachment (no modulation) and modulation measurements was conducted. At first, 20 force-distance curves were recorded without modulation with a setpoint force of 0.5 nN and 5 µm/s for the speed of the cantilever movement. Then, 20 force-distance curves were recorded with a modulation segment with amplitudes of 10-1000 nm and modulation frequencies of 1-10 Hz. After finishing this first cycle, the whole process was repeated for two further cycles. The cell-substrate contact time was kept at 5 s for all measurements. All force-distance curves recorded were analyzed for the detachment force, energy and the last rupture event including its force and position as well as length and slope of the plateau prior to the last rupture event.

The detachment energy (i.e., area under the retract curve of a force-distance curve) represents the energy that is necessary to completely detach a cell from the substrate, whereas the cell detachment force describes the force that is necessary to completely detach the cell from the substrate. Figure 3.14 shows the mean detachment forces for different modulation settings as a function of the modes (normal, modulation). Each symbol represents the mean value of up to 20 force-distance curves analyzed and the error bars indicate the standard deviations. Since the results of detachment energies show a trend similar to the detachment forces shown below, the results are shown in Figure 7 in Appendix F.

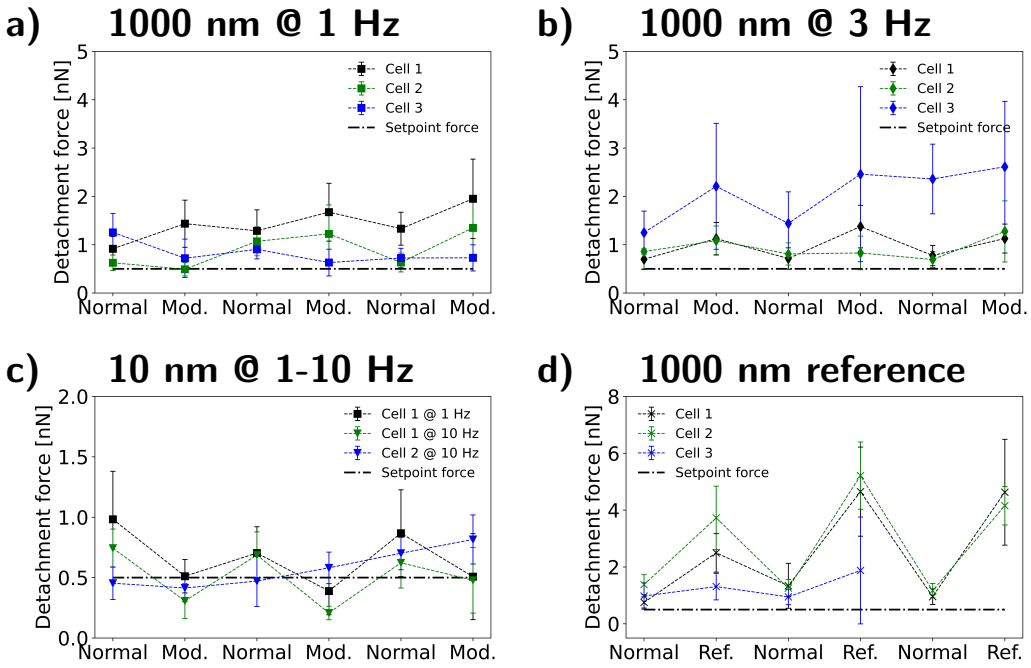

Figure 3.14: Mean detachment forces as a function of the modes applied. Each symbol shows the mean detachment force of up to 20 force-distance curves and the error bars denote the standard deviations. Modulations with an amplitude of 1000 nm and frequencies of a) 1 Hz and b) 3 Hz show increased detachment forces for the modulation mode compared to the normal mode. An overall positive impact of the modulation with 1000 nm was indicated through the increased detachment forces after the third cycle compared to the values from the first normal mode. c) Modulations with 10 nm amplitude may have a negative impact on detachment forces since the mean detachment forces for the modulation modes were lower than mean detachment forces determined from normal modes. However, it should be noted that the number of cells successfully measured was limited to three cells in total. d) Since a modulation with a certain amplitude applies additional force to the attached cell, which can affect the detachment forces determined, a reference measurement was necessary to verify the described observations. For this purpose, the modulation segment was exchanged with a second approach segment. Here, a reference measurement with 1000 nm additional distance shows distinctive increases in detachment forces for the reference modes in comparison to results of the corresponding normal measurements. The impact of the reference measurements was more pronounced than the impacts of 1000 nm modulations.

Modulations with an amplitude of 1000 nm and frequencies of 1 Hz (see Figure 3.14 a)) or 3 Hz (b)) resulted in increased detachment forces compared to normal measurements. Since an overall shift (i.e., comparison first normal to third modulation mode) towards larger detachment forces was visible for both modulation frequencies, enhanced cell detachment can be suggested. The results from modulations with a 10 nm amplitude, on the other hand, show that such modulations decrease the detachment forces (see Figure 3.14 c)). I assume that small modulation amplitudes had an adverse impact on cell detachment. It should be noted that only one cell was measured at 1 Hz and two cells at 10 Hz. However, all three cells show a similar trend for the mean detachment forces.

Since the force applied affects the detachment forces determined [205], a reference measurement was necessary to verify the observations. For this purpose, the modulation segment was exchanged with a segment to approach with a predefined distance (so-called reference mode, see further details in Section 3.4.3). Figure 3.14 d) shows the mean detachment forces for a reference measurement with 1000 nm additional distance. A prominent increase in detachment forces was detected for the reference mode in comparison to results of the normal measurements. The larger forces applied during reference measurements compared to modulation measurements may explain the larger increase in detachment forces. This is supported by the results of cell 3 of the reference measurement, where the forces applied were in a similar range during the reference measurement than forces applied during modulation measurements (1000 nm, 1 Hz) and the detachment forces determined showed similar increases as observed for modulation measurements.

The analysis of the last rupture event can provide insight into the characteristics of single bonds. This permits the correlation of changed detachment forces to single bond specifics. For this purpose, the last rupture event was analyzed for its step height (i.e., the force necessary to rupture the bond), its step position (i.e., the distance at which the bond ruptures) and the length and slope of the plateau region prior to the last rupture event. The results of last rupture force (Figure 8 a)-d)) and the plateau length (Figure 8 e)-h)) are shown in Appendix F. I suggest no distinctive difference between normal and modulation measurements as well as between different modulation settings.

Figure 3.15 shows the absolute frequency of step positions determined for 1000 nm modulation amplitudes at a) 1 Hz and b) 3 Hz as well as for c) 10 nm modulation amplitudes at 10 Hz and d) 1000 nm reference measurements. The step positions determined for normal (black) and modulation (turquoise) or reference (orange) measurements were combined for all cycles. The insets show the distributions of the step positions for normal (black) and modulation (turquoise) or reference (orange) measurements. The boxplots and significance levels follow the convention described in Appendix B.2.

Modulations with an amplitude of 1000 nm show a significant shift towards larger step positions for both modulation frequencies. Modulations with 10 nm and 10 Hz, on the other hand, show a shift towards lower step positions at a significance level of 0.05. Since the step position is a measure for the bond lifetime, larger values reflect an increased duration until full cell detachment. The observations about shifted

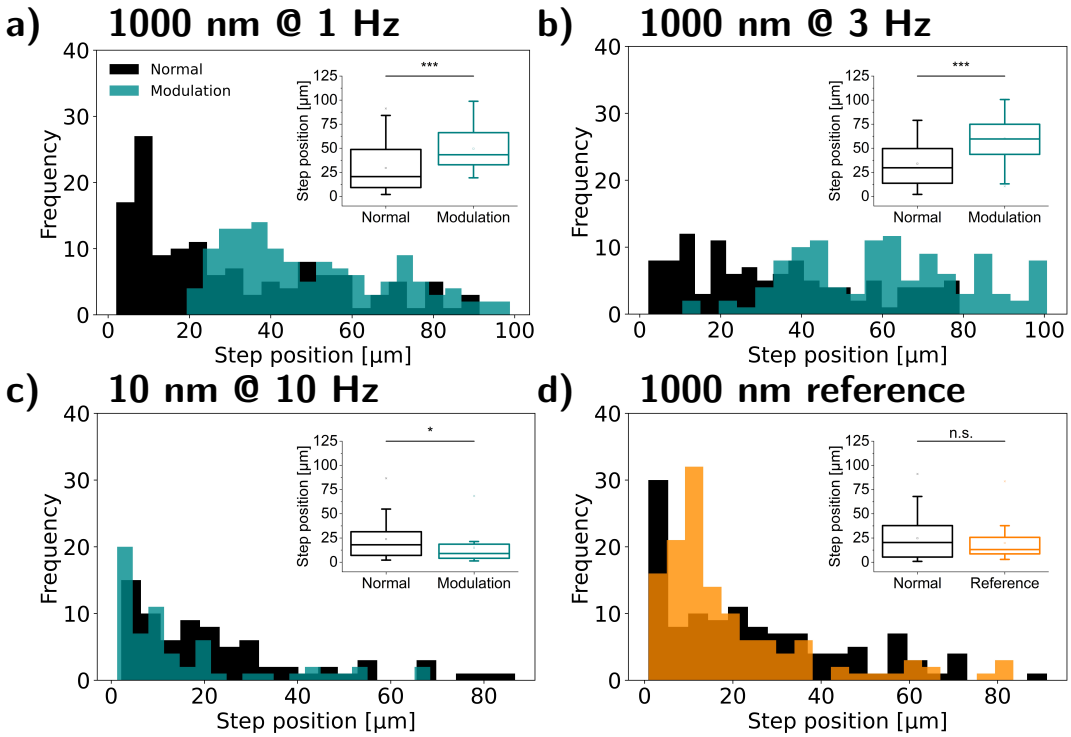

Figure 3.15: Probability distributions of the step positions. Each graph shows the frequency of all step positions determined for normal (black) and modulation (blue) or reference (orange) measurements. The insets show the distributions of step positions with significance levels of * $p < 0.05$ and ***$p < 0.001$ or no significant difference (n.s.) at $p < 0.05$. Modulations with an amplitude of 1000 nm and frequencies of a) 1 Hz and b) 3 Hz show a significant shift towards larger step positions. c) Modulations with 10 nm at 10 Hz (measurement of two cells) show a shift towards lower step positions (significance level of 0.05). d) Reference measurements with 1000 nm additional distance show no significant (n.s.) difference between normal and reference measurements. Hence, the modulation with 1000 nm amplitude has an impact on step position that was not observed for the reference measurements although a prominent increase of detachment forces was detected for both 1000 nm modulation and reference measurements. Additionally, the results of modulation measurements with 10 nm suggest an adverse impact on cell detachment.

step positions support the previous conclusions that modulations with 1000 nm amplitudes enhanced cell detachment, whereas modulations with small amplitudes impaired cell detachment. Additionally, reference measurements with 1000 nm additional distance show no significant (n.s.) difference between normal and reference measurements. Hence, the modulation with 1000 nm amplitude has an impact on step position that was not observed for the reference measurements although a prominent increase of detachment forces was detected for both 1000 nm modulation and reference measurements. It is conceivable that modulations with large amplitudes result in a modulation-dependent activation of the cell membrane and I conclude that increased cell detachment was related to a combination of additional force applied and a modulation with a defined frequency.

In addition to the last rupture characteristics, I analyzed the plateau region prior to the last rupture event (see Figure 8 e)-h)) in Appendix F). The slope of the plateau

region can provide insights into the receptor-cytoskeleton connection. A negative slope indicates a tight connection to the actin cytoskeleton, whereas a horizontal plateau (slope close to zero) indicates the extraction of membrane tethers, which impedes bond rupture. Figure 3.16 shows the probability densities of slopes of the plateau region determined as a function of step positions measured. Each symbol shows the plateau slope determined prior to a last rupture event correlated to its step position for normal (black squares), modulation (turquoise diamonds or light turquoise stars) and reference (orange upward-pointing triangles) measurements.

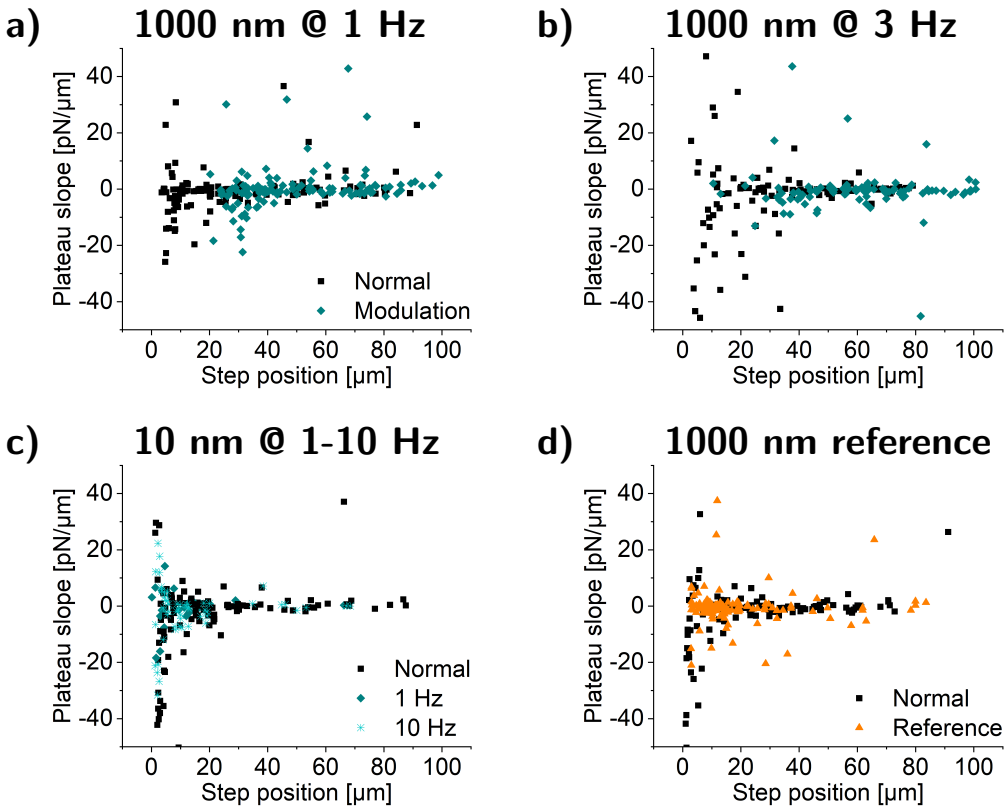

Figure 3.16: Probability density of slopes of the plateau region determined prior to the last rupture event as a function of step positions measured. Each symbol shows the plateau slope determined prior to a last rupture event correlated to its step position for normal (black squares), modulation (turquoise diamonds or light turquoise stars) and reference (orange upward-pointing triangles) measurements. a) Modulations with 1000 nm at 1 Hz showed a similar probability density compared to normal measurements but a shift towards larger step positions. Most plateau slopes were around zero, which indicates tether formation. Negative slopes were detected at lower positions for both normal and modulation measurements. b) Modulations with 1000 nm at 3 Hz reduced the occurrence of positive and negative slopes, which suggests increased tether formation. c) Modulations with 10 nm showed no distinctive difference to normal measurements for both frequencies. d) Reference measurements showed a slight reduction of negative slopes, which indicates reduced connection to the actin cytoskeleton.

Modulations with 1000 nm at 1 Hz showed a similar probability density compared to normal measurements but a shift towards larger step positions (see Figure 3.16 a)).

Most plateau slopes were around zero, which indicates tether formation. Negative slopes were detected at lower step positions for both normal and modulation measurements. Figure 3.16 b) shows the results of modulations with 1000 nm at 3 Hz. A modulation reduced the number of negative slopes, which suggests a higher rate of tether formation. For modulations with 10 nm, no distinctive difference to normal measurements was detected for both frequencies (see Figure 3.16 c)). Reference measurements seem to slightly reduce the connection to the actin cytoskeleton indicated by a reduction of negative slopes (see Figure 3.16 d)).

Since the reference measurements showed a similar or larger impact on detachment forces and energies than the modulation measurements, I propose a strong effect of the additional force applied to a cell. However, no significant impact of the reference measurement on step positions was detected, which indicates an underlying mechanism that relies on the modulation amplitude and frequency. A frequency of 1 Hz is a physiological relevant stimulus [220] and it seems that a slightly larger frequency up to 3 Hz still has a positive impact on cell detachment. However, I suggest a slight decrease of connection to actin indicated by a reduction of negative plateau slopes for 3 Hz modulations compared to 1 Hz modulations. The combination of a small modulation amplitude and a large modulation frequency, on the other hand, damaged the cells measured and prevented a recovery during normal measurements. This agrees well with the work of Heitmann et al. which shows that certain amplitudes of a surface limit cell adhesion [169].

The underlying mechanism that induces increased cell detachment upon modulation might include integrins that act as catch bonds or other proteins integrated in the adhesion cluster (e.g., talin or vinculin) [217]. Talin unfolding is known to open up additional binding sites that can stabilize cell adhesion and can favor a growth of focal adhesions [12], [47], [50]. Also, modulation of a cell may start an internal cell reaction to start allosteric regulations [46] or the cell membrane might be activated through the modulation that may lead to integrin recruitment [20]. In addition, mechanosensitive ion channels could play a significant role in explaining the observations. For instance, Piezo1 opens upon cell indentation [51]. I propose that the modulation presented here can trigger the opening of ion channels to adapt cell detachment. Still, a combination of the abovementioned explanations is plausible.

3.4.5 Adjustment of the Manipulation System Presented to Investigate Mechanosensitive Ion Channels

Since mechanosensitive ion channels, such as Piezo1, are a relevant candidate to explain the impact of modulation measurements on cell detachment, the next step towards a comprehensive study of modulation measurements, was the investigation of the aforementioned ion channel. Piezo1 plays an essential role in cancer formation and metastatic behavior [65] and is important in inflammatory processes of the immune system [66]. Modified human embryonic kidney cells (HEK293T, provided by my collaboration partner Dr. Kate Poole) were used in the described experimental setup. To interpret results with regard to Piezo1, two cell types were measured: one with Piezo1 to investigate the role of the ion channel (so-called “Piezo1”) and

one without Piezo1 (so-called "control") as a base level for the modulation measurements.

The established system to measure and modulate fibroblast cells employed a contact time of 5 s. The same contact time resulted in successful measurements of the control line. However, initial measurements of Piezo1 cells revealed incomplete cell detachment within the available 100 µm range of the AFM setup. Since the available time during cell-substrate contact (i.e., contact time) has an impact on the cell detachment [8], [109], a reduction of the contact time was necessary to achieve full cell detachment. The maximum meaningful modulation frequency was 2 Hz as higher frequencies may prevent a relaxation of the Piezo1 channel (reaction time of Piezo1 is on a millisecond timescale [61]).

Modulations with 10 nm amplitudes affected the detachment of fibroblast cells little and/or adversely. Initial measurements of HEK293T cells supported these findings. Hence, modulation amplitudes of 1000 nm were chosen for further measurements of HEK293T cells.

3.4.6 Preliminary Manipulation Measurements Indicate the Importance of Piezo1

After the successful adjustment of the experimental setup, single HEK293T cells were measured through three cycles of normal and modulation or reference modes. The procedure was the same as previously described (see Section 3.4.4). Briefly, one cycle consisted of 20 normal force-distance curves and 20 manipulated (either modulation or reference) force-distance curves. The experimental details were 0.5 nN setpoint force, 5 µm/s as cantilever speed, 3 s contact time and modulation settings of 1000 nm at 2 Hz. The force-distance curves recorded were analyzed for the detachment force, detachment energy, last rupture force and step position as well as length and slope of the plateau region prior to the last rupture event. Figure 3.17 shows the distributions of detachment forces for single cell measurements with the convention described in Appendix B.2. Normal measurements are labeled with black, modulation measurements are labeled in blue colors (light blue: Control cell, dark blue: Piezo1 cell) and reference measurements are labeled in orange colors (light orange: Control cell, orange: Piezo1 cell).

The distributions and mean values of the detachment force showed no distinctive differences or any trend throughout the cycles for the control cell (see Figure 3.17 a)). Modulations of the Piezo1 cell resulted in a slight increase of mean detachment forces compared to detachment forces of normal measurements and a slight overall increase of detachment forces can be speculated (see Figure 3.17 b)). Reference measurements for both the control and Piezo1 cell showed pronounced increases of mean values and distributions of detachment forces. However, the reference measurements showed a reversible effect on the detachment forces determined (i.e., values for normal measurements stayed on the same base level). Additionally, the reference measurement of the Piezo1 cell indicated an overall positive impact on the cell detachment. Still, it is important to note that these graphs show only results

from measurements of single cells and cell variability exists that may affect the outcome and observations of the measurements. The results of detachment energies fit well with the abovementioned observations of detachment forces (see Figure 9 in Appendix G).

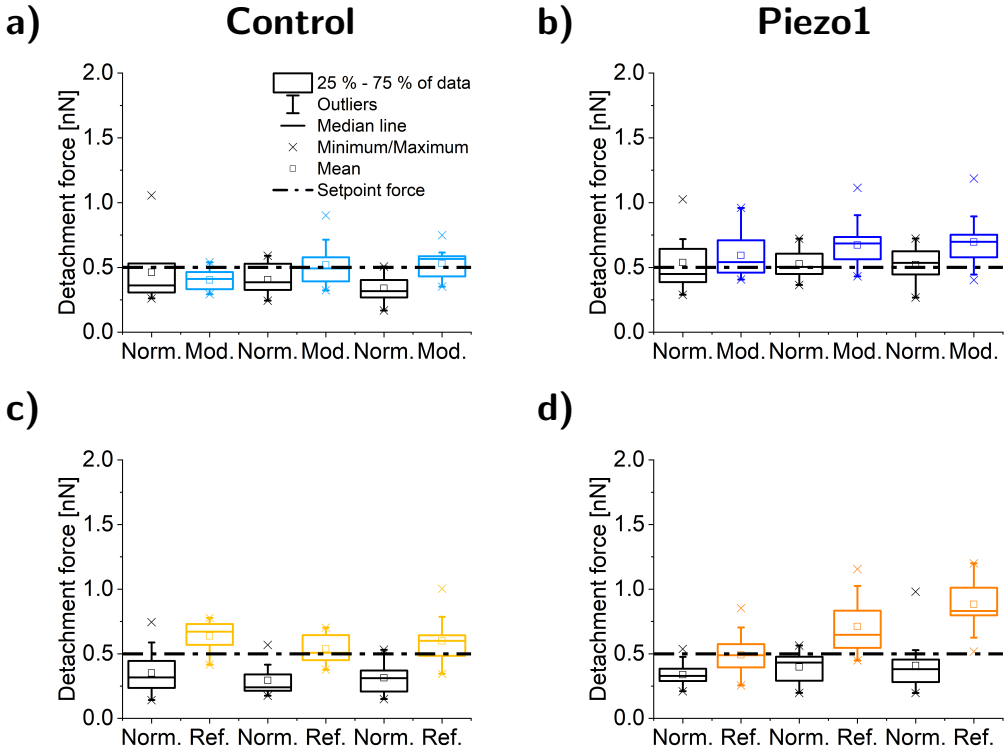

Figure 3.17: Distributions of detachment forces as a function of the modes applied. Each graph shows the results of a single cell measurement. Normal measurements are labeled with black, modulation measurements are labeled in blue colors (light blue: Control cell, dark blue: Piezo1 cell) and reference measurements are labeled in orange colors (light orange: Control cell, orange: Piezo1 cell). a) Modulations of a control cell showed no distinctive difference or trend throughout the cycles. b) Modulations of a Piezo1 cell showed a slight increase of mean values of detachment forces compared to detachment forces of normal measurements. Additionally, a slight overall increase of detachment forces during modulations was visible. c) Reference measurements of a control cell showed a reversible prominent increase of mean detachment forces. A clear difference between the distributions of normal and reference measurements was visible. d) Reference measurements of a Piezo1 cell showed a striking increase of mean detachment forces compared to detachment forces of normal measurements. In addition, an overall increase of the distributions during reference modes was detected. These observations suggest a slight impact of modulations on Piezo1 cells and a distinctive impact of additional distance (i.e., force) on control and Piezo1 cells. Additionally, reference measurements may affect Piezo1 cells persistently. It is important to note that further measurements are required to verify these observations.

Figure 3.18 shows the plateau slopes determined as a function of step positions combined for all cycles of the single cell measurements. Each symbol shows the plateau slope determined prior to a last rupture event correlated to its step position.

Normal measurements are displayed by black squares, modulation measurements are displayed by light blue (control) or dark blue (Piezo1) diamonds, whereas reference measurements are indicated by light orange (control) or orange (Piezo1) upward-pointing triangles.

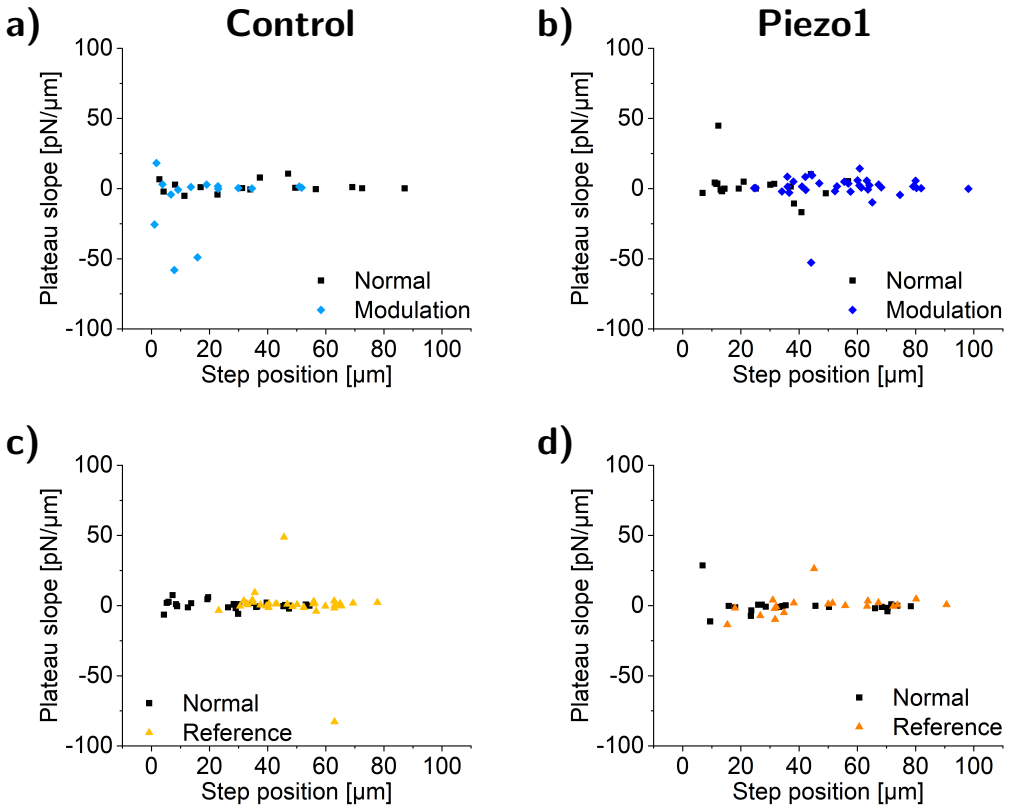

Figure 3.18: Probability density of slopes of the plateau region determined prior to the last rupture event as a function of step positions measured. Each symbol shows the plateau slope determined prior to a last rupture event correlated to its step position for normal (black squares), modulation (light blue diamonds for the control cell or dark blue diamonds for the Piezo1 cell) and reference (light orange upward-pointing triangles for the control cell or orange upward-pointing triangles for the Piezo1 cell) measurements. The majority of plateau slopes determined was approximately zero, which indicates tether formations. a) Modulations of a control cell showed a similar probability density compared to normal measurements. Still, a slight decrease of step positions was determined at a significance of 0.05 (see Figure 10 a) in Appendix G). b) Modulations of a Piezo1 cell shifted the probability density towards larger step positions. c) Reference measurements of a control cell shifted the probability density towards larger step positions similar to modulations of a Piezo1 cell. Both shifts towards larger step positions showed a significance level of 0.001 (see Figure 10 b) and c) in Appendix G). d) Reference measurements of a Piezo1 cell showed no prominent difference to normal measurements (see Figure 10 d) in Appendix G). These observations suggest that the impact of the modulation is specific for the Piezo1. However, the reference measurement enables the induction of a similar impact for the control cell.

Modulations of a control cell showed no distinctive impact on the probability density compared to normal measurements (see Figure 3.18 a)). However, a slight decrease of step positions was determined at a significance of 0.05 (see Figure 10 a) in Appendix G). Modulations of a Piezo1 cell shifted the probability density towards larger step positions (see Figure 3.18 b)). Reference measurements of a control cell shifted the probability density towards larger step positions similar to modulations of a Piezo1 cell. Both shifts towards larger step positions showed a significance level of 0.001 (see Figure 10 b) and c) in Appendix G). Reference measurements of a Piezo1 cell showed no significant difference to normal measurements (see Figure 10 d) in Appendix G). These observations suggest that the impact of the modulation is specific for the Piezo1. However, the reference measurement showed a similar impact for the control cell. The last rupture forces showed no clear variations, except for the modulated Piezo1 cell (see Figure 11 a)-d) in Appendix G). I propose a slight decrease of the last rupture forces due to modulations. The plateau lengths determined showed slight variations between cell type and/or throughout the measurement cycles, but it was not possible to suggest a clear trend of the parameter (see Figure 11 e)-h) in Appendix G).

Since these measurements depict single cell measurements, the depth of interpretation is limited by cell variability. Still, the initial results indicate a difference between the control and the Piezo1 cell line. It seems that the modulation has no impact on the control line, whereas increases cell detachment if Piezo1 is present. A similar effect can be triggered by applying additional force to a control cell.

3.4.7 Conclusion

In the body, mechanical signals regulate cells and their behavior. For instance, blood pressure controls blood vessel wall stretching [12], certain blood flow patterns can promote atherosclerosis and thrombosis [193] or mechanical loads can adjust bone mass in bone tissue (e.g., bone mass formation upon continuous exercise) [213]. Understanding the diversity of cell responses to external cues is vital for medical purposes and will be beneficial for medical applications (e.g., tissue engineering, implant design) [163]. Yet, detailed understanding of the impact of oscillatory forces on initial cell adhesion of single cells and single bond strengths is lacking.

Here, I presented a system applying oscillatory forces to single cells attached to an AFM cantilever and a subsequent measurement of cell detachment. For this purpose, the cantilever was modulated with a defined modulation amplitude and frequency during cell-substrate contact. At first, I modulated fibroblast cells with amplitudes of 10 nm or 1000 nm and frequencies of 1-10 Hz. I showed that large amplitudes increase the cell detachment determined (force and energy) independent of the frequency applied, whereas modulations with small amplitudes of 10 nm seemed to be harmful since cell detachment decreased. Reference measurements that accounted for the additional force applied during the modulation phase also showed strongly increased cell detachment.

The last rupture event can provide information on single bond dynamics. I propose no distinctive difference between normal and modulation measurements and

between different modulation settings for the last rupture force and plateau length, whereas significant differences were observed for the step position (i.e., position at which the bond ruptures). Large modulation amplitudes significantly shifted the step positions determined to larger values, whereas small amplitudes slightly shifted the step positions towards lower values. This supports the suggestion that small amplitudes are harmful and/or exhausting for cells. Although reference measurements increased cell detachment, the step positions determined showed no significant difference between normal and reference measurements. This suggests an impact of the modulation on both whole cell detachment and single bonds, whereas additional forces applied affect only whole cell detachment. A correlation of step positions and plateau slopes showed that a 1000 nm amplitude at 3 Hz reduced the number of negative slopes, which indicates increased tether formation. This was detected for reference measurements as well but much less pronounced, which indicates a combined effect of modulation and additional force applied for plateau slopes.

From these results, I propose a strong effect of additional force applied to a cell. Since no significant impact of the reference measurement on step positions was detected, I conclude that an underlying mechanism exists that relies on the modulation amplitude and frequency. Plausible candidates include integrins acting as catch bonds, other proteins of the adhesion complex like talin or vinculin and/or mechanosensitive ion channels. In addition, the modulation may activate the cell membrane leading to integrin recruitment, which can also impede cell detachment.

Since mechanosensitive ion channels, such as Piezo1, are highly relevant to ensure a comprehensive study of the impact of the modulation system presented, the experimental parameters were modified permitting the investigation of the impact of modulations on modified human embryonic kidney cells (HEK293T). HEK293T cells with the mechanosensitive ion channel Piezo1 and HEK293T without Piezo1 as control were modulated with 1000 nm amplitude at 2 Hz. Initial results showed no impact of the modulation on the control cell but slightly increased cell detachment for a Piezo1 cell. However, the reference measurement of a control cell showed a distinctive impact of additional force on cell detachment, which was also observed for a Piezo1 cell. In addition, an overall increase of cell detachment was visible for the Piezo1 cell, which was not detected for the control cell. As these were only single cell measurements and cell variability can have a significant impact, these observations are stated with caution. Correlations of step positions and plateau slopes showed a majority of tethers (i.e., zero slopes). Modulations of the Piezo1 cell or reference measurements of the control cell shifted the values of step positions towards larger values compared to normal measurements. This suggests that the modulation is specific for Piezo1 cells, while reference measurements (i.e., additional force applied) may have a similar impact as Piezo1 modulation measurements, also for control cells.

For future measurements, I recommend using staining techniques to visualize adhesion proteins or the actin cytoskeleton to investigate their role in the modulation experiments presented. Alternatively, the use of chemicals that block the actin cytoskeleton would be beneficial for a comprehensive study. For instance, the inhibitor cyto-D can disrupt actin polymerization and can eliminate stress fibers [213]. An-

other possible chemical is blebbistatin, which affects cell contractility due to inhibition of non-muscle myosin II [213]. The combination of the AFM-based modulation system presented with imaging of Ca^{2+} flickers as described by Pathak et al. and/or Ellefsen et al. could allow a precise correlation of Piezo1 activity and cell detachment [40], [221]. Also, the investigation of the exact contact area via total internal reflection fluorescence microscopy would allow a more detailed understanding of mechanotransduction.

Ultimately, a comprehensive study of the impact of modulations with different amplitudes and frequencies will help in treating diseases and developing new implant materials. A promising strategy would be to waken cancer dormancy and a consecutive targeted treatment of cancer cells to improve cancer treatment.

Chapter 4

Conclusion

In the first part of my thesis, I described how conventional AFM-based microindentation lacks consistency and comparability. However, mechanotransduction studies depend not only on producing materials with defined material properties but moreover on reliable and feasible techniques for quantitatively measuring properties of a given material. I demonstrated a new and versatile strategy towards reliable AFM-based microindentation measurements of soft materials by developing a MATLAB algorithm that iteratively fits the Hertz model to indentation data. By this means, a value for the Young's modulus with minimized fitting error is automatically detected in a region where it is independent of the indentation depth. This ensures a quantitative and reproducible determination of Young's moduli, even for huge data sets. In a second step, I demonstrated the impact of various experimental parameters on the outcome of AFM-based microindentations. This proved both the necessity and applicability of our newly developed algorithm. I proposed a detailed strategy for implementing microindentation measurements of a given material. In addition, I showed that our algorithm is capable of recording elasticity maps and allows the determination of Young's moduli on a spatial scale similar to cell interactions. This will permit a more comprehensive study of elastic properties of soft biomaterials that also includes material inhomogeneity at the nano- and/or microscale.

In the second part of my thesis, I followed three approaches to affect cells and their behavior: To begin with, I investigated the impact of layer thickness on cell morphology. In a second approach, I adapted our existing AFM towards a unique AFM-based shear system and finally, I established an AFM-based modulation system for applying oscillatory forces to single cells.

Based on previous research, I designed an experimental setup to investigate the impact of layer thickness on cell morphology. I showed that cell circularity in addition to the cell spreading area usually used is a crucial cell parameter to describe alterations of cell behavior. I propose that a layer thickness sensing threshold of fibroblast cells exists independent of the substrate stiffness used, whereas fibrosarcoma cells showed no clear trend for a thickness sensing threshold. This emphasizes the need for investigating cell behavior correlated to the *in vivo* situation and/or possible application fields. A further study could focus on investigating the thickness sensing threshold of healthy brain cells to aid developing implant coatings that match the

natural elasticity of brain tissue and reduce the risk of implant complications, such as scar formations that alter signal transduction. The correlation of traction forces to the thickness sensing threshold will enable a more comprehensive understanding of mechanotransduction and may pave the way towards novel applications fields (e.g., smart brain-computer interfaces [222]).

AFM single cell force spectroscopy is a versatile tool for analyzing initial cell adhesion and single bond ruptures under physiological conditions. I enabled stage movement during cell-substrate contact permitting the application of defined shear to a single cell that is attached to the cantilever. I showed how different shear distances affected both whole cell detachment and single bond ruptures of fibroblast cells. To my knowledge, such a shear system is unique and can easily be adjusted for investigating other cell types. More comprehensive understanding of how shear impacts cells is of medical interest. For instance, vascular functionality highly depends on normal shear conditions. In addition to a setup applying unidirectional shear, I installed a high precision stage to establish bidirectional shear measurements. In the future, this setup will allow correlating the influences of varying shear distances applied at different frequencies on whole cell detachment and single bond ruptures. Thus, having a broad scope for medical applications, such as treatment of atherosclerosis and development of new implant materials and/or designs, and/or for fundamental research building an overarching understanding of mechanotransduction.

In a final step of my thesis, I followed an approach to apply oscillatory pushing and pulling on the microscale. Such oscillatory mechanical loading is essential in many parts of our body. For instance, our body adjusts bone mass according to the level of loading experienced. I developed an AFM-based modulation system that facilitates cantilever oscillation with controlled amplitudes at defined frequencies during cell-substrate contact and a subsequent measurement of whole cell detachment. Although, reference measurements that accounted for additional force applied during the modulation showed similar, positive effects to whole cell detachment, I revealed that shifts of the positions at which the last rupture event occurs were solely affected by modulation measurements with large amplitudes. This suggests an inherent mechanism that rather stems from the oscillatory stimulus than the pushing forces alone. In addition to integrins, mechanosensitive ion channels, such as Piezo1, are a great candidate to explain this inherent mechanism. Hence, I adjusted the experimental setup to apply AFM-based modulations to modified human embryonic kidney cells with and without Piezo1. Preliminary results supported the idea that Piezo1 is crucial for the inherent mechanism of detecting the modulation applied. The modulation system presented offers a great strategy to investigate mechanotransduction, which will help treating diseases and developing new implant materials and/or designs that precisely match the *in vivo* situation.

The studies shown in this thesis can be another step towards new and smart application fields. In the future, it might be realistic to ensure cell adhesion on demand through a smart implant device stimulating cells in specific and controlled situations.

Bibliography

[1] K. Munk, C. Abröll, T. Kurth, *et al.*, *Taschenlehrbuch Biologie: Biochemie - Zellbiologie*. Georg Thieme Verlag, 2008, ISBN: 978-3-13-144831-6.

[2] B. Alberts, D. Bray, K. Hopkin, *et al.*, *Essential Cell Biology*, 3rd ed. Garland Science, 2010, ISBN: 978-0-8153-4129-1.

[3] M. Benoit and C. Selhuber-Unkel, "Measuring Cell Adhesion Forces: Theory and Principles," in *Methods Mol. Biol.* Vol. 736, 2011, ch. 21, pp. 355–377, ISBN: 978-1-61779-105-5. DOI: 10.1007/978-1-61779-105-5_21.

[4] M. Benoit, "Force Spectroscopy on Cells," in *Handb. Nanophysics Nanomed. Nanorobotics*, 2011, ch. 9, pp. 1–29, ISBN: 978-1-4200-7546-5.

[5] M. S. Almén, K. J. Nordström, R. Fredriksson, and H. B. Schiöth, "Mapping the human membrane proteome: A majority of the human membrane proteins can be classified according to function and evolutionary origin," *BMC Biol.*, vol. 7, 2009. DOI: 10.1186/1741-7007-7-50.

[6] C. Chothia and E. Y. Jones, "The molecular structure of cell adhesion molecules," *Annu. Rev. Biochem.*, vol. 66, pp. 823–862, 1997. DOI: 10.1146/annurev.biochem.66.1.823.

[7] B. Ladoux and A. Nicolas, "Physically based principles of cell adhesion mechanosensitivity in tissues," *Reports Prog. Phys.*, vol. 75, no. 11, 2012. DOI: 10.1088/0034-4885/75/11/116601.

[8] A. A. Khalili and M. R. Ahmad, "A Review of Cell Adhesion Studies for Biomedical and Biological Applications," *Int. J. Mol. Sci.*, vol. 16, no. 8, pp. 18 149–18 184, 2015. DOI: 10.3390/ijms160818149.

[9] K. A. Jansen, D. M. Donato, H. E. Balcioglu, T. Schmidt, E. H. J. Danen, and G. H. Koenderink, "A guide to mechanobiology: Where biology and physics meet," *Biochim. Biophys. Acta*, vol. 1853, no. 11 Pt B, pp. 3043–3052, 2015. DOI: 10.1016/j.bbamcr.2015.05.007.

[10] F. Martino, A. R. Perestrelo, V. Vinarský, S. Pagliari, and G. Forte, "Cellular Mechanotransduction: From Tension to Function," *Front. Physiol.*, vol. 9, pp. 1–21, 2018. DOI: 10.3389/fphys.2018.00824.

[11] D. E. Discher, P. Janmey, and Y.-L. Wang, "Tissue Cells Feel and Respond to the Stiffness of Their Substrate," *Science*, vol. 310, no. 5751, pp. 1139–1143, 2005. DOI: 10.1126/science.1116995.

[12] J. L. Alonso and W. H. Goldmann, "Cellular mechanotransduction," *AIMS Biophys.*, vol. 3, no. 1, pp. 50–62, 2016. DOI: 10.3934/biophy.2016.1.50.

[13] T. Okegawa, R.-C. Pong, Y. Li, and J.-T. Hsieh, "The role of cell adhesion molecule in cancer progression and its application in cancer therapy," *Acta Biochim. Pol.*, vol. 51, no. 2, pp. 445–457, 2004. DOI: 10.18388/abp.2004_3583.

[14] M. Arnold, V. C. Hirschfeld-Warneken, T. Lohmüller, *et al.*, "Induction of Cell Polarization and Migration by a Gradient of Nanoscale Variations in Adhesive Ligand Spacing," *Nano Lett.*, vol. 8, no. 7, pp. 2063–2069, 2008. DOI: 10.1021/nl801483w.

[15] B. M. Gumbiner, "Cell Adhesion: The Molecular Basis of Tissue Architecture and Morphogenesis," *Cell*, vol. 84, no. 3, pp. 345–357, 1996. DOI: 10.1016/S0092-8674(00)81279-9.

[16] P. Martin, "Wound Healing - Aiming for Perfect Skin Regeneration," *Science*, vol. 276, no. 5309, pp. 75–81, 1997. DOI: 10.1126/science.276.5309.75.

[17] D. Wirtz, K. Konstantopoulos, and P. C. Searson, "The physics of cancer: The role of physical interactions and mechanical forces in metastasis," *Nat. Rev. Cancer*, vol. 11, no. 7, pp. 512–522, 2011. DOI: 10.1038/nrc3080.

[18] "Cell Adhesion and the Extracellular Matrix," in *Goodman's Med. Cell Biol.* 4th ed., Academic Press, 2021, ch. 7, pp. 203–247, ISBN: 978-0-12-817927-7. DOI: 10.1016/b978-0-12-817927-7.00007-7.

[19] J. L. Morrison, R. Breitling, D. J. Higham, and D. R. Gilbert, "A lock-and-key model for protein-protein interactions," *Bioinformatics*, vol. 22, no. 16, pp. 2012–2019, 2006. DOI: 10.1093/bioinformatics/btl338.

[20] V. Vogel and M. Sheetz, "Local force and geometry sensing regulate cell functions," *Nat. Rev. Mol. Cell Biol.*, vol. 7, no. April, pp. 265–275, 2006. DOI: 10.1038/nrm1890.

[21] J. M. Maloney, E. B. Walton, C. M. Bruce, and K. J. Van Vliet, "Influence of finite thickness and stiffness on cellular adhesion-induced deformation of compliant substrata," *Phys. Rev. E*, vol. 78, no. 4, pp. 1–15, 2008. DOI: 10.1103/PhysRevE.78.041923.

[22] L. F. Kadem, "Nanostructured and Photoswitchable Biointerfaces for Controlling Cell Adhesion," Ph.D. dissertation, Christian-Albrechts-Universität zu Kiel, 2016.

[23] Y. Alapan, J. A. Little, and U. A. Gurkan, "Heterogeneous Red Blood Cell Adhesion and Deformability in Sickle Cell Disease," *Sci. Rep.*, vol. 4, pp. 1–8, 2014. DOI: 10.1038/srep07173.

[24] S. Noria, D. B. Cowan, A. I. Gotlieb, and B. L. Langille, "Transient and Steady-State Effects of Shear Stress on Endothelial Cell Adherens Junctions," *Circ. Res.*, vol. 85, no. 6, pp. 504–514, 1999. DOI: 10.1161/01.res.85.6.504.

[25] W. A. Loesberg, X. F. Walboomers, J. J. W. A. Van Loon, and J. A. Jansen, "The effect of combined cyclic mechanical stretching and microgrooved surface topography on the behavior of fibroblasts," *J. Biomed. Mater. Res. Part A*, vol. 75A, no. 3, 2005. DOI: 10.1002/jbm.a.30480.

[26] S. Huth, "Force Measurement Assays and Materials for the Quantification of Cell Behavior," Ph.D. dissertation, Christian-Albrechts-Universität zu Kiel, 2020.

[27] N. Wang, J. D. Tytell, and D. E. Ingber, "Mechanotransduction at a distance: mechanically coupling the extracellular matrix with the nucleus," *Nat. Rev. Mol. Cell Biol.*, vol. 10, no. 1, pp. 75–82, 2009. DOI: https://doi.org/10.1038/nrm2594.

[28] J. M. Goffin, P. Pittet, G. Csucs, J. W. Lussi, J.-J. Meister, and B. Hinz, "Focal adhesion size controls tension-dependent recruitment of α-smooth muscle actin to stress fibers," *J. Cell Biol.*, vol. 172, no. 2, pp. 259–268, 2006. DOI: 10.1083/jcb.200506179.

[29] D. Riveline, E. Zamir, N. Q. Balaban, *et al.*, "Focal Contacts as Mechanosensors: Externally Applied Local Mechanical Force Induces Growth of Focal Contacts by an mDia1-dependent and ROCK-independent Mechanism," *J. Cell Biol.*, vol. 153, no. 6, pp. 1175–1185, 2001. DOI: 10.1083/jcb.153.6.1175.

[30] B. Geiger and A. Bershadsky, "Exploring the Neighborhood: Adhesion-Coupled Cell Mechanosensors," *Cell*, vol. 110, no. 2, pp. 139–142, 2002. DOI: 10.1016/S0092-8674(02)00831-0.

[31] R. Tapia-Rojo, Á. Alonso-Caballero, and J. M. Fernández, "Talin folding as the tuning fork of cellular mechanotransduction," *Proc. Natl. Acad. Sci. U. S. A.*, vol. 117, no. 35, pp. 21 346–21 353, 2020. DOI: 10.1073/pnas.2004091117.

[32] J. M. Barnes, L. Przybyla, and V. M. Weaver, "Tissue mechanics regulate brain development, homeostasis and disease," *J. Cell Sci.*, vol. 130, no. 1, pp. 71–82, 2017. DOI: 10.1242/jcs.191742.

[33] W. Platzer, *Color Atlas of Human Anatomy: Locomotor system*, 6th ed. Thieme Verlag, 2009, ISBN: 9783135333069.

[34] C. G. Rolli, H. Nakayama, K. Yamaguchi, J. P. Spatz, R. Kemkemer, and J. Nakanishi, "Switchable adhesive substrates: Revealing geometry dependence in collective cell behavior," *Biomaterials*, vol. 33, no. 8, pp. 2409–2418, 2012. DOI: 10.1016/j.biomaterials.2011.12.012.

[35] E. K. Paluch, C. M. Nelson, N. Biais, *et al.*, "Mechanotransduction: Use the force(s)," *BMC Biol.*, vol. 13, no. 1, pp. 1–14, 2015. DOI: 10.1186/s12915-015-0150-4.

[36] C. Couzon, A. Duperray, and C. Verdier, "Critical stresses for cancer cell detachment in microchannels," *Eur. Biophys. J.*, vol. 38, no. 10, pp. 1035–1047, 2009. DOI: 10.1007/s00249-009-0506-1.

[37] M. Cecelja and P. Chowienczyk, "Role of arterial stiffness in cardiovascular disease," *J. R. Soc. Med. Cardiovasc. Dis.*, vol. 1, no. 4, pp. 1–10, 2012. DOI: 10.1258/cvd.2012.012016.

[38] M. Ghibaudo, A. Saez, L. Trichet, *et al.*, "Traction forces and rigidity sensing regulate cell functions," *Soft Matter*, vol. 4, no. 9, pp. 1836–1843, 2008. DOI: 10.1039/b804103b.

[39] C. G. Galbraith and M. P. Sheetz, "A micromachined device provides a new bend on fibroblast traction forces," *Proc. Natl. Acad. Sci. U. S. A.*, vol. 94, no. 17, pp. 9114–9118, 1997. DOI: 10.1073/pnas.94.17.9114.

[40] K. L. Ellefsen, J. R. Holt, A. C. Chang, *et al.*, "Myosin-II mediated traction forces evoke localized Piezo1-dependent Ca2+ flickers," *Commun. Biol.*, vol. 2, no. 1, pp. 1–13, 2019. DOI: 10.1038/s42003-019-0514-3.

[41] J. Jiang, Z.-h. Zhang, X.-b. Yuan, and M.-m. Poo, "Spatiotemporal dynamics of traction forces show three contraction centers in migratory neurons," *J. Cell Biol.*, vol. 209, no. 5, pp. 759–774, 2015. DOI: 10.1083/jcb.201410068.

[42] B. Trappmann, J. E. Gautrot, J. T. Connelly, *et al.*, "Extracellular-matrix tethering regulates stem-cell fate," *Nat. Mater.*, vol. 11, no. 7, pp. 642–649, 2012. DOI: 10.1038/nmat3339.

[43] R. J. Pelham and Y. L. Wang, "Cell locomotion and focal adhesions are regulated by substrate flexibility," *Proc. Natl. Acad. Sci. U. S. A.*, vol. 94, no. 25, pp. 13 661–13 665, 1997. DOI: 10.1073/pnas.94.25.13661.

[44] J. M. Charest, J. P. Califano, S. P. Carey, and C. A. Reinhart-King, "Fabrication of Substrates with Defined Mechanical Properties and Topographical Features for the Study of Cell Migration," *Macromol. Biosci.*, vol. 12, no. 1, pp. 12–20, 2012. DOI: 10.1002/mabi.201100264.

[45] S. Weis, T. T. Lee, A. del Campo, and A. J. García, "Dynamic cell-adhesive microenvironments and their effect on myogenic differentiation," *Acta Biomater.*, vol. 9, no. 9, pp. 8059–8066, 2013. DOI: 10.1016/j.actbio.2013.06.019.

[46] W. Thomas, M. Forero, O. Yakovenko, *et al.*, "Catch-Bond Model Derived from Allostery Explains Force-Activated Bacterial Adhesion," *Biophys. J.*, vol. 90, no. 3, pp. 753–764, 2006. DOI: 10.1529/biophysj.105.066548.

[47] A. del Rio, R. Perez-Jimenez, R. Liu, P. Roca-Cusachs, J. M. Fernandez, and M. P. Sheetz, "Stretching Single Talin Rod Molecules Activates Vinculin Binding," *Science*, vol. 323, no. 5914, pp. 638–641, 2009. DOI: 10.1126/science.1162912.

[48] B. T. Marshall, M. Long, J. W. Piper, T. Yago, R. P. McEver, and C. Zhu, "Direct observation of catch bonds involving cell-adhesion molecules," *Nature*, vol. 423, pp. 190–193, 2003. DOI: 10.1038/nature01605.

[49] D. A. Calderwood, "Integrin activation," *J. Cell Sci.*, vol. 117, no. 5, pp. 657–666, 2004. DOI: 10.1242/jcs.01014.

[50] A. Wagoner Johnson and B. A. Harley, *Mechanobiology of Cell-Cell and Cell-Matrix Interactions*. Springer New York Dordrecht Heidelberg London, 2011, ISBN: 978-1-4419-8082-3. DOI: 10.1007/978-1-4419-8083-0.

[51] M. R. Servin-Vences, M. Moroni, G. R. Lewin, and K. Poole, "Direct measurement of TRPV4 and PIEZO1 activity reveals multiple mechanotransduction pathways in chondrocytes," *Elife*, vol. 6, pp. 1–24, 2017. DOI: 10.7554/eLife.21074.

[52] A. Kaminski, G. R. Fedorchak, and J. Lammerding, "The Cellular Mastermind(?) - Mechanotransduction and the Nucleus," in *Prog. Mol. Biol. Transl. Sci.* 1st ed., vol. 126, 2014, pp. 157–203, ISBN: 978-0-12-394624-9. DOI: 10.1016/B978-0-12-394624-9.00007-5.

[53] A. Banno and M. H. Ginsberg, "Integrin activation," *Biochem. Soc. Trans.*, vol. 36, no. Pt 2, pp. 229–234, 2008. DOI: 10.1042/BST0360229.

[54] B. Martinac and C. Cox, "Mechanosensory Transduction: Focus on Ion Channels," in *Ref. Modul. Life Sci.* 2017, pp. 1–47, ISBN: 978-0-12-809633-8. DOI: 10.1016/b978-0-12-809633-8.08094-8.

[55] K. Poole, R. Herget, L. Lapatsina, H.-D. Ngo, and G. R. Lewin, "Tuning Piezo ion channels to detect molecular-scale movements relevant for fine touch," *Nat. Commun.*, vol. 5, 2014. DOI: 10.1038/ncomms4520.

[56] S. S. Ranade, Z. Qiu, S.-H. Woo, *et al.*, "Piezo1, a mechanically activated ion channel, is required for vascular development in mice," *Proc. Natl. Acad. Sci. U. S. A.*, vol. 111, no. 28, pp. 10 347–10 352, 2014. DOI: 10.1073/pnas.1409233111.

[57] H. Ledford and E. Callaway, "Medicine Nobel for Duo Who Discovered Biology of Senses," *Nature*, vol. 598, p. 246, 2021. DOI: https://doi.org/10.1038/d41586-021-01283-6.

[58] P. A. Gottlieb, T. M. Suchyna, and F. Sachs, "Properties and Mechanism of the Mechanosensitive Ion Channel Inhibitor GsMTx4, a Therapeutic Peptide Derived from Tarantula Venom," in *Curr. Top. Membr.* Vol. 59, 2007, pp. 81–109, ISBN: 012153359X. DOI: 10.1016/S1063-5823(06)59004-0.

[59] H. Atcha, A. Jairaman, J. R. Holt, *et al.*, "Mechanically activated ion channel Piezo1 modulates macrophage polarization and stiffness sensing," *Nat. Commun.*, vol. 12, pp. 1–14, 2021. DOI: 10.1038/s41467-021-23482-5.

[60] A. Patkunarajah, J. H. Stear, M. Moroni, *et al.*, "TMEM87a/Elkin1, a component of a novel mechanoelectrical transduction pathway, modulates melanoma adhesion and migration," *Elife*, vol. 9, pp. 1–25, 2020. DOI: 10.7554/eLife.53308.

[61] D. De Vecchis, D. J. Beech, and A. C. Kalli, "Molecular dynamics simulations of Piezo1 channel opening by increases in membrane tension," *Biophys. J.*, vol. 120, no. 8, pp. 1510–1521, 2021. DOI: 10.1016/j.bpj.2021.02.006.

[62] J. M.-J. Romac, R. A. Shahid, S. M. Swain, S. R. Vigna, and R. A. Liddle, "Piezo1 is a mechanically activated ion channel and mediates pressure induced pancreatitis," *Nat. Commun.*, vol. 9, no. 1, pp. 1–10, 2018. DOI: 10.1038/s41467-018-04194-9.

[63] J. Ge, W. Li, Q. Zhao, *et al.*, "Architecture of the mammalian mechanosensitive Piezo1 channel," *Nature*, vol. 527, pp. 64–69, 2015. DOI: 10.1038/nature15247.

[64] J. Li, B. Hou, and D. J. Beech, "Endothelial Piezo1: Life depends on it," *Channels*, vol. 9, no. 1, pp. 1–2, 2015. DOI: 10.4161/19336950.2014.986623.

[65] Y. Sun, M. Li, G. Liu, *et al.*, "The function of Piezo1 in colon cancer metastasis and its potential regulatory mechanism," *J. Cancer Res. Clin. Oncol.*, vol. 146, no. 5, pp. 1139–1152, 2020. DOI: 10.1007/s00432-020-03179-w.

[66] A. G. Solis, P. Bielecki, H. R. Steach, *et al.*, "Mechanosensation of cyclical force by PIEZO1 is essential for innate immunity," *Nature*, vol. 573, pp. 69–74, 2019. DOI: 10.1038/s41586-019-1485-8.

[67] A. C. Newman, M. N. Nakatsu, W. Chou, P. D. Gershon, and C. C. Hughes, "The requirement for fibroblasts in angiogenesis: fibroblast-derived matrix proteins are essential for endothelial cell lumen formation," *Mol. Biol. Cell*, vol. 22, no. 20, pp. 3791–3800, 2011. DOI: 10.1091/mbc.E11-05-0393.

[68] I. R. Fernandes, F. B. Russo, G. C. Pignatari, *et al.*, "Fibroblast sources: Where can we get them?" *Cytotechnology*, vol. 68, pp. 223–228, 2016. DOI: 10.1007/s10616-014-9771-7.

[69] R. Lüllmann-Rauch, *Histologie*, 2. Auflage. Georg Thieme Verlag, 2006, ISBN: 978-3-13-129242-1.

[70] P. Meister, "Myofibroblasten Übersicht und Ausblick," *Pathologe*, vol. 19, pp. 189–193, 1998. DOI: https://doi.org/10.1007/s002920050272.

[71] A. Merecz-Sadowska, P. Sitarek, E. Kucharska, *et al.*, "Antioxidant Properties of Plant-Derived Phenolic Compounds and Their Effect on Skin Fibroblast Cells," *Antioxidants*, vol. 10, no. 5, pp. 1–24, 2021. DOI: 10.3390/antiox10050726.

[72] J. Solon, I. Levental, K. Sengupta, P. C. Georges, and P. A. Janmey, "Fibroblast Adaptation and Stiffness Matching to Soft Elastic Substrates," *Biophys. J.*, vol. 93, no. 12, pp. 4453–4461, 2007. DOI: 10.1529/biophysj.106.101386.

[73] B. C. Isenberg, P. A. DiMilla, M. Walker, S. Kim, and J. Y. Wong, "Vascular Smooth Muscle Cell Durotaxis Depends on Substrate Stiffness Gradient Strength," *Biophys. J.*, vol. 97, no. 5, pp. 1313–1322, 2009. DOI: 10.1016/j.bpj.2009.06.021.

[74] J. Y. Wong, A. Velasco, P. Rajagopalan, and Q. Pham, "Directed Movement of Vascular Smooth Muscle Cells on Gradient-Compliant Hydrogels," *Langmuir*, vol. 19, no. 5, pp. 1908–1913, 2003. DOI: 10.1021/la026403p.

[75] A. J. Engler, L. Richert, J. Y. Wong, C. Picart, and D. E. Discher, "Surface probe measurements of the elasticity of sectioned tissue, thin gels and polyelectrolyte multilayer films: correlations between substrate stiffness and cell adhesion," *Surf. Sci.*, vol. 570, no. 1-2, pp. 142–154, 2004. DOI: 10.1016/j.susc.2004.06.179.

[76] F. L. Graham, J. Smiley, W. C. Russell, and R. Nairn, "Characteristics of a Human Cell Line Transformed by DNA from Human Adenovirus Type 5," *J. Gen. Virol.*, vol. 36, no. 1, pp. 59–72, 1977. DOI: 10.1099/0022-1317-36-1-59.

[77] S. Dübel, F. Breitling, A. Frenzel, T. Jostock, and A. L. J. Marschall, *Rekombinante Antikörper*, 2.Auflage. Springer Spektrum, Berlin, Heidelberg, 2019, ISBN: 978-3-662-50275-4. DOI: https://doi.org/10.1007/978-3-662-50276-1.

[78] A. A. Stepanenko and V. V. Dmitrenko, "HEK293 in cell biology and cancer research: phenotype, karyotype, tumorigenicity, and stress-induced genome-phenotype evolution," *Gene*, vol. 569, no. 2, pp. 182–190, 2015. DOI: 10.1016/j.gene.2015.05.065.

[79] G. Shaw, S. Morse, M. Ararat, and F. L. Graham, "Preferential transformation of human neuronal cells by human adenovirus and the origin of HEK 293 cells," *FASEB Fed. Am. Soc. Exp. Biol.*, vol. 16, no. 8, pp. 869–871, 2002. DOI: 10.1096/fj.01.

[80] S. A. Campbell, J. Lin, E. Y. Dobrikova, and M. Gromeier, "Genetic Determinants of Cell Type-Specific Poliovirus Propagation in HEK 293 Cells," *J. Virol.*, vol. 79, no. 10, pp. 6281–6290, 2005. DOI: 10.1128/jvi.79.10.6281-6290.2005.

[81] S. N. Madhusudana, S. Sundaramoorthy, and P. T. Ullas, "Utility of human embryonic kidney cell line HEK-293 for rapid isolation of fixed and street rabies viruses: comparison with Neuro-2a and BHK-21 cell lines," *Int. J. Infect. Dis.*, vol. 14, no. 12, e1067–e1071, 2010. DOI: 10.1016/j.ijid.2010.07.004.

[82] I. Kovesdi and S. J. Hedley, "Adenoviral Producer Cells," *Viruses*, vol. 2, no. 8, pp. 1681–1703, 2010. DOI: 10.3390/v2081681.

[83] Y. L. Wang and R. J. Pelham, "[39] Preparation of a Flexible, Porous Polyacrylamide Substrate for Mechanical Studies of Cultured Cells," *Methods Enzymol.*, vol. 298, pp. 489–496, 1998. DOI: 10.1016/S0076-6879(98)98041-7.

[84] N. Guz, M. Dokukin, V. Kalaparthi, and I. Sokolov, "If Cell Mechanics Can Be Described by Elastic Modulus: Study of Different Models and Probes Used in Indentation Experiments," *Biophys. J.*, vol. 107, no. 3, pp. 564–575, 2014. DOI: 10.1016/j.bpj.2014.06.033.

[85] J. R. Tse and A. J. Engler, "Stiffness Gradients Mimicking In Vivo Tissue Variation Regulate Mesenchymal Stem Cell Fate," *PLoS One*, vol. 6, no. 1, e15978, 2011. DOI: 10.1371/journal.pone.0015978.

[86] W. J. Hadden, J. L. Young, A. W. Holle, *et al.*, "Stem cell migration and mechanotransduction on linear stiffness gradient hydrogels," *Proc. Natl. Acad. Sci. U. S. A.*, vol. 114, no. 22, pp. 5647–5652, 2017. DOI: 10.1073/pnas.1618239114.

[87] A. K. Denisin and B. L. Pruitt, "Tuning the Range of Polyacrylamide Gel Stiffness for Mechanobiology Applications," *ACS Appl. Mater. Interfaces*, vol. 8, no. 34, pp. 21 893–21 902, 2016. DOI: 10.1021/acsami.5b09344.

[88] A. J. Engler, S. Sen, H. L. Sweeney, and D. E. Discher, "Matrix Elasticity Directs Stem Cell Lineage Specification," *Cell*, vol. 126, no. 4, pp. 677–689, 2006. DOI: 10.1016/j.cell.2006.06.044.

[89] P. Moshayedi, G. Ng, J. C. F. Kwok, *et al.*, "The relationship between glial cell mechanosensitivity and foreign body reactions in the central nervous system," *Biomaterials*, vol. 35, no. 13, pp. 3919–3925, 2014. DOI: 10.1016/j.biomaterials.2014.01.038.

[90] C. E. Kandow, P. C. Georges, P. A. Janmey, and K. A. Beningo, "Polyacrylamide Hydrogels for Cell Mechanics: Steps Toward Optimization and Alternative Uses," in *Methods Cell Biol.* 07, vol. 83, 2007, ch. 2, pp. 29–46, ISBN: 978-0-12-370500-6. DOI: 10.1016/S0091-679X(07)83002-0.

[91] R. N. Palchesko, L. Zhang, Y. Sun, and A. W. Feinberg, "Development of Polydimethylsiloxane Substrates with Tunable Elastic Modulus to Study Cell Mechanobiology in Muscle and Nerve," *PLoS One*, vol. 7, no. 12, e51499, 2012. DOI: 10.1371/journal.pone.0051499.

[92] K. Siemsen, "Bio – Matrices Interaction from Microstructured Hydrogel Volumes and Hydrogel Surfaces Dissertation," Ph.D. dissertation, 2020.

[93] W. Shing, C. Yong, H. Yu, *et al.*, "Thickness sensing of hMSCs on collagen gel directs stem cell fate," *Biochem. Biophys. Res. Commun.*, vol. 401, no. 2, pp. 287–292, 2010. DOI: 10.1016/j.bbrc.2010.09.052.

[94] S. B. Gutekunst, K. Siemsen, S. Huth, *et al.*, "3D Hydrogels Containing Interconnected Microchannels of Subcellular Size for Capturing Human Pathogenic Acanthamoeba Castellanii," *ACS Biomater. Sci. Eng.*, vol. 5, no. 4, pp. 1784–1792, 2019. DOI: 10.1021/acsbiomaterials.8b01009.

[95] F. Di Benedetto, A. Biasco, D. Pisignano, and R. Cingolani, "Patterning polyacrylamide hydrogels by soft lithography," *Nanotechnology*, vol. 16, no. 5, S165–S170, 2005. DOI: 10.1088/0957-4484/16/5/006.

[96] J. R. Tse and A. J. Engler, "Preparation of Hydrogel Substrates with Tunable Mechanical Properties," *Curr. Protoc. Cell Biol.*, no. SUPPL. 47, pp. 1–16, 2010. DOI: 10.1002/0471143030.cb1016s47.

[97] S. Syed, A. Karadaghy, and S. Zustiak, "Simple Polyacrylamide-based Multiwell Stiffness Assay for the Study of Stiffness-dependent Cell Responses," *J. Vis. Exp.*, vol. 97, pp. 1–12, 2015. DOI: 10.3791/52643.

[98] W. Gross and H. Kress, "Simultaneous measurement of the Young's modulus and the poisson ratio of thin elastic layers," *Soft Matter*, no. 5, 2017. DOI: 10.1039/C6SM02470J.

[99] E. D'Arcangelo and A. P. McGuigan, "Micropatterning strategies to engineer controlled cell and tissue architecture in vitro," *Biotechniques*, vol. 58, no. 1, pp. 13–23, 2015. DOI: 10.2144/000114245.

[100] A. Engler, L. Bacakova, C. Newman, A. Hategan, M. Griffin, and D. Discher, "Substrate Compliance versus Ligand Density in Cell on Gel Responses," *Biophys. J.*, vol. 86, no. 1, pp. 617–628, 2004. DOI: 10.1016/S0006-3495(04)74140-5.

[101] C. Selhuber, "Biological Adhesion on Nanopatterned Substrates Studied with Force Spectroscopy and Microinterferometry," Ph.D. dissertation, 2006. DOI: 10.1002/ejoc.201200111.

[102] C. S. Chen, "Mechanotransduction - a field pulling together?" *J. Cell Sci.*, vol. 121, no. 20, pp. 3285–3292, 2008. DOI: 10.1242/jcs.023507.

[103] P. Roca-Cusachs, V. Conte, and X. Trepat, "Quantifying forces in cell biology," *Nat. Cell Biol.*, vol. 19, no. 7, pp. 742–751, 2017. DOI: 10.1038/ncb3564.

[104] U. S. Schwarz and J. R. Soiné, "Traction force microscopy on soft elastic substrates: A guide to recent computational advances," *Biochim. Biophys. Acta - Mol. Cell Res.*, vol. 1853, no. 11, pp. 3095–3104, 2015. DOI: 10.1016/j.bbamcr.2015.05.028.

[105] K. C. Neuman and A. Nagy, "Single-molecule force spectroscopy: optical tweezers, magnetic tweezers and atomic force microscopy," *Nat. Methods*, vol. 5, no. 6, pp. 491–505, 2008. DOI: 10.1038/nmeth.1218.

[106] D. Martínez-Martín, G. Fläschner, B. Gaub, *et al.*, "Inertial picobalance reveals fast mass fluctuations in mammalian cells," *Nature*, vol. 550, pp. 500–505, 2017. DOI: 10.1038/nature24288.

[107] G. Binnig, C. F. Quate, and C. Gerber, "Atomic Force Microscope," *Phys. Rev. Lett.*, vol. 56, no. 9, pp. 930–934, 1986. DOI: https://doi.org/10.1103/PhysRevLett.56.930.

[108] F. Moreno-Herrero and J. Gomez-Herrero, "General atomic force microscopy," in *At. Force Microsc. Liq. Biol. Appl.* 2012, pp. 1–34, ISBN: 3527327584. DOI: https://doi.org/10.1002/9783527649808.ch1.

[109] J. Helenius, C. P. Heisenberg, H. E. Gaub, and D. J. Muller, "Single-cell force spectroscopy," *J. Cell Sci.*, vol. 121, no. 11, pp. 1785–1791, 2008. DOI: 10.1242/jcs.030999.

[110] E. Hornbogen, G. Eggeler, and E. Werner, *Werkstoffe*, 10.Auflage. Springer Berlin, Heidelberg, 2011, ISBN: 978-3-642-22560-4. DOI: 10.1007/978-3-642-22561-1.

[111] G. Schramm, *A Practical Approach to Rheology and Rheometry*, 2nd ed. Gebrueder Haake, 1994, ISBN: 9783881904674.

[112] F. Haque, "Application of nanoindentation to development of biomedical materials," *Surf. Eng.*, vol. 19, no. 4, pp. 255–268, 2003. DOI: 10.1179/026708403225007464.

[113] D. M. Ebenstein, A. Kuo, J. J. Rodrigo, A. H. Reddi, M. Ries, and L. Pruitt, "A nanoindentation technique for functional evaluation of cartilage repair tissue," *J. Mater. Res.*, vol. 19, pp. 273–281, 2004. DOI: 10.1557/jmr.2004.19.1.273.

[114] U. Ramamurty and J. I. Jang, "Nanoindentation for probing the mechanical behavior of molecular crystals-a review of the technique and how to use it," *CrystEngComm*, vol. 16, no. 1, pp. 12–23, 2014. DOI: 10.1039/c3ce41266k.

[115] M. Galluzzi, G. Tang, C. S. Biswas, J. Zhao, S. Chen, and F. J. Stadler, "Atomic force microscopy methodology and AFMech Suite software for nanomechanics on heterogeneous soft materials," *Nat. Commun.*, vol. 9, no. 1, 2018. DOI: 10.1038/s41467-018-05902-1.

[116] B. V. Derjaguin, V. M. Muller, and Y. P. Toporov, "Effect of Contact Deformation on the Adhesion of Elastic Solids," *J. Colloid Interface Sci.*, vol. 53, no. 2, pp. 314–326, 1975. DOI: https://doi.org/10.1016/0021-9797(75)90018-1.

[117] M. Krieg, G. Fläschner, D. Alsteens, *et al.*, "Atomic force microscopy-based mechanobiology," *Nat. Rev. Phys.*, vol. 1, no. 1, pp. 41–57, 2019. DOI: 10.1038/s42254-018-0001-7.

[118] K. Johnson, K. Kendall, and A. Roberts, "Surface energy and the contact of elastic solids," *Proc. R. Soc. London. A.*, vol. 324, no. 1558, pp. 301–313, 1971. DOI: 10.1098/rspa.1971.0141.

[119] J. Instruments, "Determining the elastic modulus of biological samples using atomic force microscopy," Tech. Rep., 2003.

[120] E. K. Dimitriadis, F. Horkay, J. Maresca, B. Kachar, and R. S. Chadwick, "Determination of Elastic Moduli of Thin Layers of Soft Material Using the Atomic Force Microscope," *Biophys. J.*, vol. 82, no. 5, pp. 2798–2810, 2002. DOI: 10.1016/S0006-3495(02)75620-8.

[121] J. Wegener, A. Janshoff, and L. Steinem, "The Quartz Crystal Microbalance as a Novel Means to Study Cell-Substrate Interactions In Situ," *Cell Biochem. Biophys.*, vol. 34, no. 1, pp. 121–151, 2001. DOI: 10.1385/CBB:34:1:121.

[122] A. S. Rozeik, M. S. Chaar, S. Sindt, *et al.*, "Cellular properties of human gingival fibroblasts on novel and conventional implant-abutment materials," *Dent. Mater.*, vol. 38, no. 3, pp. 540–548, 2022. DOI: 10.1016/j.dental.2021.12.139.

[123] C. Mehl, M. Dent, H. Matthias, P. Med, D. Habil, and A. Zimmermann, "Impact of Cleaning Procedures on Adhesion of Living Cells to Three Abutment Materials," vol. 32, no. 5, 2017. DOI: 10.11607/jomi.5630.

[124] D. G. Grier, "A revolution in optical manipulation," *Nature*, vol. 424, pp. 810–816, 2003. DOI: 10.1038/nature01935.

[125] A. Ashkin, J. M. Dziedzic, J. E. Bjorkholm, and S. Chu, "Observation of a single-beam gradient force optical trap for dielectric particles," *Opt. Angular Momentum*, vol. 11, no. 5, pp. 288–290, 1986. DOI: 10.1364/ol.11.000288.

[126] J. Friedrichs, K. R. Legate, R. Schubert, *et al.*, "A practical guide to quantify cell adhesion using single-cell force spectroscopy," *Methods*, vol. 60, no. 2, pp. 169–178, 2013. DOI: 10.1016/j.ymeth.2013.01.006.

[127] E. Evans and K. Ritchie, "Dynamic Strength of Molecular Adhesion Bonds," *Biophys. J.*, vol. 72, no. 4, pp. 1541–1555, 1997. DOI: 10.1016/S0006-3495(97)78802-7.

[128] R. Merkel, P. Nassoy, A. Leung, K. Ritchie, and E. Evans, "Energy landscapes of receptor-ligand bonds explored with dynamic force spectroscopy," *Nature*, vol. 397, pp. 50–53, 1999. DOI: 10.1038/16219.

[129] B. Bhana, R. K. Iyer, W. L. K. Chen, *et al.*, "Influence of Substrate Stiffness on the Phenotype of Heart Cells," *Biotechnol. Bioeng.*, vol. 105, no. 6, pp. 1148–1160, 2010. DOI: 10.1002/bit.22647.

[130] A. J. Engler, C. Carag-Krieger, C. P. Johnson, *et al.*, "Embryonic cardiomyocytes beat best on a matrix with heart-like elasticity : scar-like rigidity inhibits beating," *J. Cell Sci.*, vol. 121, no. 22, pp. 3794–3802, 2008. DOI: 10.1242/jcs.029678.

[131] H. Geckil, F. Xu, X. Zhang, S. Moon, and U. Demirci, "Engineering hydrogels as extracellular matrix mimics," *Nanomedicine*, vol. 5, no. 3, pp. 469–484, 2010. DOI: 10.2217/nnm.10.12.

[132] A. Burmistrova, M. Richter, C. Uzum, and R. V. Klitzing, "Effect of cross-linker density of P(NIPAM-co-AAc) microgels at solid surfaces on the swelling/shrinking behaviour and the Young's modulus," *Colloid Polym. Sci.*, vol. 289, pp. 613–624, 2011. DOI: 10.1007/s00396-011-2383-2.

[133] A. Buxboim, K. Rajagopal, A. Brown, and D. E. Discher, "How deeply cells feel: methods for thin gels," *J. Phys. Condens. Matter*, vol. 22, no. 19, pp. 1–7, 2010. DOI: 10.1088/0953-8984/22/19/194116.

[134] S. Huth, S. Sindt, and C. Selhuber-Unkel, "Automated analysis of soft hydrogel microindentation: Impact of various indentation parameters on the measurement of Young's modulus," *PLoS One*, vol. 14, no. 8, 2019. DOI: 10.1371/journal.pone.0220281.

[135] M. Doerner and W. Nix, "A method for interpreting the data from depth-sensing indentation instrurments," *J. Mater. Res.*, vol. 1, pp. 601–609, 1986. DOI: https://doi.org/10.1557/JMR.1986.0601.

[136] S. L. Crick and F. C. Yin, "Assessing micromechanical properties of cells with atomic force microscopy: importance of the contact point," *Biomech. Model. Mechanobiol.*, vol. 6, pp. 199–210, 2007. DOI: 10.1007/s10237-006-0046-x.

[137] F. Rico, E. P. Wojcikiewicz, and V. T. Moy, "16 Atomic Force Microscopy Studies of the Mechanical Properties of Living Cells," in *Appl. Scanning Probe Methods IX. Nano Sci. Technolgy*, Springer, Berlin, Heidelberg, 2008, ISBN: 978-3-540-74083-4. DOI: 10.1007/978-3-540-74083-4_4.

[138] N. Gavara, "Combined strategies for optimal detection of the contact point in AFM force-indentation curves obtained on thin samples and adherent cells," *Sci. Rep.*, vol. 6, pp. 1–13, 2016. DOI: 10.1038/srep21267.

[139] E. Barthel, "Adhesive elastic contacts: JKR and more," *J. Phys. D. Appl. Phys.*, vol. 41, no. 16, 2008. DOI: 10.1088/0022-3727/41/16/163001.

[140] C. Storm, J. J. Pastore, F. C. MacKintosh, T. C. Lubensky, and P. A. Janmey, "Nonlinear elasticity in biological gels," *Nature*, vol. 435, pp. 191–194, 2005. DOI: 10.1038/nature03521.

[141] J. S. Field and M. V. Swain, "Determining the mechanical properties of small volumes of material from submicrometer spherical indentations," *J. Mater. Res.*, vol. 10, no. 1, pp. 101–112, 1995. DOI: 10.1557/JMR.1995.0101.

[142] M. M. Chaudhri, "Subsurface plastic strain distribution around spherical indentations in metals," *Philos. Mag. A Phys. Condens. Matter, Struct. Defects Mech. Prop.*, vol. 74, no. 5, pp. 1213–1224, 1996. DOI: 10.1080/01418619608239721.

[143] J. R. Pratt, G. A. Shaw, L. Kumanchik, and N. A. Burnham, "Quantitative assessment of sample stiffness and sliding friction from force curves in atomic force microscopy," *J. Appl. Phys.*, vol. 107, no. 4, 2010. DOI: 10.1063/1.3284957.

[144] J. Stiernstedt, M. W. Rutland, and P. Attard, "A novel technique for the in situ calibration and measurement of friction with the atomic force microscope," *Rev. Sci. Instrum.*, vol. 76, no. 8, pp. 1–9, 2005. DOI: 10.1063/1.2006407.

[145] L.-n. Xu, "Viscoelasticity of mixed polyacrylamide solution," *J. Cent. South Univ.*, vol. 15, no. s1, pp. 443–446, 2008. DOI: 10.1007/s11771008396x.

[146] B. Sabass, M. L. Gardel, C. M. Waterman, and U. S. Schwarz, "High Resolution Traction Force Microscopy Based on Experimental and Computational Advances," *Biophys. J.*, vol. 94, no. 1, pp. 207–220, 2008. DOI: 10.1529/biophysj.107.113670.

[147] J. H. Wen, L. G. Vincent, A. Fuhrmann, *et al.*, "Interplay of matrix stiffness and protein tethering in stem cell differentiation," *Nat. Mater.*, vol. 13, no. 10, pp. 979–987, 2014. DOI: 10.1038/nmat4051.

[148] R. Rüchel and M. D. Brager, "Scanning Electron Microscopic Observations of Polyacrylamide Gels," *Anal. Biochem.*, vol. 68, no. 2, pp. 415–428, 1975. DOI: 10.1016/0003-2697(75)90637-5.

[149] E. Cesewski, M. Singh, Y. Liu, J. Zhang, A. P. Haring, and B. N. Johnson, "Real-time monitoring of hydrogel rheological property changes and gelation processes using high-order modes of cantilever sensors," *J. Appl. Phys.*, vol. 128, no. 17, pp. 1–11, 2020. DOI: 10.1063/5.0020547.

[150] E. Liamas, S. D. Connell, M. Zembyla, R. Ettelaie, and A. Sarkar, "Friction between soft contacts at nanoscale on uncoated and protein-coated surfaces," *Nanoscale*, vol. 13, no. 4, pp. 2350–2367, 2021. DOI: 10.1039/d0nr06527g.

[151] H. A. Marin-Tapia, L. Romero-Salazar, J. C. Arteaga-Arcos, R. Rosales-Ibánez, and M. Mayorga-Rojas, "Micro-mechanical properties of corneal scaffolds from two different bio-models obtained by an efficient chemical decellularization," *J. Mech. Behav. Biomed. Mater.*, vol. 119, p. 104 510, 2021. DOI: 10.1016/j.jmbbm.2021.104510.

[152] R. Zaman, A. Lombardo, C. Sauvanet, *et al.*, "Effector-mediated ERM activation locally inhibits RhoA activity to shape the apical cell domain," *J. Cell Biol.*, vol. 220, no. 6, pp. 1–20, 2021. DOI: 10.1083/jcb.202007146.

[153] S. Huth, J. W. Blumberg, D. Probst, J. Lammerding, U. S. Schwarz, and C. Selhuber-Unkel, "Quantifying force transmission through fibroblasts: changes of traction forces under external shearing," *Eur. Biophys. J.*, vol. 51, 2021. DOI: 10.1007/s00249-021-01576-8.

[154] J. Christian, J. W. Blumberg, D. Probst, *et al.*, "Control of Cell Adhesion using Hydrogel Patterning Techniques for Applications in Traction Force Microscopy," *J. Vis. Exp.*, vol. 179, pp. 1–17, 2022. DOI: 10.3791/63121.

[155] A. E. Dodi, I. O. Ajayi, C. Chang, *et al.*, "Regulation of fibroblast Fas expression by soluble and mechanical pro-fibrotic stimuli," *Respir. Res.*, vol. 19, no. 1, pp. 1–12, 2018. DOI: 10.1186/s12931-018-0801-4.

[156] C.-M. Lo, H.-B. Wang, M. Dembo, and Y.-L. Wang, "Cell Movement is Guided by the Rigidity of the Substrate," *Biophys. J.*, vol. 79, no. 1, pp. 144–152, 2000. DOI: 10.1016/S0006-3495(00)76279-5.

[157] B. J. DuChez, A. D. Doyle, E. K. Dimitriadis, and K. M. Yamada, "Durotaxis by Human Cancer Cells," *Biophys. J.*, vol. 116, no. 4, pp. 670–683, 2019. DOI: 10.1016/j.bpj.2019.01.009.

[158] C. Franck, S. A. Maskarinec, D. A. Tirrell, and G. Ravichandran, "Three-dimensional traction force microscopy: A new tool for quantifying cell-matrix interactions," *PLoS One*, vol. 6, no. 3, 2011. DOI: 10.1371/journal.pone.0017833.

[159] N. M. Kronenberg, P. Liehm, A. Steude, *et al.*, "Long-term imaging of cellular forces with high precision by elastic resonator interference stress microscopy," *Nat. Cell Biol.*, vol. 19, no. 7, pp. 864–872, 2017. DOI: 10.1038/ncb3561.

[160] C. Selhuber-Unkel, T. Erdmann, M. López-García, H. Kessler, U. S. Schwarz, and J. P. Spatz, "Cell Adhesion Strength is Controlled by Intermolecular Spacing of Adhesion Receptors," *Biophys. J.*, vol. 98, no. 4, pp. 543–551, 2010. DOI: 10.1016/j.bpj.2009.11.001.

[161] C. S. Chen, M. Mrksich, S. Huang, G. M. Whitesides, and D. E. Ingber, "Geometric Control of Cell Life and Death," *Science*, vol. 276, no. 5317, pp. 1425–1428, 1997. DOI: 10.1126/science.276.5317.1425.

[162] L. Pieuchot, J. Marteau, A. Guignandon, *et al.*, "Curvotaxis directs cell migration through cell-scale curvature landscapes," *Nat. Commun.*, vol. 9, 2018. DOI: 10.1038/s41467-018-06494-6.

[163] L. F. Kadem, M. Holz, K. G. Suana, *et al.*, "Rapid Reversible Photoswitching of Integrin-Mediated Adhesion at the Single-Cell Level," *Adv. Mater.*, vol. 28, no. 9, pp. 1799–1802, 2016. DOI: 10.1002/adma.201504394.

[164] M. Wirkner, J. M. Alonso, V. Maus, *et al.*, "Triggered Cell Release from Materials Using Bioadhesive Photocleavable Linkers," *Adv. Mater.*, vol. 23, no. 34, pp. 3907–3910, 2011. DOI: 10.1002/adma.201100925.

[165] P. C. Dartsch, H. Hämmerle, and E. Betz, "Orientation of Cultured Arterial Smooth Muscle Cells Growing on Cyclically Stretched Substrates," *Acta Anat. (Basel).*, vol. 125, no. 2, pp. 108–113, 1986. DOI: 10.1159/000146146..

[166] A. Tondon and R. Kaunas, "The Direction of Stretch-Induced Cell and Stress Fiber Orientation Depends on Collagen Matrix Stress," *PLoS One*, vol. 9, no. 2, e89592, 2014. DOI: 10.1371/journal.pone.0089592.

[167] K. Kanda, T. Matsuda, and T. Oka, "Two-dimensional Orientational Response of Smooth Muscle Cells to Cyclic Stretching," *ASAIO J.*, vol. 38, no. 3, pp. M382–385, 1992. DOI: 10.1097/00002480-199207000-00060.

[168] S. Jungbauer, H. Gao, J. P. Spatz, and R. Kemkemer, "Two Characteristic Regimes in Frequency-Dependent Dynamic Reorientation of Fibroblasts on Cyclically Stretched Substrates," *Biophys. J.*, vol. 95, no. 7, pp. 3470–3478, 2008. DOI: 10.1529/biophysj.107.128611.

[169] V. Heitmann and J. Wegener, "Monitoring Cell Adhesion by Piezoresonators: Impact of Increasing Oscillation Amplitudes," *Anal. Chem.*, vol. 79, no. 9, pp. 3392–3400, 2007. DOI: 10.1021/ac062433b.

[170] F. Guo, P. Li, J. B. French, *et al.*, "Controlling cell-cell interactions using surface acoustic waves," *Proc. Natl. Acad. Sci. U. S. A.*, vol. 112, no. 1, pp. 43–48, 2015. DOI: 10.1073/pnas.1422068112.

[171] G. Velve-Casquillas, M. Le Berre, M. Piel, and P. T. Tran, "Microfluidic tools for cell biological research," *Nano Today*, vol. 5, no. 1, pp. 28–47, 2010. DOI: 10.1016/j.nantod.2009.12.001.

[172] R. Langer and J. P. Vacanti, "Tissue Engineering," *Science*, vol. 260, no. 5110, pp. 920–926, 1993. DOI: 10.1126/science.8493529.

[173] S. Singh, L. L. Fujii, M. H. Murad, *et al.*, "Liver Stiffness Is Associated With Risk of Decompensation, Liver Cancer, and Death in Patients with Chronic Liver Diseases: A Systematic Review and Meta-analysis," *Clin. Gastroenterol. Hepatol.*, vol. 11, no. 12, 1573–1584.e2, 2013. DOI: 10.1016/j.cgh.2013.07.034.

[174] J. A. L. Harkness, M. B. Richter, G. S. Panayi, K. Van de Pette, A. Unger, and R. Pownall, "Circadian variation in disease activity in rheumatoid arthritis.," *Br. Med. J. (Clin. Res. Ed).*, vol. 284, pp. 551–554, 1982. DOI: 10.1136/bmj.284.6322.1114-d.

[175] K. Hosseini, A. Taubenberger, C. Werner, and E. Fischer-friedrich, "EMT-Induced Cell-Mechanical Changes Enhance Mitotic Rounding Strength," *Adv. Sci.*, vol. 7, no. 19, 2001276 (1–12), 2020. DOI: 10.1002/advs.202001276.

[176] R. J. Ferguson, A. J. Palmer, A. Taylor, M. L. Porter, H. Malchau, and S. Glyn-Jones, "Hip replacement," *Hip Knee Replace.*, vol. 392, no. 10158, pp. 1662–1671, 2018. DOI: 10.1016/S0140-6736(18)31777-X.

[177] W. M. Mihalko, H. Haider, S. Kurtz, M. Marcolongo, and K. Urish, "New materials for hip and knee joint replacement: What's hip and what's in kneed?" *J. Orthop. Res.*, vol. 38, no. 7, pp. 1436–1444, 2020. DOI: 10.1002/jor.24750.

[178] T. Liu, M. Ead, S. D. Cruz, *et al.*, "Polycarbonate-urethane coating can significantly improve talus implant contact characteristics," *J. Mech. Behav. Biomed. Mater.*, vol. 125, p. 104 936, 2022. DOI: 10.1016/j.jmbbm.2021.104936.

[179] E. Moeendarbary, I. P. Weber, G. K. Sheridan, *et al.*, "The soft mechanical signature of glial scars in the central nervous system," *Nat. Commun.*, vol. 8, 2017. DOI: 10.1038/ncomms14787.

[180] E. Kolaya and B. L. Firestein, "Deep brain stimulation: Challenges at the tissue-electrode interface and current solutions," *Biotechnol. Prog.*, vol. 37, no. 5, pp. 1–8, 2021. DOI: 10.1002/btpr.3179.

[181] C. Schmitt, A. Lechanteur, F. Cossais, *et al.*, "Liposomal Encapsulated Curcumin Effectively Attenuates Neuroin fl ammatory and Reactive Astrogliosis Reactions in Glia Cells and Organotypic Brain Slices," *Int. J. Nanomedicine*, vol. 15, pp. 3649–3667, 2020. DOI: 10.2147/IJN.S245300.

[182] P. Boodagh, R. Johnson, C. Maly, Y. Ding, and W. Tan, "Soft-sheath, stiff-core microfiber hydrogel for coating vascular implants," *Colloids Surfaces B Biointerfaces*, vol. 183, 2019. DOI: 10.1016/j.colsurfb.2019.110395.

[183] P. W. Oakes, Y. Beckham, J. Stricker, and M. L. Gardel, "Tension is required but not sufficient for focal adhesion maturation without a stress fiber template," *J. Cell Biol.*, vol. 196, no. 3, pp. 363–374, 2012. DOI: 10.1083/jcb.201107042.

[184] C. F. Guimarães, L. Gasperini, A. P. Marques, and R. L. Reis, "The stiffness of living tissues and its implications for tissue engineering," *Nat. Rev. Mater.*, vol. 5, pp. 351–370, 2020. DOI: 10.1038/s41578-019-0169-1.

[185] C. A. Mullen, T. J. Vaughan, K. L. Billiar, and L. M. McNamara, "The Effect of Substrate Stiffness, Thickness, and Cross-Linking Density on Osteogenic Cell Behavior," *Biophys. J.*, vol. 108, no. 7, pp. 1604–1612, 2015. DOI: 10.1016/j.bpj.2015.02.022.

[186] C. M. Denais, R. M. Gilbert, P. Isermann, *et al.*, "Nuclear envelope rupture and repair during cancer cell migration," *Science*, vol. 352, no. 6283, pp. 353–358, 2016. DOI: 10.1126/science.aad7297.

[187] C. T. Mierke, D. Rösel, B. Fabry, and J. Brábek, "Contractile forces in tumor cell migration," *Eur. J. Cell Biol.*, vol. 87, no. 8-9, pp. 669–676, 2008. DOI: 10.1016/j.ejcb.2008.01.002.

[188] M. Beil, A. Micoulet, G. Von Wichert, *et al.*, "Sphingosylphosphorylcholine regulates keratin network architecture and visco-elastic properties of human cancer cells," *Nat. Cell Biol.*, vol. 5, no. 9, pp. 803–811, 2003. DOI: 10.1038/ncb1037.

[189] M. Ye, H. M. Sanchez, M. Hultz, *et al.*, "Brain microvascular endothelial cells resist elongation due to curvature and shear stress," *Sci. Rep.*, vol. 4, pp. 1–6, 2014. DOI: 10.1038/srep04681.

[190] S. Li, M. Kim, Y. L. Hu, *et al.*, "Fluid Shear Stress Activation of Focal Adhesion Kinase. Linking to Mitogen-activated Protein Kinases," *J. Biol. Chem.*, vol. 272, no. 48, pp. 30 455–30 462, 1997. DOI: 10.1074/jbc.272.48.30455.

[191] K. S. Cunningham and A. I. Gotlieb, "The role of shear stress in the pathogenesis of atherosclerosis," *Lab. Investig.*, vol. 85, no. 1, pp. 9–23, 2005. DOI: 10.1038/labinvest.3700215.

[192] E. A. Osborn, A. Rabodzey, C. F. Dewey, and J. H. Hartwig, "Endothelial actin cytoskeleton remodeling during mechanostimulation with fluid shear stress," *Am. J. Physiol. - Cell Physiol.*, vol. 290, no. 2, pp. 444–453, 2006. DOI: 10.1152/ajpcell.00218.2005.

[193] D. C. Fernandes, T. L. Araujo, F. R. Laurindo, and L. Y. Tanaka, "Hemodynamic Forces in the Endothelium: From Mechanotransduction to Implications on Development of Atherosclerosis," in *Endothel. Cardiovasc. Dis. Vasc. Biol. Clin. Syndr.* Academic Press, 2018, ch. 7, pp. 85–95, ISBN: 978-0-12-812348-5. DOI: 10.1016/B978-0-12-812348-5.00007-6.

[194] S. Bajaj, R. Parikh, A. Hamdan, and M. Bikkina, "Covered-stent treatment of coronary aneurysm after drug-eluting stent placement: Case report and literature review," *Texas Hear. Inst. J.*, vol. 37, no. 4, pp. 449–454, 2010.

[195] P. F. Davies, A. Robotewskyj, and M. L. Griem, "Quantitative studies of endothelial cell adhesion. Directional remodeling of focal adhesion sites in response to flow forces," *J. Clin. Invest.*, vol. 93, no. 5, pp. 2031–2038, 1994. DOI: 10.1172/jci117197.

[196] R. Salánki, C. Hos, N. Orgovan, *et al.*, "Single cell adhesion assay using computer controlled Micropipette," *PLoS One*, vol. 9, no. 10, pp. 1–12, 2014, ISSN: 19326203. DOI: 10.1371/journal.pone.0111450.

[197] R. Paul, P. Heil, J. P. Spatz, and U. S. Schwarz, "Propagation of Mechanical Stress through the Actin Cytoskeleton toward Focal Adhesions: Model and Experiment," *Biophys. J.*, vol. 94, no. 4, pp. 1470–1482, 2008. DOI: 10.1529/biophysj.107.108688.

[198] P. Rupprecht, L. Golé, J.-p. Rieu, *et al.*, "A tapered channel microfluidic device for comprehensive cell adhesion analysis , using measurements of detachment kinetics and shear stress-dependent motion A tapered channel microfluidic device for comprehensive cell adhesion analysis , using measurement," *Biomicrofluidics*, vol. 6, no. 1, p. 014 107, 2012. DOI: 10.1063/1.3673802.

[199] D. D. Nalayanda, Q. Wang, W. B. Fulton, T. H. Wang, and F. Abdullah, "Engineering an artificial alveolar-capillary membrane: a novel continuously perfused model within microchannels," *J. Pediatr. Surg.*, vol. 45, no. 1, pp. 45–51, 2010. DOI: 10.1016/j.jpedsurg.2009.10.008.

[200] F. S. Majedi, M. M. Hasani-Sadrabadi, T. J. Thauland, S. Li, L.-S. Bouchard, and M. J. Butte, "Augmentation of T-Cell Activation by Oscillatory Forces and Engineered Antigen-Presenting Cells," *Nano Lett.*, vol. 19, no. 10, pp. 694 5–6954, 2019. DOI: 10.1021/acs.nanolett.9b02252.

[201] K. Kouzbari, M. R. Hossan, J. H. Arrizabalaga, *et al.*, "Oscillatory shear potentiates latent TGF-β1 activation more than steady shear as demonstrated by a novel force generator," *Sci. Rep.*, vol. 9, pp. 1–8, 2019. DOI: 10.1038/s41598-019-42302-x.

[202] O. Onaizah, L. Xu, K. Middleton, L. You, and E. Diller, "Local stimulation of osteocytes using a magnetically actuated oscillating beam," *PLoS One*, vol. 15, no. 6, e0235366, 2020. DOI: 10.1371/journal.pone.0235366.

[203] M. Hagiwara, T. Kawahara, and F. Arai, "Local streamline generation by mechanical oscillation in a microfluidic chip for noncontact cell manipulations," *Appl. Phys. Lett.*, vol. 101, no. 7, pp. 1–4, 2012. DOI: 10.1063/1.4746247.

[204] V. Barsegov and D. Thirumalai, "Dynamics of unbinding of cell adhesion molecules: Transition from catch to slip bonds," *Proc. Natl. Acad. Sci. U. S. A.*, vol. 102, no. 6, pp. 1835–1839, 2005. DOI: 10.1073/pnas.0406938102.

[205] R. Oropesa-Nunez, A. Mescola, M. Vassalli, and C. Canale, "Impact of Experimental Parameters on Cell-Cell Force Spectroscopy Signature," *Sensors*, vol. 21, no. 4, pp. 1–11, 2021. DOI: https://doi.org/10.3390/s21041069.

[206] P. W. Oakes, E. Wagner, C. A. Brand, *et al.*, "Optogenetic control of RhoA reveals zyxin-mediated elasticity of stress fibres," *Nat. Commun.*, vol. 8, 2017. DOI: 10.1038/ncomms15817.

[207] S. Hong, E. Ergezen, R. Lec, and K. A. Barbee, "Real-time analysis of cell-surface adhesive interactions using thickness shear mode resonator," *Biomaterials*, vol. 27, no. 34, pp. 5813–5820, 2006. DOI: 10.1016/j.biomaterials.2006.07.031.

[208] J. J. Paszkowiak and A. Dardik, "Arterial Wall Shear Stress: Observations from the Bench to the Bedside," *Vasc. Endovascular Surg.*, vol. 37, no. 1, pp. 47–57, 2003. DOI: 10.1177/153857440303700107.

[209] H. A. Fozzard, "Heart: excitation-contraction coupling," *Annu. Rev. Physiol.*, vol. 35, pp. 201–220, 1977. DOI: 10.1146/annurev.ph.39.030177.001221.

[210] L. Irons, H. Huang, M. R. Owen, R. D. O'Dea, G. A. Meininger, and B. S. Brook, "Switching behaviour in vascular smooth muscle cell–matrix adhesion during oscillatory loading," *J. Theor. Biol.*, vol. 502, pp. 1–12, 2020. DOI: 10.1016/j.jtbi.2020.110387.

[211] L. You, S. Temiyasathit, P. Lee, *et al.*, "Osteocytes as mechanosensors in the inhibition of bone resorption due to mechanical loading," *Bone*, vol. 42, no. 1, pp. 172–179, 2008. DOI: 10.1016/j.bone.2007.09.047.

[212] J. C. Crockett, M. J. Rogers, F. P. Coxon, L. J. Hocking, and M. H. Helfrich, "Bone remodelling at a glance," *J. Cell Sci.*, vol. 124, no. 7, pp. 991–998, 2011. DOI: 10.1242/jcs.063032.

[213] P. P. Weafer, N. H. Reynolds, S. P. Jarvis, and J. P. McGarry, "Single cell active force generation under dynamic loading - Part I: AFM experiments," *Acta Biomater.*, vol. 27, pp. 236–250, 2015. DOI: 10.1016/j.actbio.2015.09.006.

[214] V. Jeyalakshmi Devi, "Artificial cardiac pacemaker," *3rd Int. Conf. Sci. Technol. Eng. Manag.*, pp. 1015–1017, 2017. DOI: 10.1109/ICONSTEM.2017.8261320.

[215] M. Rabbani, M. Tafazzoli-Shadpour, M. A. Shokrgozar, M. Janmaleki, and M. Teymoori, "Cyclic Stretch Effects on Adipose-Derived Stem Cell Stiffness , Morphology and Smooth Muscle Cell Gene Expression," *Tissue Eng. Regen. Med.*, vol. 14, no. June, pp. 279–286, 2017. DOI: 10.1007/s13770-017-0033-6.

[216] J. Hatami, M. Tafazzoli-Shadpour, N. Haghighipour, M. A. Shokrgozar, and M. Janmaleki, "Influence of Cyclic Stretch on Mechanical Properties of Endothelial Cells," *Exp. Mech.*, vol. 53, no. October, pp. 1291–1298, 2013. DOI: 10.1007/s11340-013-9744-3.

[217] L. F. Kadem, K. G. Suana, M. Holz, *et al.*, "High-Frequency Mechanostimulation of Cell Adhesion," *Angew. Chemie - Int. Ed.*, vol. 56, no. 1, pp. 225–229, 2017. DOI: 10.1002/anie.201609483.

[218] M. Hippler, K. Weißenbruch, K. Richler, *et al.*, "Mechanical stimulation of single cells by reversible host-guest interactions in 3D microscaffolds," *Sci. Adv.*, vol. 6, no. 39, pp. 1–13, 2020. DOI: 10.1126/sciadv.abc2648.

[219] N. Sivanantha, C. Ma, D. J. Collins, *et al.*, "Characterization of adhesive properties of red blood cells using surface acoustic wave induced flows for rapid diagnostics," *Appl. Phys. Lett.*, vol. 105, no. 10, p. 103 704, 2014. DOI: 10.1063/1.4895472.

[220] P. P. Weafer, J. P. McGarry, M. H. van Es, *et al.*, "Stability enhancement of an atomic force microscope for long-term force measurement including cantilever modification for whole cell deformation," *Rev. Sci. Instrum.*, vol. 83, no. 9, p. 093 709, 2012. DOI: 10.1063/1.4752023.

[221] M. M. Pathak, J. L. Nourse, T. Tran, *et al.*, "Stretch-activated ion channel Piezo1 directs lineage choice in human neural stem cells," *Proc. Natl. Acad. Sci. U. S. A.*, vol. 111, no. 45, pp. 16 148–16 153, 2014. DOI: 10.1073/pnas.1409802111.

[222] A. N. Pisarchik, V. A. Maksimenko, and A. E. Hramov, "From Novel Technology to Novel Applications: Comment on "An Integrated Brain-Machine Interface Platform With Thousands of Channels" by Elon Musk and Neuralink," *J. Med. Internet Res.*, vol. 21, no. 10, e16356, 2019. DOI: 10.2196/16356.

Publications

S. Huth*, **S. Sindt***, and C. Selhuber-Unkel, "Automated analysis of soft hydrogel microindentation: Impact of various indentation parameters on the measurement of Young's modulus," *PLoS ONE*, vol. 14, no. 8, 2019. doi:10.1371/journal.pone.0220281. (* shared first-authorship)

F. Block, F. Klingbeil, S. Deshpande, U. Sajjad, D. Seidler, C. Arndt, **S. Sindt**, C. Selhuber-Unkel, J. McCord, "Unidirectional transport of superparamagnetic beads and biological cells along oval magnetic elements," *Applied Physics Letters*, vol. 118, no. 23, p. 232 405, 2021. doi:10.1063/5.0044310.

J. Christian, J. W. Blumberg, D. Probst, C. Lo Guidice, **S. Sindt**, C. Selhuber-Unkel, U. S. Schwarz, E. A. Cavalcanti-Adam, "Control of cell adhesion using hydrogel patterning techniques for applications in traction force microscopy," *Journal of Visualized Experiments*, vol. 179, pp. 1–17, 2022. doi:10.3791/63121.

A. S. Rozeik, M. S. Chaar, **S. Sindt**, S. Wille, C. Selhuber-Unkel, M. Kern, S. El-Kholy, C. Dörfer, K. M. Fawzy El-Sayed, "Cellular properties of human gingival fibroblasts on novel and conventional implant-abutment materials," *Dental Materials*, vol. 38, no. 3, pp. 540–548, 2022. doi:10.1016/j.dental.2021.12.139.

Acknowledgment

Mein erster Dank gilt Prof. Dr. Christine Selhuber-Unkel für ihre jahrelange Unterstützung. Sehr schnell hast du mir verantwortungsvolle Aufgaben übertragen und mir viele Konferenzteilnahmen im In- und Ausland ermöglicht. Ich danke dir für dieses Vertrauen und deine kontinuierliche Unterstzützung auch über das Fachliche hinaus! Für mich ist das nicht selbstverständlich.

Ich freue mich, dass ich Prof. Dr. Regine Willumeit-Römer als meine Zweitgutachterin gewinnen konnte. Danke für deine Bereitschaft und Flexibilität!

Ich bin für die sehr unterschiedlichen Kooperationen während meiner Promotionszeit dankbar. Insbesondere danke ich Joel Christian für die erfolgreiche Zusammenarbeit und Unterstützung meiner AFM-Versuche.

Außerdem bin ich Dr. Kate Poole sehr dankbar für ihre herzliche Aufnahme in Sydney, wenn auch coronabedingt leider nur sehr kurz. Ich danke dir für deine Unterstützung während dieses verrückten Ausflugs und es war toll, dass wir das geplante Projekt abgewandelt in Heidelberg umsetzen konnten. Ich hätte gerne vor Ort mit dir und deiner Arbeitsgruppe zusammen gearbeitet und dabei sicherlich eine tolle Zeit mit vielen schönen Erfahrungen erlebt.

Für die Entwicklung der AFM-basierten Manipulationssysteme hatte ich großartige Unterstützung vom Applikationsteam von JPK Instruments. Insbesondere bin ich Dr. Thomas Henze für die erfolgreiche, unkomplizierte Zusammenarbeit dankbar.

Ich bin den Mitarbeitenden der TF-Werkstatt dankbar für die zuverlässige und schnelle Unterstützung. Ein großer Dank an Berndt Neumann, der meine Wünsche und Vorstellungen umgesetzt hat. Ich konnte meine Bauteile eigentlich immer schneller abholen als er angekündigt hatte. Das war eine große Hilfe!

Ich bin froh und dankbar als assoziiertes Mitglied im Graduiertenkolleg “Materials for Brain” (GRK2154, gefördert durch die DFG) gewesen zu sein. Dadurch habe ich sehr unterschiedliche Erfahrungen sammeln können. Danke Dr. Tina Kerby für die Hilfe bei den GRK-Dokumenten und die THW-Gespräche abseits des GRKs.

Ohne mein Büro wären die letzten Jahre sicherlich nur halb so lustig und schön gewesen. Egal ob das nachmittägliche Darts im Büro, die Pizza im Privaten oder einfach ein kurzer Plausch zwischendurch; ich habe die Zeit sehr genossen! Ein großes Danke an Christine Arndt, Dr.-Ing. Nils Lukat, Tobias Spratte und Dr.-Ing. Michael Timmermann! Zusätzlich war unsere Büro-Reunion in Heidelberg, bei der sich Dr.-Ing. Laith Kadem einfach mit eingeschlichen hat, natürlich genial.

Mit Dr. rer. nat. Steven Huth war die Arbeit zwar häufig recht chaotisch, aber ich hatte immer wieder ein Schmunzeln im Gesicht. Danke für deine gute Einweisung ins AFM, den Startschuss in MATLAB und generell die coole, schöne Zeit! Unser 1-Woche-Paper-Erlebnis werde ich wohl so schnell nicht vergessen.

Was AFM angeht bin ich auch Dr.-Ing. Laith Kadem und Dr.-Ing. Dipl.-Chem. Hendrikje Neumann für ihre Unterstützung dankbar. Ich konnte immer Jemanden von euch erwischen und ihr standet mir mit Rat und Tat zur Seite. Laith, deine Erfahrung bei den Zellversuchen haben mich voran gebracht!

Ich schätze mich glücklich, dass ich in den letzten Jahren wunderbare Studierende im Labor betreuen und sie ein Stück begleiten durfte. Ich danke Johanna Buck, Annina Graeber, Yannic Hallier, Zuzana Johanovska, Raunak Lohar, Galen Ream, Hela Uplegger und Marijke Wessel für eure Beiträge zu meiner Forschung und den unterschiedlichen Erfahrungen mit euch! Insbesondere danke ich Johanna Buck für die erfolgreiche Zusammenarbeit und ihr Engagement. Wir haben wirklich das Beste aus einer online-Betreuung herausgeholt.

Ein besonderes Erlebnis war die Zeit mit Yasmeen El-Rayyes, das durch das RISE Germany Stipendium des DAAD möglich war. Ich bin dankbar, dass ich mich bei der Auswahl für dich entschieden habe und es war cool, dass wir uns in Toronto wiedergesehen haben und du mir die *BeaverTails* gezeigt hast.

Ich bin dankbar ein Teil der Arbeitsgruppe *Biokompatible Nanomaterialien* gewesen zu sein. Insbesondere bin ich Ellen Riemer für ihre verwaltungsseitige Unterstützung dankbar. Du hattest immer gute Laune und warst für einen Spaß zu haben. Ein herzliches Danke an Dipl.-Ing. Manuela Lieb, die unser Labor immer in Ordnung gehalten hat und die *Streuselschnecken*-Leidenschaft mit mir teilt. Ich habe mich immer gefreut, wenn du während des letzten Jahres einfach mal reingeschneit bist und wir ein bisschen über Dies und Das quatschen konnten. Danke an die "neuen" und "alten" Bnanos in Heidelberg! Es war toll, dass ihr mich so lieb dort unten im Süden aufgenommen habt. Dadurch hatte ich einen schönen Aufenthalt mit vielen schönen Erinnerungen.

Ich bin Dr.-Ing. Brook Shurtleff dankbar für die erfolgreiche Zusammenarbeit in der Lehre. Vielen Dank für das Teilen deiner Erfahrungen und die motivierenden Gespräche! Ich hoffe du hast nicht zu viele Albträume von Olat. Außerdem ein großes Dankeschön für die sprachliche Korrektur meiner Doktorarbeit!

Ich bin froh über meine TF-Freundschaften mit Katharina, Lars, Lea und Lena. Wir hatten viele coole und schöne Erlebnisse; sei es bei Spieleabenden, Leberkäse essen oder einfach einem Spaziergang im Park oder am Wasser. Die endlosen Runden Billard mit Lea habe ich zu gut und gerne in Erinnerung.

Immer wieder eine tolle, entspannte, lustige, erdende Zeit habe ich mit meiner längsten -unfassbare 20 Jahre- und besten Freundin Lena. *Immer werden wir so bleiben...wir beide.* Behalte deinen Frohsinn; der ist ansteckend! DANKE für deine Freundschaft!!

Ich bin unheimlich dankbar für meine Familie, die ein großer Anker für mich ist, und mich immer wieder unterstützt. Hans-Jürgen, es ist toll, dass wir die Handball-

Leidenschaft teilen und Antje und ich uns immer auf dich verlassen können. Ich bin dankbar, dass du Teil meines Lebens bist! Mama, du bist mir unglaublich wichtig und ich bin immer für dich da. Gerne denke ich an unsere gemeinsame Zeit im Herbst zurück und hoffe, dass wir das bald wiederholen können.

Was mir meine Schwester Sabrina bedeutet, lässt sich kaum in Worte fassen. So unterschiedlich wir in manchen Bereichen sind, so ähnlich sind wir uns in anderen Dingen und verrückt sind wir irgendwie auch. Wie schön, dass du mit Manni eine ähnliche Verrücktheit in unsere Familie gebracht hast. Ich sag nur *sie wars*. Sabrina, du bist *die immer lacht* und jeder Mensch, der dich Teil seines Lebens nennen darf, hat einen unbeschreiblichen Reichtum.

Ganz besondere Unterstützung habe ich schon immer von meiner Tante Antje erhalten. Du bist einfach eine gute Seele, die immer für Jeden da ist und ein offenes Ohr hat. Es ist toll, dass wir die Leidenschaft für den Garten, insbesondere die Rosen, miteinander teilen und uns gegenseitig so viel Freude bringen. Danke für deine stetige Unterstützung, in Allem was ich mache! Ich bin froh, dass unser Zusammenleben eine solche Symbiose gebildet hat und ich freue mich auf unser nächstes Projekt!

Ruben, du bist ein toller Mensch und ich bin froh, dass du damals durch die FS-Tür in mein Leben gestapft bist. Danke für die viele Geduld und die Diskussionen über den Zellkram, mit dem du eigentlich gar nichts am Hut hast! Lass uns diesen Sommer wieder die Bienen im Garten besuchen; das war lustig. Danke, dass du Teil meines Lebens bist!

Einige Menschen, denen ich viel zu verdanken habe, können diesen Abschluss leider nicht mehr miterleben. Ich bin dankbar, dass ihr Teil meines Lebens ward und behalte die vielen schönen Momente in meiner Erinnerung.

Appendix

A Abbreviations and Symbols

Table 1: Symbols

χ	squared sum of the fitting residuals
ϵ	strain
ν	Poisson's ratio
a	radius of the contact area between a surface and an indenter
A	cell spreading area
C	cell circularity
cp	distance value at the contact point
d	indentation depth
d_{max}	distance value at maximum indentation force
$d_{rupture}$	distance value of a bond rupture
E	Young's modulus
E-d curve	Young's modulus as a function of indentation depth
f	arbitrary function
F	setpoint force or indentation force
k	spring constant
p	perimeter of a cell
r	loading rate
R	radius of an indenter
t	time
t_{bond}	bond lifetime
v	pulling speed

Table 2: Abbreviations

AFM	atomic force microscope or atomic force microscopy
a-NHS	acrylic acid *N*-hydroxysuccimide ester
APS	ammonium persulfate
CAM	cell adhesion molecule
conA	concanavalin A
DNA	deoxyribonucleic acid
DMEM	Dulbecco's Modified Eagle's Medium
DMT model	Derjaguin-Muller-Toropov model
ECM	extracellular matrix
EDTA	ethylenediaminetetraacetic acid
FBS	fetal bovine serum
HEK293	human embryonic kidney cells
HEK293T	modified human embryonic kidney cells
HEPES	2-[4-(2-Hydroxyethyl)piperazin-1-yl]ethane-1-sulfonic acid
HT1080	fibrosarcoma cells
JKR model	Johnson-Kendall-Roberts model
LUVI-TFM	local UV illumination traction force microscopy
Mod.	modulation mode/measurement
$NaOHCO_2$	sodium bicarbonate
NaOH	sodium hydroxide
NIH-3T3	fibroblast cell line
Norm.	normal mode/measurement
n.s.	not significant or no significance
PAM	polyacrylamide
PBS	phosphate buffer saline
PDL	poly-D-lysine
PDMS	polydimethylsiloxane
Pen/Strep	penicillin streptomycin
PLL	poly-L-lysine
PLL-PEG	poly-L-lysine-poly(ethylene glycol)
Ref.	reference mode/measurement
REF 52-wt	rat embryonic fibroblast cells wild type
SAW	surface acoustic wave
SCFS	single cell force spectroscopy
TAO	tip assisted optics module
TFM	traction force microscope or traction force microscopy
TIRFM	total internal reflection fluorescence microscopy
TEMED	N, N, N', N'-tetramethylethylenediamine

B Materials and Methods

B.1 AFM Setups

B.1.1 CellHesion® 200 setup (CH200)

The CellHesion® 200 setup was mounted on an IX73 inverted microscope (Olympus Deutschland GmbH) equipped with a Progress MF cool camera (Jenoptik) and a motorized precision stage (JPK Instruments) with a travel range of $20 \cdot 20$ mm^2. The system was controlled with the JPK control software (latest version 6.1.72, JPK Instruments).

B.1.2 NanoWizard® 3 setup

The NanoWizard® 3 setup was mounted on an IX71 inverted microscope (Olympus Deutschland GmbH) equipped with a Progress MF cool camera (Jenoptik) and either a manual stage (JPK Instruments) or a tip assisted optics module (TAO, JPK Instruments) with a travel range of $100 \cdot 100$ µm^2 range with nanometer precision. The system was controlled with the JPK control software (latest version 4.3.5, JPK Instruments).

B.2 Convention of boxplots and significance levels

The convention of all boxplots presented is as follows: A box shows 25-75 % of a value determined, the square shows the mean value, the horizontal line gives the median, the crosses present the minimum and maximum of the distribution, whereas the whiskers represent outliers.

The convention of the significance levels determined with a student's t-test is as follows: * $p < 0.05$, *** $p < 0.001$ or not significant (n.s.) at $p < 0.05$.

B.3 Cell Culture of REF 52-wt and HT1080

Rat embryonic fibroblast (REF 52-wt) or fibrosarcoma (HT1080) cells were cultured at 37°C with 5 % carbon dioxide content and passaged at 70-90 % confluency. For this purpose, the cells were washed with phosphate buffered saline (PBS, 1 %) and incubated either with a 0.05 % Trypsin/0.02 % EDTA solution (Sigma-Aldrich) or Accutase™ (Sigma-Aldrich) for 5 min at 37°C. Then, the cell suspension was centrifuged at 800 g for 4 min. The supernatant was removed and the cell pellet was resuspended with fresh medium. The seeding densities varied between 1:2 and 1:40 for culturing or 5,000-30,000 cells per well for experiments. More details are shown in the corresponding sections.

C Determination of Young's Moduli of Bulk Polyacrylamide

Bulk PAM samples produced in 4 mm Teflon™ molds were indented with a home-built indenter system previously reported in [94] after 48 h swelling in bidest. water. 10 indentation curves were recorded at 3 sample positions. The indenter radius was 3 mm, the speed was 0.5 mm/s and the indentation depth was 1 mm. The indentation curves were analyzed with our newly developed MATLAB algorithm. Figure 1 shows the distribution of Young's moduli determined, where each box represents 25-75 % of Young's moduli, the square shows mean Young's moduli, the horizontal line gives the median, the crosses present the smallest and highest Young's modulus, respectively, whereas the whiskers represent outliers. A bis-acrylamide concentration of 5 % refers to "soft", whereas 18 % displays "stiff" samples.

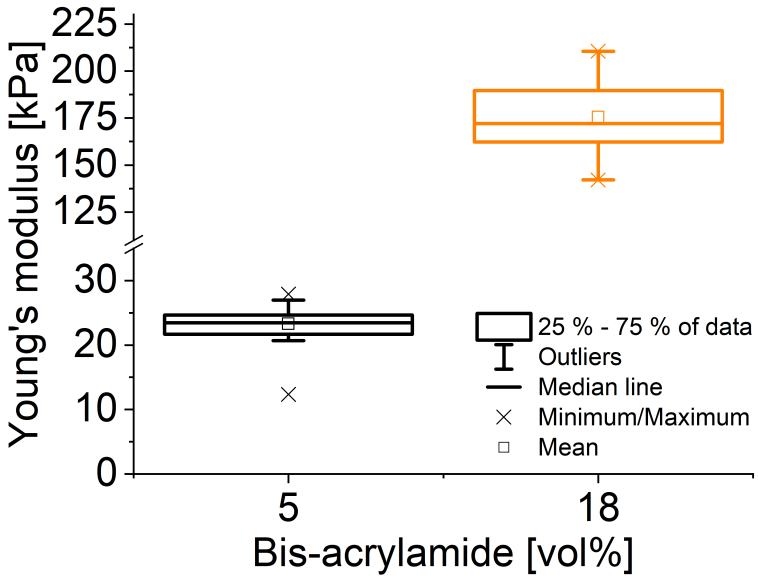

Figure 1: Distribution of Young's moduli measured with a home-built indenter system. Our newly developed MATLAB algorithm was used to analyze the indentation data. "Soft" samples have a mean Young's modulus of ca. 23 kPa, whereas "stiff" samples have a mean Young's modulus of ca. 175 kPa. This covers a reasonable range of tissue stiffnesses.

D Supporting Information for AFM-based Shear Measurements of Single Fibroblast Cells

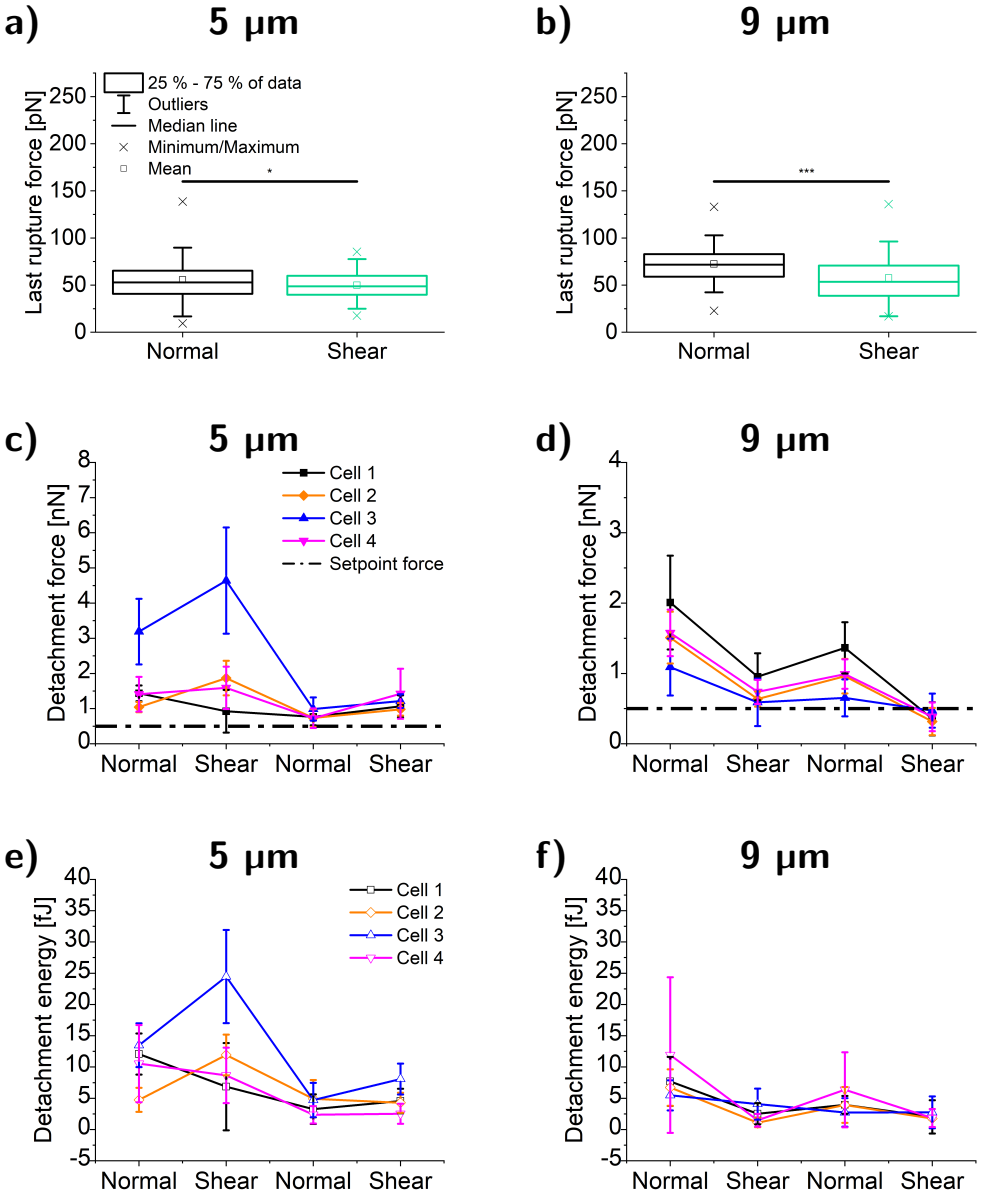

Figure 2: Supporting/Additional data from AFM-based shear with shear distances of 5 µm (left column) and 9 µm (right column). The determined last rupture forces decreased significantly for shear distances of a) 5 µm and b) 9 µm compared to last rupture forces of normal measurements (significance levels of * $p < 0.05$ or *** $p < 0.001$). c) Shear distances of 5 µm mostly increased the detachment forces compared to detachment forces for normal measurements, whereas shear distances of d) 9 µm resulted in decreased detachment forces. In addition, an overall negative, harmful impact of large shear distances can be suggested. The results of the detachment energies for shear distances of e) 5 µm and f) 9 µm followed the same trends of the detachment forces.

E Supporting Information for Pilot Oscillatory Manipulations

Figure 3 shows results of pilot oscillatory experiments with a 10 nm amplitude at a) 1 Hz and b) 10 Hz. Each box represents 25-75 % of detachment forces determined from up to 20 force-distance curves, the square shows mean detachment forces, the horizontal line gives the median, the crosses present the smallest and highest detachment force, respectively, whereas the whiskers represent outliers. At first, 20 force-distance curves were measured without modulation (i.e., normal detachment measurement, labeled in black) followed by the measurement of 20 force-distance curves with modulation (labeled in light turquoise). After this first cycle, two further measurement cycles with the same experimental setup were conducted.

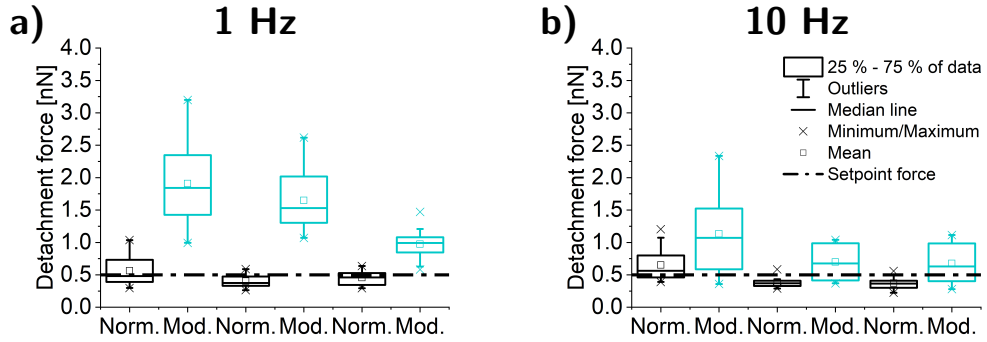

Figure 3: Distributions of detachment forces for two modulation frequencies as a function of normal and modulation modes. Comparison of distributions of detachment forces measured for modulations with 10 nm amplitudes at frequencies of a) 1 Hz and b) 10 Hz. The pilot tests of modulation show a huge increase of detachment forces for modulation modes, which is more pronounced at 1 Hz. Since the detachment forces determined slightly decreased for normal modes after the first cycle, it is likely that the modulation was exhausting for the cells.

For both modulation frequencies, the detachment forces show a noticeable shift towards larger values as response to a modulation. This is less pronounced for 10 Hz. However, the detachment forces for normal modes slightly decrease after the first cycle, which indicates that the modulation is exhausting for the cells. Checking the progress of force-time curve during the modulation revealed a drastic, unpredictable artifact of the modulation segment that was even more pronounced for a modulation amplitude of 1000 nm, where forces above 40 nN were observed (see Figure 4). Since the setpoint force applied to a cell correlates with detachment forces determined, it is reasonable that the observed increased detachment forces were related to the huge increase of force rather than a successful cell modulation.

Thus, I developed an alternative method for applying oscillatory pushing and pulling. Since I used the force ramp designer to implement consecutively down and up movements of the cantilever in z-direction, I called this method a “z-stimulation”. A sketch of the consecutive down and up movements during cell-substrate contact is

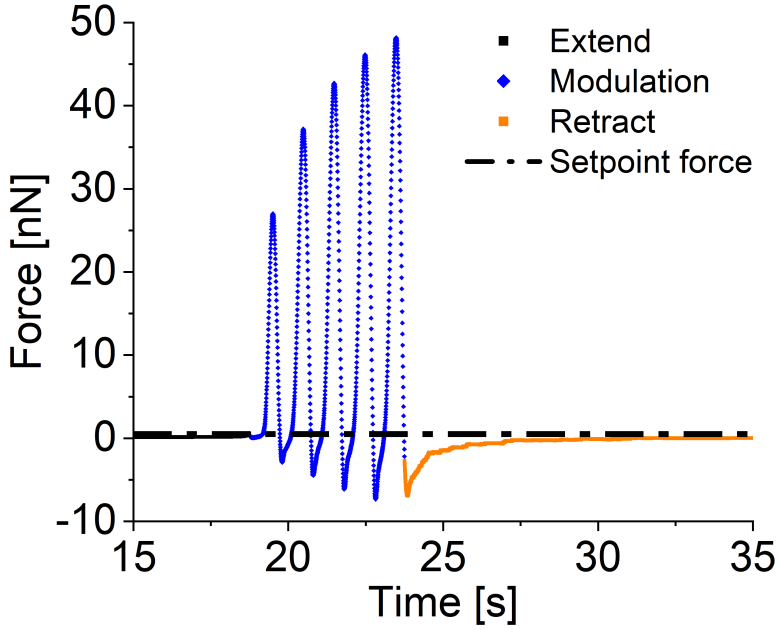

Figure 4: Force-time curve of a pilot modulation showed an unpredictable increase of applied force during the modulation segment. A pilot modulation with a modulation amplitude of 1000 nm at 1 Hz resulted in forces additionally applied above 40 nN.

visualized in Figure 5 a). However, the maximum number of segments was 40 limiting the number of possible periods, distances and speeds for the down and up movement and a reduction of the contact time to 1 s was necessary. In addition, it was rather a gradual down and up movement of the cantilever than an oscillation of the cantilever, which was originally planned. I conducted example measurements with distances of 10-1000 nm with speeds of 0.4-5 µm/s and 2.5-20 repetitions. The results are shown in Figure 5, where b) shows the detachment forces determined from three cells measured with 10 nm distance, 0.4 µm/s and 20 repetitions, whereas c) shows single cell measurements of distances between 100-1000 nm. Since most of the mean detachment forces determined decrease during a stimulation, I conclude that z-stimulation experiments had no or an adverse impact on cell detachment. Hence, at first glance, the z-stimulation method seems to be an alternative to unpredictable modulation measurements, however, I do not recommend to follow this approach further.

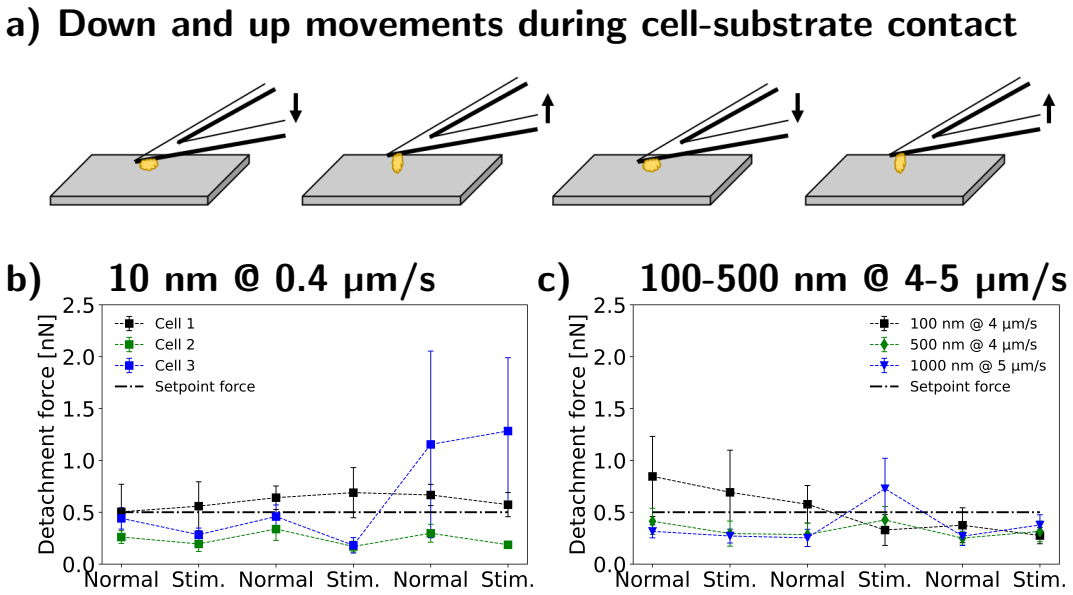

Figure 5: Preliminary results of z-stimulation experiments. a) The cantilever was consecutively moved down and up during cell-substrate contact. b) Mean detachment forces determined during preliminary z-stimulation measurements with 10 nm, 0.4 µm/s, 20 repetitions show no or adverse effects of the stimulation (except cell 3 during the last cycle). c) Mean detachment forces determined during single cell measurements with distances of 100-1000 nm, 4-5 µm/s speeds and up to 20 repetitions show that the z-stimulation seems to be rather harmful to the cells.

F Supporting Information for Manipulations of Fibroblast Cells with Oscillatory Forces

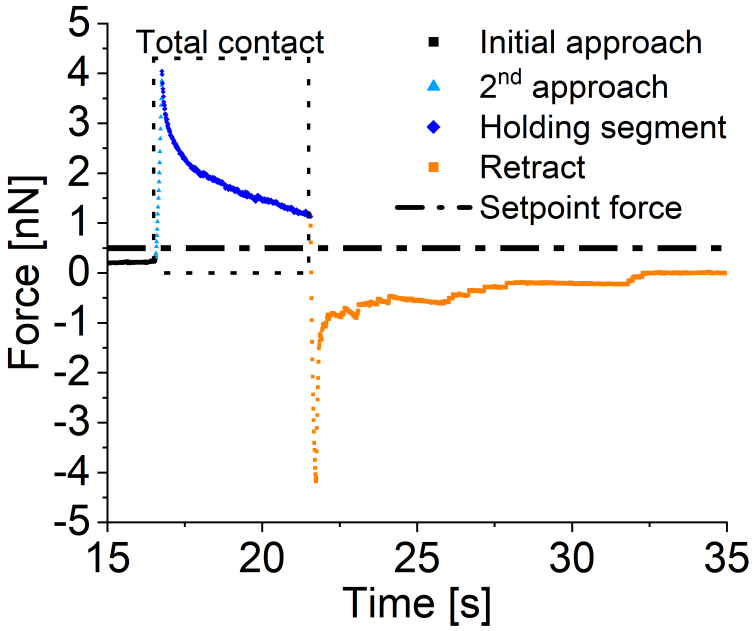

Figure 6: Force-time curve of a reference measurement for modulations with 1000 nm amplitudes. After the initial approach to 0.5 nN, a second approach accounted for the 1000 nm additional distance during modulation measurements. This resulted in a pronounced force increase, which was partially expected. However, that the maximum applied force was larger than the applied forces during modulations was unexpected.

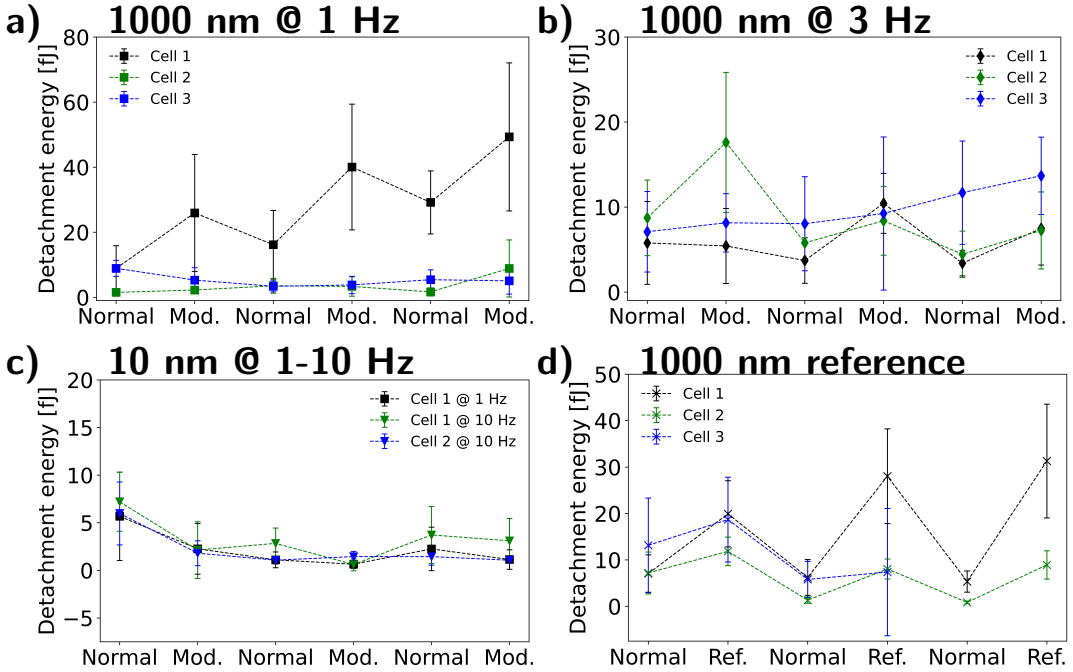

Figure 7: Mean detachment energies as a function of the applied modes. Each symbol shows the mean detachment energy of up to 20 force-distance curves and the error bars denote the standard deviations. The results of detachment energies showed a similar trend than the detachment forces presented in Section 3.4.4. Modulations with an amplitude of 1000 nm and frequencies of a) 1 Hz and b) 3 Hz mostly increased detachment energies for a modulation compared to the normal mode. An overall positive impact of the modulation with 1000 nm was indicated through the increased detachment energies after the third cycle compared to the values from the first normal mode. c) Modulations with 10 nm amplitude showed decreased detachment energies compared to detachment energies of normal modes. This indicates a negative impact. d) Reference measurements resulted in pronounced increases of detachment energies compared to detachment energies of normal measurements.

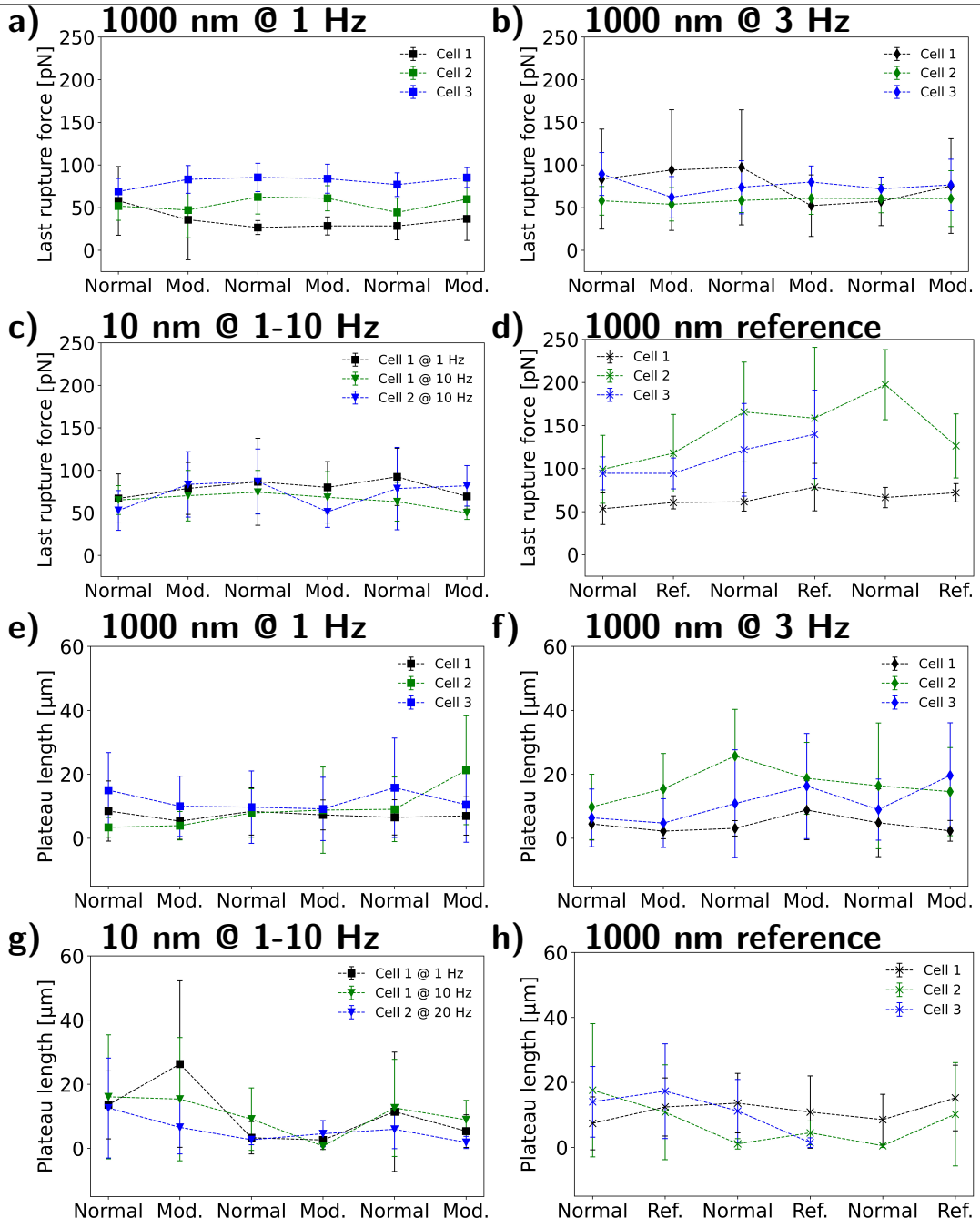

Figure 8: Mean last rupture forces (a)-d)) and mean plateau lengths (e)-h)) as a function of the modes applied. Each symbol shows the mean value of up to 20 force-distance curves and the error bars denote the standard deviations. The values of both the last rupture forces and the plateau lengths showed no distinctive differences and/or trends throughout the cycles of all modulation types and the reference measurement. This suggests that the last rupture force and plateau length are independent of the investigated modulation settings and additionally applied forces.

G Supporting Information for Manipulations of HEK293T Cells with Oscillatory Forces

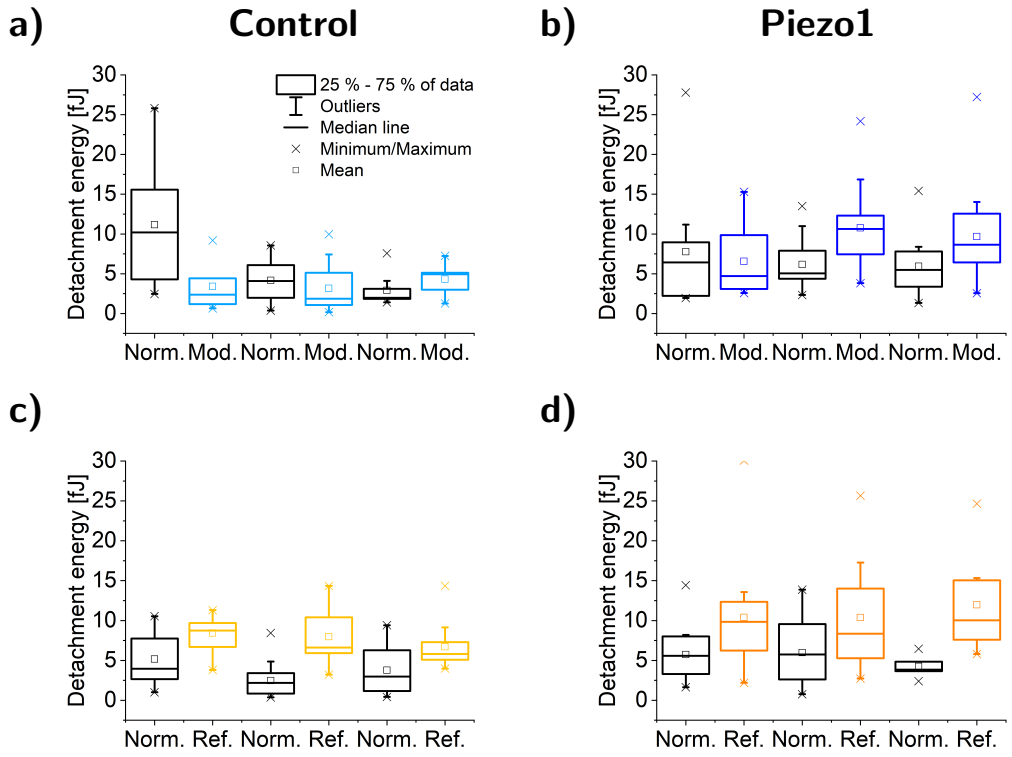

Figure 9: Distributions of detachment energies as a function of the applied modes. Each graph shows the results of a single cell measurement. Normal measurements are labeled with black, modulation measurements are labeled in blue colors (light blue: Control cell, dark blue: Piezo1 cell) and reference measurements are labeled in orange (light orange: Control cell, orange: Piezo1 cell). The results of detachment energies fit well with the observations of detachment forces presented in Section 3.4.6. a) Modulations of a control cell showed no distinctive difference or trend throughout the cycles. b) Modulations of a Piezo1 cell showed an increase of mean values of detachment energies compared to detachment energies of normal measurements for the second and third cycle. Additionally, a slight overall increase of detachment energy during modulations can be suggested. c) Reference measurements of a control cell showed a reversible prominent increase of mean detachment energies. d) Reference measurements of a Piezo1 cell showed an increase of mean detachment energies compared to detachment energies of normal measurements. In addition, an overall increase of the distributions during references was detected.

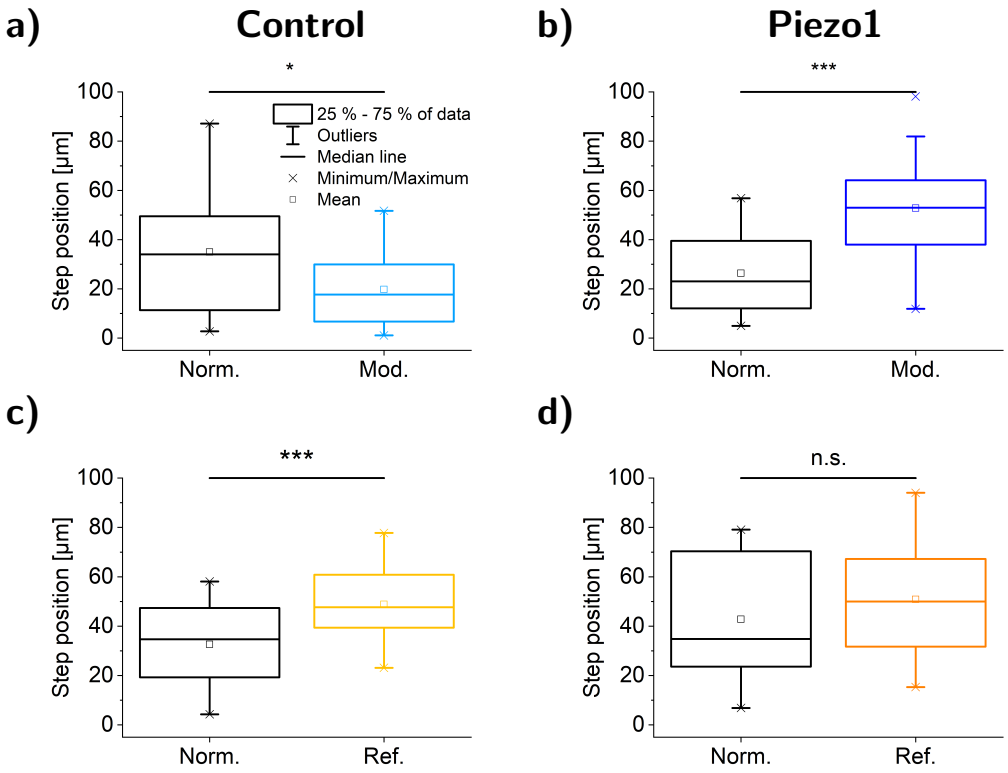

Figure 10: Distributions of step positions for the different cell types. Each box combines all step positions of the corresponding mode determined (e.g., for all normal measurements). The significance level determined with a student's t-test is * $p < 0.05$, *** $p < 0.001$ or not significant (n.s.) at $p < 0.05$. a) A modulation of the control cell resulted in a slight decrease of the step position. b) A modulation of the Piezo1 cell showed a significant increase of the step position. c) A similar significant increase of the determined step positions was observed for a reference measurement of a control cell. d) A reference measurement of a Piezo1 cell showed no significant impact on the step position.

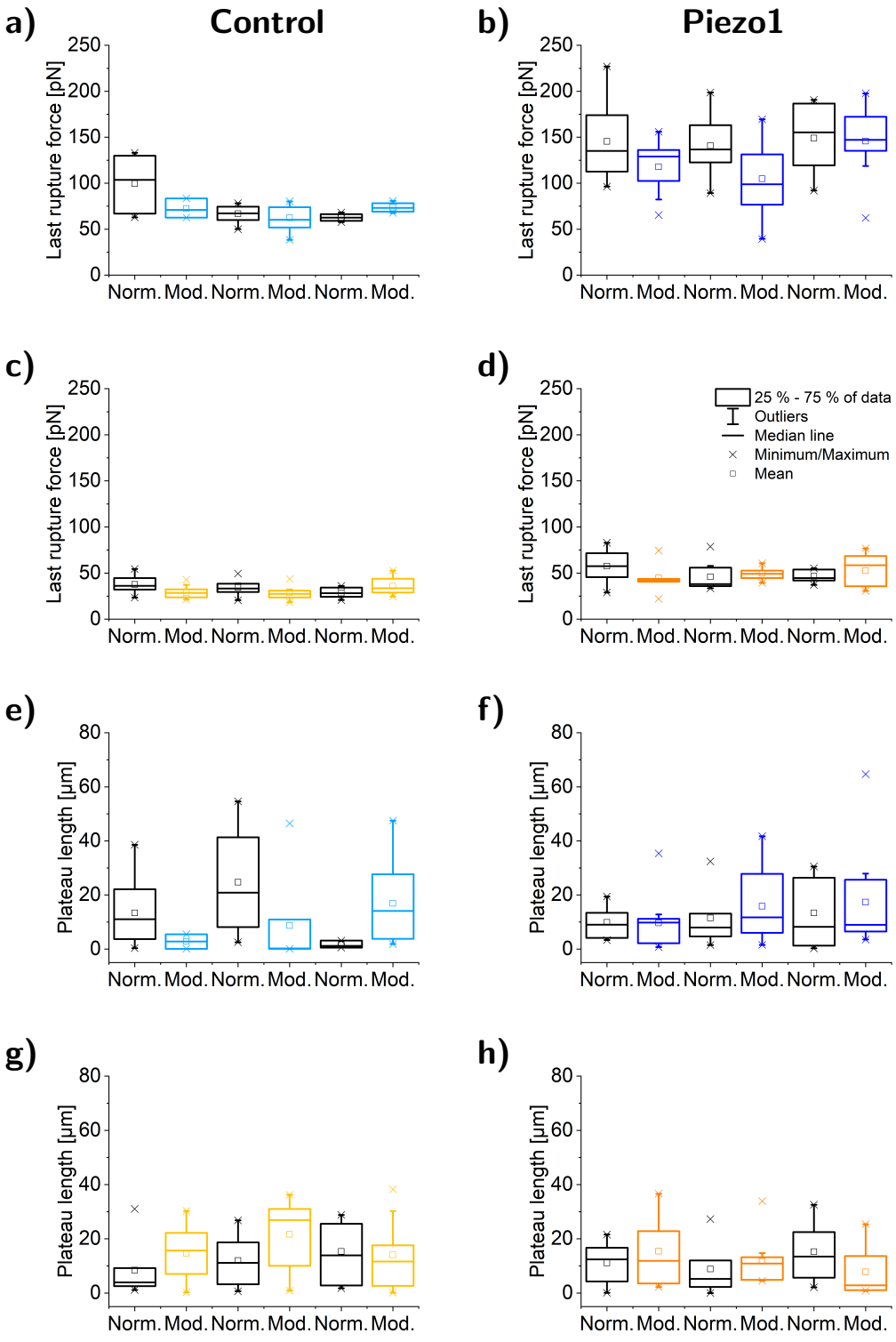

Figure 11: Distribution of last rupture forces (a)-d)) and plateau lengths (e)-h)) as a function of the modes applied. The last rupture forces showed no clear variations, except for the modulated Piezo1 cell. I suggest a slight decrease of the last rupture forces due to modulations. The mean plateau lengths showed slight variations between cell type and/or throughout the measurement cycles but it was not possible to suggest a clear trend of the parameter.